MINIMUM ENTROPY TECHNIQUES FOR DETERMINING THE PERIODS OF W UMA STARS

by

IAN ALBERT McARTHUR

submitted in accordance with the requirements

for the degree of

MASTER OF SCIENCE

in the subject of

ASTRONOMY

at the

UNIVERSITY OF SOUTH AFRICA

SUPERVISOR: PROF D P SMITS

AUGUST 2014

Student Number: 3304-799-5

I declare that

MINIMUM ENTROPY TECHNIQUES FOR DETERMINING THE PERIODS OF W UMA STARS

is my own work and that all the sources that I have used or quoted have been indicated and acknowledged by means of complete references.

I further declare that I have not previously submitted this work, or part of it, for examination at UNISA for another qualification or at any other higher education institution

.....

Ian Albert McArthur

.....

Date

Acknowledgements

Thankyou to my supervisor Prof. D. P. Smits for his guidance and support throughout the course of this study.

Thank you to Ms P. Skelton for the amazing assistance which she was always so willing to provide.

Thank you also to Ms A. Prozesky for so kindly sourcing administrative documentation.

This research has made use of the following data bases:

- The SIMBAD database, operated at CDS, Strasbourg, France and the SAO/NASA Astrophysics Data Stream.
- The ASAS-3 Catalogue of Variable Stars.
- The SuperWASP database, operated by the Universities of Warwick and Keele.

Summary

This MSc report discusses the attributes of W Ursae Majoris (W UMa) stars and an investigation into the Minimum Entropy (ME) method, a digital technique applied to the determination of their periods of variability. A Python code programme was written to apply the ME method to photometric data collected on W UMa stars by the All Sky Automated Survey (ASAS). Starting with the orbital period of the binaries estimated by ASAS, this programme systematically searches around this period for the period which corresponds to the lowest value of entropy. Low entropy here means low scatter (or spread) of data across the phase-magnitude plane. The ME method divides the light curve plot area into a number of elements of the investigators choosing. When a particular orbital period is applied to this photometric data, the resulting distribution of this data in the light curve plane corresponds to a specific number of data points in each element into which this plane has been divided. This data spread is measured and calculated in terms of entropy and the lowest value of entropy corresponds to the lowest spread of data across the light curve plane. This should correspond to the best light curve shape available from the data and therefore the most accurate orbital period available. Subsequent to the testing of this Python code on perfect sine waves, it was applied, and its results compared, to the 62 ASAS eclipsing binary stars which were investigated by Deb and Singh (2011). The method was then applied to selected stars from the ASAS data base.

KEYWORDS: stars – All Sky Automated Survey: binaries – eclipsing – stars – Roche: variables – W UMa – A-type – W-type: information theory – minimum entropy – period-change – light curve: magnetic field – starspots

Contents

Chapter 1

Classification of Binary Stars

1.1 Introduction

A variable star is any star whose brightness in any wavelength range of the electromagnetic spectrum changes with time. The brightness variations could be a single event such as occurs when a star goes supernova, the irregular eruptions seen on flare stars, or a regular repeating pattern such as seen in pulsating stars and eclipsing binary systems.

A binary star is a stellar system consisting of two stars orbiting around their common centre of mass. From Newton's Law of Universal Gravitation it is straightforward to show that for two stars of masses M_1 and M_2 orbiting each other with a semi-major axis of length a, the orbital period P is given by

$$4\pi^2 a^3 = G(M_1 + M_2)P^2$$

where G is the gravitational constant. Clearly, the period of a binary system depends on the mass of the component stars and their separation. Therefore, by measuring the period accurately, the geometry of the system can be constrained. If the period is known and radial velocities of the components can be measured using spectroscopy, then it is possible to calculate directly the masses of the two component stars. This in turn allows other properties such as radius and density to be determined. Because the parameters of

binary stars, the period in particular, can be measured more accurately than for single stars, they provide a powerful means of testing theories of stellar structure and evolution.

A commonly held opinion is that most stars in the Galaxy are in binary or multiple star systems. This is certainly true for bright massive stars, but it is not true for red dwarf or M stars which are considerably more abundant than high-mass stars. Combining all the star counts, Lada (2006) suggests that two-thirds of all main-sequence stellar systems in the Galactic disc are composed of single stars. However, even if they are no longer as abundant as previously believed, binary stars provide an important diagnostic test of stellar physics and are therefore very important in astrophysics.

The variation of stellar brightness with time is called a light curve. The classification of certain types of variable stars is based entirely on the shape of their light curves. Historically, variable stars were identified by eye which relies essentially on white light, but modern optical studies often use observations in a particular photometric band (such as the Johnson U, B, V, R filters) to determine a light curve.

The main thrust of this dissertation is the investigation of the application of the Minimum Entropy (ME) method to increasing the accuracy of the periods determined for W UMa stars in the All Sky Automated Survey (ASAS) data base. The ME method applies the concept of entropy to the location of ASAS photometric data, associated with a particular orbital period, on a light curve or phase-magnitude plane. The sense of the word "entropy" here is the order or disorder of the data distribution in the plane of the light curve on the application of a particular value for the orbital period of the binary. The greater the order of the data distribution, the lower the entropy should be. This means that the greatest order should produce a light curve closest to the true light curve of the binary and therefore the lowest value of entropy. The lowest entropy then should correspond to the most accurate light curve period possible with the available data.

In order to carry out this investigation a program was written in Python code which varied the period applied to the data of a given star and determined which period produced the lowest entropy. The Python code was tested on the data from two perfect sine waves and produced accurate results. It was then applied to the photometric data of the 62 ASAS eclipsing binary stars which were investigated by Deb and Singh (2011) and the results compared. Next, it was applied to the photometric data from a number of W UMa

stars selected from the ASAS data base. When the ASAS variable star catalogue was downloaded from the ASAS website it was found to contain 50124 stars. The 50124 stars were searched for stars which appeared to have the photometric characteristics of W UMa stars. The stars were also required to be sufficiently bright that the effect of noise would be minimal, but not so bright that the camera CCD would suffer saturation affects. The result was still a huge number of stars and so from the list of stars satisfying the above criteria a small number were selected at random for studying.

One of the desired outcomes of the investigation was to determine the minimum number of elements into which it is necessary to divide the phase–magnitude plane in order to achieve accurate results. Although this can depend on the number of photometric data points in the ASAS file, a 50 x 50 phase–plane division matrix appears to be optimum.

This chapter introduces the concepts of variable stars and light curves and gives a description of the scope of this dissertation. The classification of binary stars is described along with the Roche model of binary stars and its application to their classification.

Chapter 2 - W UMa Stars. This chapter gives some of the history of W UMa stars and their classification as distinct entities. The introduction of subclasses of W UMa stars is described. The characteristics and evolution of W UMa stars is discussed as well as the various models introduced to try and explain these characteristics.

Chapter 3 - Entropy Theory. This chapter introduces the concepts of entropy and information theory and some of the equations leading up to equation 4.1 and equation 4.2, the equations on which the ME Python programme is based.

Chapter 4 - Application of Minimum Entropy. This chapter describes the method of minimum entropy and its application to ASAS data. A Python code programme was written to apply the ME method to photometric data collected on W UMa stars by the ASAS. Starting with the orbital period of the binaries estimated by ASAS, this programme systematically searches around this period for the period which corresponds to the lowest value of entropy. Low entropy here means low scatter (or spread) of data across the phase–magnitude plane. The Python ME programme divides the light curve plot area into a number of elements of the investigators choosing. When a particular orbital period

is applied to this photometric data the resulting distribution of this data in the light-curve plane corresponds to a specific number of data points in each element into which this plane has been divided. This data spread is measured and calculated in terms of entropy and the lowest value of entropy corresponds to the lowest spread of data across the light curve plane which should correspond to the best light curve shape available from the data and therefore the most accurate orbital period available from the data.

Chapter 5 - Testing and Applying the Python Code. This chapter includes the description of the application of the Python programme to perfect sine waves in order to measure the correctness of the code and the accuracy of the ME method. Tests carried out to assess the fact that 50 x 50 is the optimum number of elements into which the programme should divide the phase–magnitude plane are described. The investigation into impact of the number of available photometric data points in an ASAS file is described. Finally the code is applied to both bright and dim stars and the quality of the light curves compared.

Chapter 6 - Conclusion. This chapter discusses the findings of the investigations and summarises the results of the various chapters.

Appendix - Additional Material. Phase–magnitude diagrams folded using the ASAS period and the ME period are presented for a number of stars, illustrating differences between the values determined.

1.2 Eclipsing Binaries and Light Curve Classification

A very important class of binary stars are those systems whose orbital planes lie such that the components periodically pass in front of each other with respect to an observer's line of sight. When this happens, the combined light of the system decreases, causing changes in the brightness of the system. The light curve of eclipsing binaries show periodic variations related to the orbital phase of the two components. In addition to their Roche model classifications, eclipsing binaries can also be classified in terms of the shapes of their light curves. The General Catalogue of Variable Stars (GCVS) uses the following light curve-based classifications (Samus and Durlevich, 2009):

EA The prototype light curve for this classification is that of the star Algol, also known as Beta Persei. The moment of the beginning and end of eclipses are clearly defined, while between eclipses the light curve is nearly constant. Secondary minima may be absent. The depths of eclipses vary widely and can reach several magnitudes in certain cases. Observed periods have been found to vary from 0.2 days to more than 10 000 days. An example of an EA light curve is shown in Fig. 1.1[1].

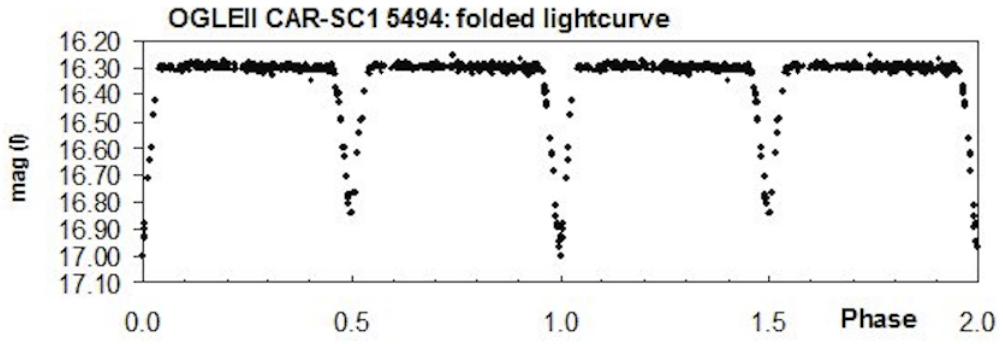

Figure 1.1: An example of an EA light curve.

EB or Beta Lyrae-type light curves typically have visual magnitudes less than 2 and periods longer than one day. The brightness changes continuously with phase so that it is impossible to specify the exact time of onset or end of the eclipses; there are no phase ranges of constant brightness. A secondary minimum is always observed but its depth is usually much shallower than that of the primary minimum. A typical example of an EB light curve is shown in Fig. 1.2.

EW or W UMa-type light curves are eclipsing systems with periods shorter than one day. The light curve varies continuously so that it is not possible to specify the start and end times of eclipses. The depths of the primary and secondary minima are almost equal, differing by less than 0.2 mag in the V-band. The light curve changes by about 0.8 mag in V-band, and the components of these systems generally have

[1]Figures 1.1, 1.2 and 1.3 are taken from the Peremennye Zvezdy Variable Stars website: "New Eclipsing Binaries in the OGLE-II Database (Part 1). The Carina Galactic Disk Fields"; http://www.astronet.ru/db/varstars/msg/eid/PZP-12-0011

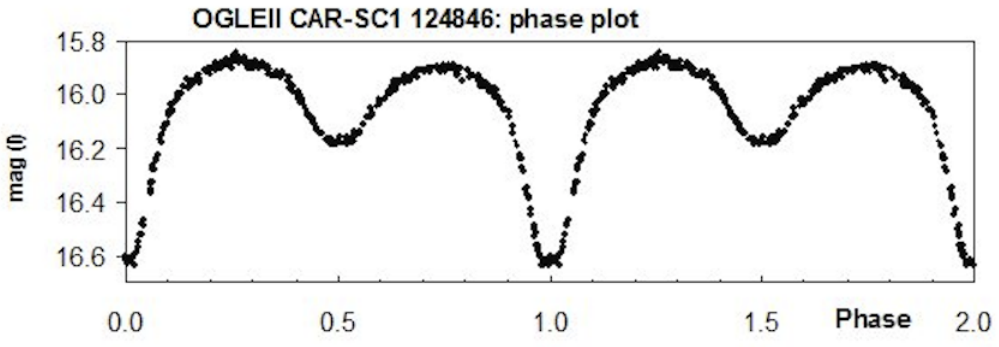

Figure 1.2: An example of an EB light curve.

spectral types between F and K. These features can all be seen in the example shown in Fig. 1.3.

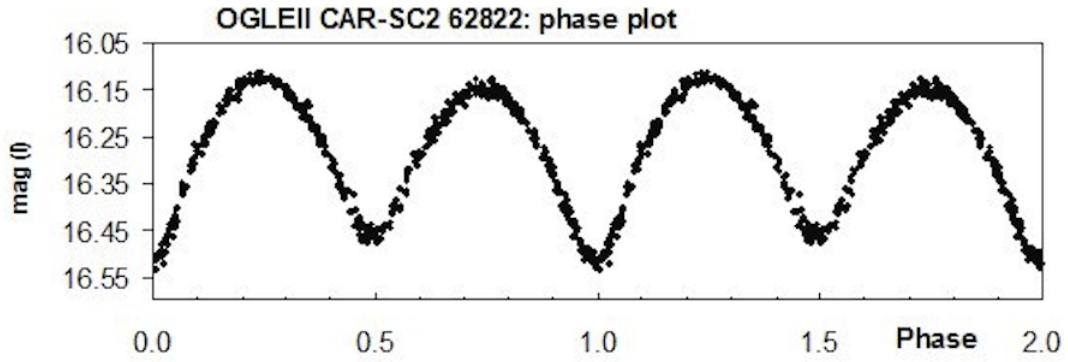

Figure 1.3: An example of an EW light curve

1.3 The Roche Model

Consider a particle held at rest relative to two large bodies of mass M1 and M2 rotating about their centre of mass (Shu, 1982). The particle will experience a force of gravitational attraction towards both bodies. In addition, because it is rotating, the particle will experience a centrifugal force relative to the centre of mass. The combined effect of these

two forces is a potential energy possessed by the particle. As the body is moved relative to M1 and M2 the potential energy changes. This potential energy is a function of position. Clearly when this particle is moved to a position near the centre of either M1 or M2, the dominant force will be the gravitational attraction of that large body. If the particle is located anywhere on the surface of a hypothetical sphere centred on M1 and passing through its original position, then it will experience the same potential energy manifested as a force directed towards the centre of M1.

Very far from both bodies, and in the plane of their rotation, where their gravitational force is low, the overriding force experienced by the particle will be an outwardly directed centrifugal force due to its rotation relative to the centre of mass. A hypothetical circle in the plane of rotation, centred on the centre of mass of the system and passing through the particle location and enclosing both bodies, will again be a locus of equal potential energy which the particle will experience as an outward force directed away from the mass centre. Effectively then, where these bodies are stars in a binary system, around and between M1 and M2 there exist surfaces of constant potential, or equipotential surfaces as they are called in the Roche model. The Shu (1982) diagram shown in Fig. 1.4, illustrates how the potential energy sphere around each body mutates into a circle around both bodies M1 and M2 in the plane of rotation. These equipotential surfaces are the basis of the Roche model (Kopal, 1959). The equipotential surfaces represent surfaces of uniform gas pressure and consequently, in a static environment, surfaces of uniform gas temperature.

The point between the binary components, where the potential disappears because the gravitational force due to M1 and M2 is equal and opposite, is called the inner Lagrange point and is usually designated as L1. The surfaces around each mass which intersect at L1 are called inner critical surfaces or Roche lobes Fig. 1.5. It is possible for three binary system conditions to exist in the Roche model of equipotential surfaces; the photospheres of both stars overfill their Roche lobes, the photosphere of one star overfills its Roche lobe or the photosphere of neither star overfills its Roche lobe. Binary systems are classified as contact, semi-detached or detached respectively for these situations (Kopal, 1955). A binary system may pass through any or all of these stages during its evolution. Because they are so far apart, astrometric and visual binaries are detached systems. Spectroscopic and eclipsing binaries could belong to any of the three classes.

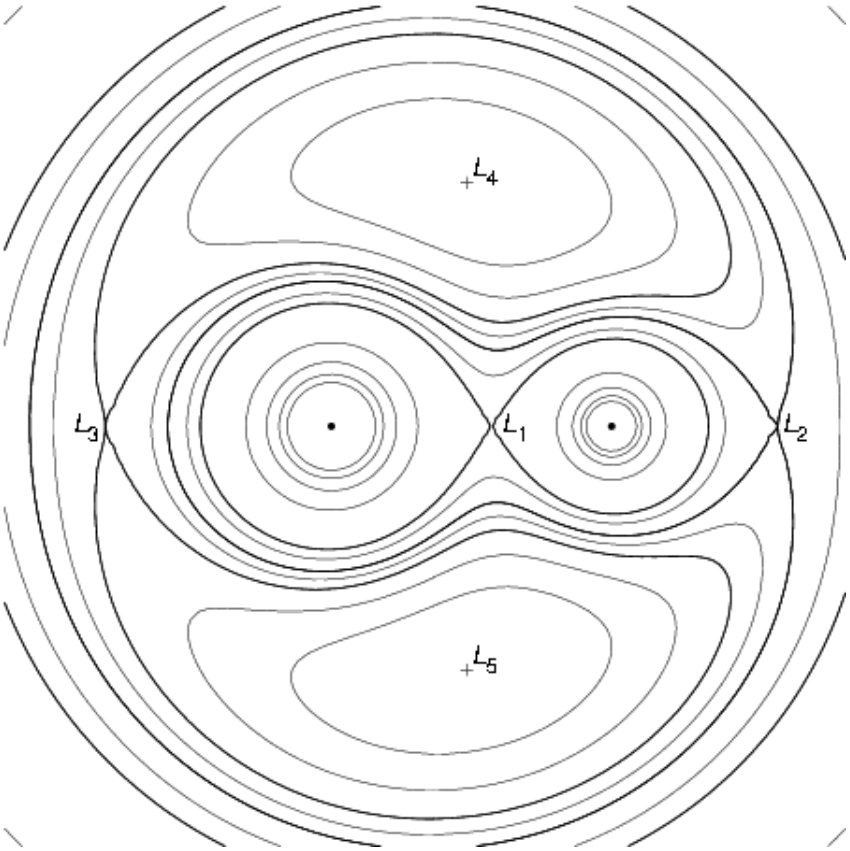

Figure 1.4: Diagram copied from Shu (1982) illustrating the equipotentials in the Roche model and the location of the five Lagrangian points.

Based on the degree to which the inner Roche lobes are filled, the GCVS uses the following categories to classify stars:

Detached binaries: The photospheres of these stars lie well inside their Roche lobes and they exert only gravitational force on one another. The GCVS definitions are:

- AR – Named after their prototype, AR Lacertae, both components are subgiants.
- D – Detached systems.
- DM – Detached systems in which both components are main-sequence stars.
- DS – Detached systems with a subgiant.

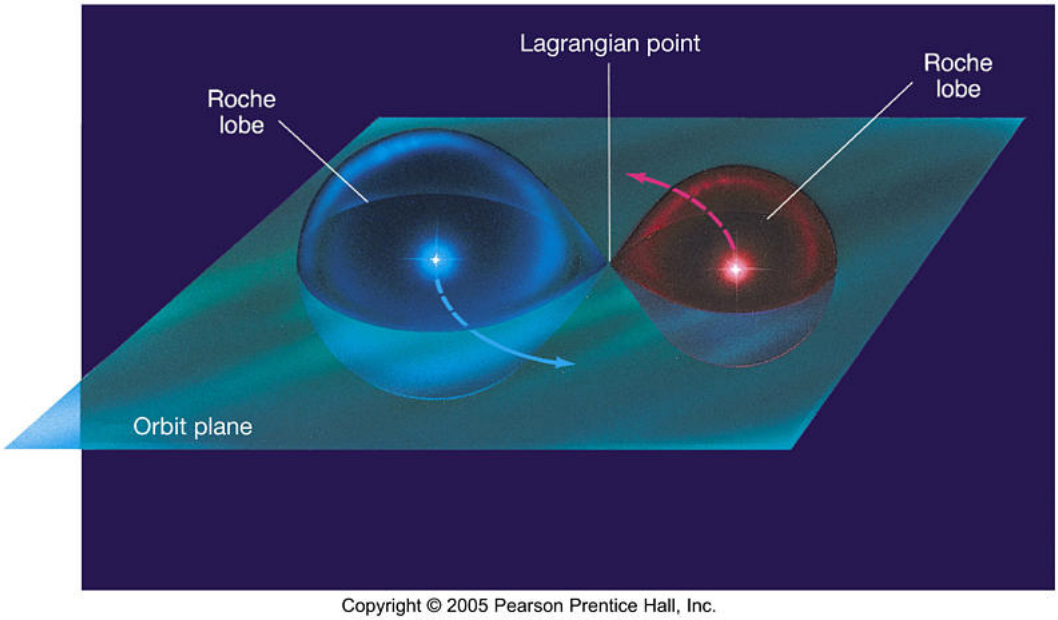

Figure 1.5: An illustration of Roche lobes meeting at the Lagrangian point L1, taken from Chaisson and McMillan (2005)

- DW – Systems similar to W UMa-type (see KW classification below) in physical properties, but not in contact.

Semi-detached binaries: The photosphere of one star completely fills its Roche lobe and it is called the contact component of the binary while the second star of which the photosphere does not fill its Roche lobe is called the detached component. In these stars material is transferred from the contact component to the detached component through the L1 point. If the detached component lies well inside its Roche lobe, it will have a surface closely approximating a spherical shape. The lobe-filling component has a distorted shape defined by the Roche lobe potential. The GCVS labels these systems as SD.

Contact binaries: The photospheres of both stars fill or overfill their Roche lobes. It is believed that such systems where the Roche lobes are overfilled are the rule and in such instances the two Roche lobes are enclosed by a single envelope of material hiding the stars from view. The GCVS classifies these systems into:

- K – contact systems, all of which have components with ellipsoidal surfaces.
- KE – Contact systems with spectral type in the range from O to A, i.e. early type stars.
- KW – Contact systems of the W UMa-type, having spectral types in the range from F to K. Primary components are main-sequence stars and secondaries lie below and to the left of the main sequence in the $(M_V,\ B-V)$ diagram.

1.4 Eclipsing Binaries and the Roche Model

Broadly speaking, eclipsing binaries classified by their light curves as EA, EB and EW, can be associated with detached, semi-detached and contact systems, respectively, in the Roche model.

Detached systems have both stellar components lying below their Roche lobes. The stars will have spherical or slightly ellipsoidal components. The area presented by both stars is constant until the eclipse begins and once the eclipse is over. The start and end times of eclipses can be clearly distinguished, and between eclipses the light curve remains almost constant or varies insignificantly because of reflection effects or slight ellipsoidality of the components. This would be particularly true of long period systems in which the stars are separated by large distances. The two stars evolve separately, i.e. there is only a gravitational interaction between them with no exchange of material, and can be of totally different masses and, therefore, spectral type. A bright star being eclipsed by a faint star would create a significant dip in the light curve, while a faint star being eclipsed will not affect the total brightness of the system. Therefore, this model can account for the large amplitude of the primary eclipse seen in some EA light curves, and the apparent lack of a secondary eclipse.

In semi-detached systems one of the stars fills its Roche lobe and very often transfers material to the other star via the L1 point. The Roche lobe-filling star has a marked non-spherical shape, while the other star could have a shape from spherical (if it is small compared to the lobe-filling star) to non-spherical (if it is also close to filling its Roche lobe). As seen by an observer, the area of the distorted star changes continuously as the

stars orbit each other, so the brightness of the system varies throughout the cycle. This makes it difficult to define the start and end of eclipses. Because the stars often have very different masses (and therefore temperatures), the primary and secondary eclipses can have noticeably different amplitudes.

The two stars in contact systems are both highly distorted and are surrounded by a common envelope. The projected area seen by an observer changes throughout the orbital cycle so the start and end of eclipses cannot be distinguished. Because the stars must be close to form a contact system, their orbital periods are short. The similarity in the depth of the light curves during primary and secondary eclipses is a result of the common envelope distributing heat so that both components have similar temperatures.

Because of the strong tidal forces acting on the components of EW systems, the Roche model is particularly relevant to them. Dynamical models of close binary systems indicate that the components rapidly develop circular orbits, and synchronous rotation, i.e. the orbital and spin periods of the components become phase locked. Observationally, the eclipses of EW systems occur at phases separated by exactly 0.5 of an orbital phase, which is proof that the orbits are circularised.

If an observer's line of sight is close to the orbital plane of a binary system, under suitable conditions, it is possible for a total eclipse to occur. An example of this can be seen in the light curve of MW Pav shown in Fig. 1.6. This occurs when one star completely disappears behind its companion, or moves across the face of its companion obscuring a constant amount of surface area. In these cases, the light curve will display a flat profile during mid-eclipse, rather than the continuously varying profile shown in Figs. 1.1, 1.2 and 1.3. Total eclipses can occur in EA, EB and EW systems but are rare; even rarer are total eclipses of both minima. Flat-bottomed eclipses are particularly useful because, by solving for the orbital parameters of the system, it is possible to determine the radius of the eclipsed star, which is an important parameter to know when modelling the structure of stars.

It is not always easy to distinguish between EB and EW eclipsing binaries. As already discussed the EW phenomenon is best explained by assuming that both stars are in contact and the more massive component is transferring luminosity to the less massive component via a common envelope, equalising the surface temperatures.

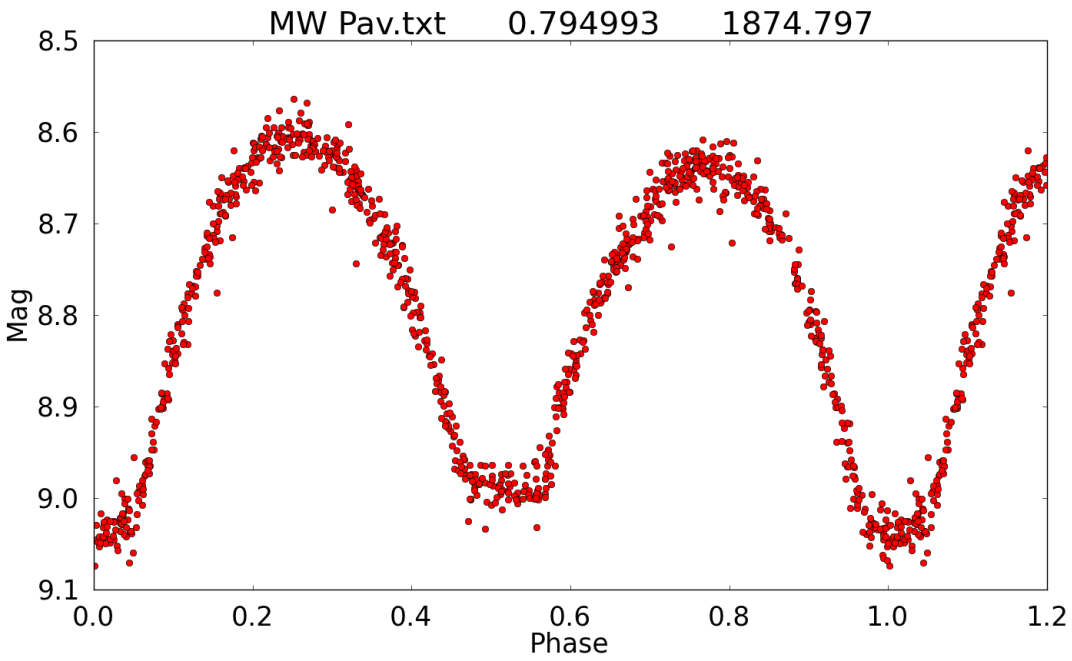

Figure 1.6: Light curve of MW Pav. The flat bottom of this total eclipsing system is apparent at phase 0.5.

The process is difficult to model but theoretical investigations indicate that thermal contact is broken from time to time, so that the system cycles between a contact system and a semi-detached system. Evidence for this scenario comes from some EB systems with masses and periods similar to those found in EW systems.

Chapter 2

W UMa Stars

2.1 Introduction

W UMa stars are rare, with a local space density of about 0.2% of main-sequence stars (Paczyński *et al.*, 2006). Howevere, W UMa stars far outnumber all the other eclipsing variable stars (Lucy, 1968a; Shapley, 1948). Therefore, contact systems are the most common eclipsing binaries. Because the relative number of W UMa stars is high, these systems must be young and still on or near the main sequence, evolving on nuclear time scales. Haffner (1937) reported that there is a W UMa star in the young cluster Praesepe, which is less than 10^9 yrs old, and hence provides evidence of these systems being unevolved. Each of the two stars comprising these binary systems has, in general, a mass of the order of a 1 $M_\odot$ or less (the reason for their long lives), making them useful objects on which to test theories of low mass stars (Mauder, 1972).

In this chapter the properties of W UMa stars and the characterization of the class of W UMa-type stars are discussed. After more than a century of observation and nearly five decades of having viable models, the origin and evolution of these contact binaries is still not resolved. A number of different models have been proposed to account for how they formed and where they will end up which are explained here.

2.2 W UMa: The Prototype

Muller and Kempf (1903) noticed W UMa's variable brightness while they were doing observations for the Potsdam Photometric Durchmustering. They reported that the light output of the star varied with a period of 4^{hrs}, which was the shortest period known for a variable star at the time. Furthermore, the W UMa light curve did not fit any of the known variable classes. One suggestion put forward by Muller and Kempf (1903) was that the variability might be explained by a rotating body of advanced age, developing a surface of non-uniform brightness as it cooled. However, the argument was not convincing so they also suggested that it was more likely that their observations resulted from the mutual eclipsing of two bodies of nearly equal size and luminosity orbiting very close to each other. Following observations by Muller and Kempf (1903) which convinced them that the light curve of W UMa could only be explained by an almost central eclipse of two ellipsoids nearly in contact, an assessment confirmed by Baldwin (1908) five years later, calculations by Russell (1912) convinced him that the eclipse theory explained the observed variability of W UMa. However, until 1919 the W UMa classification was not that widely accepted, probably on account of the exceptionally short period and spectral type (Adams and Joy, 1919).

The period was adjusted to $\sim 8^{hrs}$ when it was recognised that W UMa has two minima of slightly different amplitudes (Huffer, 1934). It varies from 7.8 mag to 8.5 mag in the V-band at primary minimum, i.e. $\Delta V = 0.7$ mag. The secondary minimum is brighter in the V-band than the primary by ~ 0.1 mag.

Shapley and van der Bilt (1917) noted that the colour of W UMa did not change during its orbital cycle. The constant colour means that the temperature of the system does not change with phase, a result that was difficult to reconcile with models of binary stars at the time. The temperature difference between the two components is less than 1000 K, even though their mass ratio q, where $q = M_2/M_1$, could be < 0.3.

W UMa has become the prototype for the class of variable stars that vary continuously by about 0.8 mag in the V-band over their orbital period of less than 1 day. Their light curves are symmetrical with maxima and minima of nearly equal amplitude and two minima of nearly equal depth. They have spectral types between F and K, and have very

small colour variations over the orbital period. The orbital periods have a sharp lower period cut-off at 0.22 d (Lohr *et al.*, 2012; Mullan, 1975). Note that in the literature the definition of a W UMa-type star can vary. For example, the spectral type can include A stars and sometimes the upper limit for the period is a bit longer than one day, e.g. 1.2 d.

The primary components of W UMa systems are main-sequence stars so the lower limit for an orbital period of 0.22 d translates into a lower limit for the primary mass of about 0.6 $M_{\odot}$ and for a total binary mass of about 1.0 to 1.2 $M_{\odot}$ (Kroupa *et al.*, 1993; Stepien, 2006a,b). The lowest mass a star on the main sequence can have is about 0.1 $M_{\odot}$.

2.3 Common Envelope Model

In a brief note, Kuiper (1948) pointed out that various paradoxes associated with observations of W UMa-type stars as two independent stars could be resolved if the binary had a common envelope in which strong currents transported photospheric material from the primary to the secondary. Kopal (1955) applied the Roche model to various types of binaries and suggested that W UMa-type stars were contact binaries in which both components overflowed their Roche lobes to form a common envelope. Building on this suggestion, Lucy (1968a,b) developed a theoretical model of two zero-age main-sequence (ZAMS) stars with a common convective envelope which he solved numerically. The major observed properties of W UMa-type light curves could be reproduced by Lucy's model. It is now generally accepted that W UMa-type systems consist of two main-sequence stars in a binary contact configuration with a common envelope that is a single connected convection zone.

The model proposed by Lucy (1968c) requires that heat is transferred by the common envelope from the hotter component to the cooler one. This results in an almost constant effective temperature over the surface of the two stars, and explains why there is essentially no colour change with phase. As contact binaries have a mass ratio distinctly different from unity, most nuclear energy is generated in the more massive component and redistributed around the whole surface via the convective envelope. The model has been

universally accepted and also supports Eggen (1967) assertion that contact systems have a total luminosity and mass that is equivalent to two equal stars of the observed colour.

The light curve of FO Hya is found to be asymmetric around the primary and secondary maxima with the secondary maximum brighter than the primary maximum. Because of large tidal distortions exerted by each star on its companion, the components have highly distorted ellipsoidal shapes joined by a neck of material. The different masses of the individual stars results in the components having different sizes. The brightness changes observed in EW light curves reflect the combined effect of the eclipse blocking light from one component, and changes in the observed surface area of the ellipsoidal component stars as the orientation of the system varies relative to the line of sight. In systems with low mass ratios the amplitude of the variation due to the orientation may be larger than the amplitude due to the eclipse (Prasad *et al.*, 2013; Rucinski, 1993a). FO Hya, see Fig. 2.1, AW UMa and Epsilon CrA display examples of this effect.

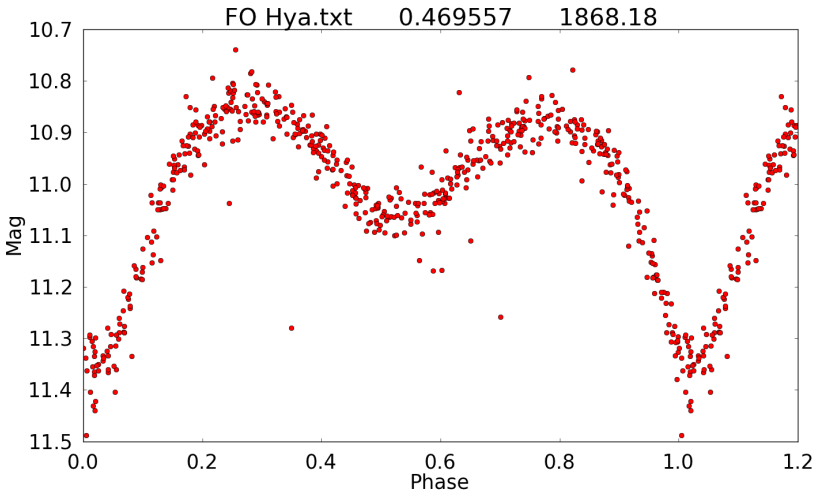

Figure 2.1: Light curve of FO Hya showing the asymmetry of the primary and secondary maxima.

The model correctly predicts the observed major characteristics of the light curves, but does not explain the asymmetries in the light curves of many systems. The light curves of many contact binaries are distorted, for example as shown in Fig. 2.2 for AK Her and in Fig. 2.3 for W Crv (Binnendijk, 1961; Lucy and Wilson, 1979; Niarchos, 1977;

Rucinski and Lu, 2000; Woodward and Wilson, 1977). Lucy and Wilson (1979) believe that these distortions are strong evidence for the predicted existence of non-equilibrium semi-detached systems but they could be due to starspots.

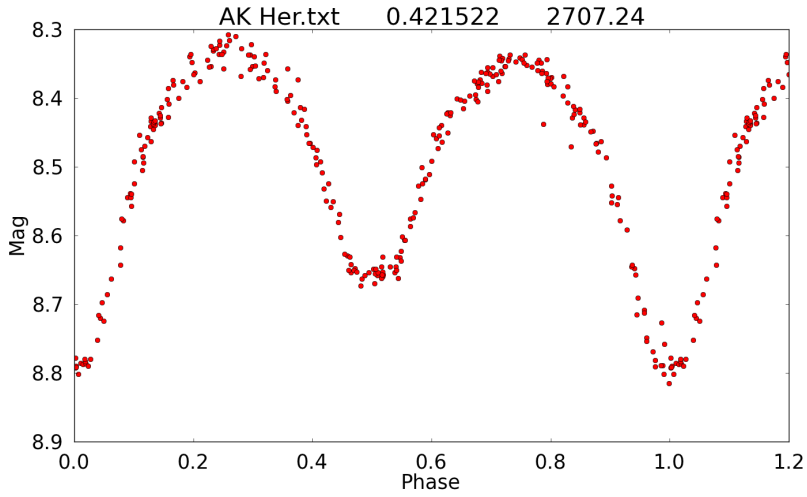

Figure 2.2: Asymmetric light curve of AK Her.

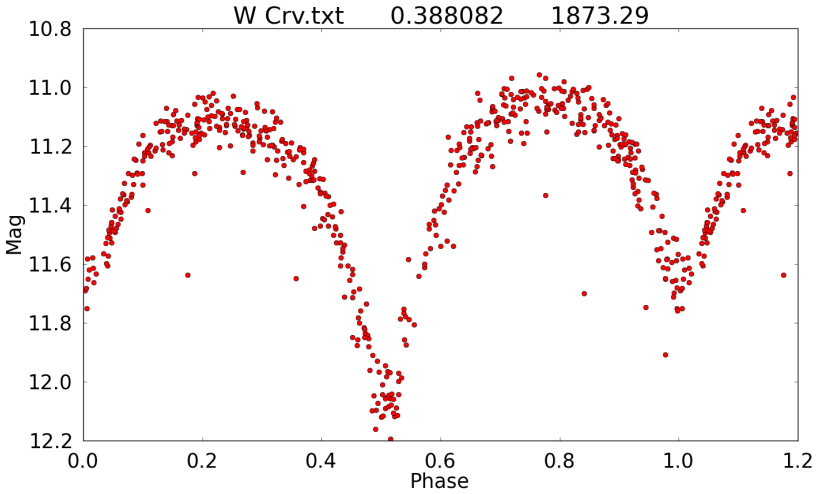

Figure 2.3: Asymmetric light curve of W Crv.

Yakut and Eggleton (2005) proposed that differential rotational shear is the mechanism

of heat transport in contact binaries. Helioseismology studies of the convective zone and photosphere of the Sun show the existence of a differential rotational shear layer in the solar convection zone. The Sun has a deep equatorial belt rotating about 10% faster than the mean rotation of the Sun. This means that it is carrying (advecting) an enormous heat flux sideways. The ratio of advection flux to convection flux is about 3000. If the Sun had a companion about half its size in contact with it, then the differential rotation driven by both the Sun and its companion would carry this heat from one body to the other and back, making the temperature of the joint surface much more nearly uniform than it would if the stars were not in contact. It is not clear how solar differential rotation is driven, but it is generally suspected to be the result of the combination of turbulent convection and Coriolis forces.

2.4 Subclasses of W UMa Systems

Two subclasses of W UMa-type systems were introduced by Binnendijk (1970), which he called A-type and W-type. In A-type systems the larger component of the binary is hotter than the smaller companion, a feature typical of main sequence stars. The primary minimum (the deeper of the two minima) of the light curve is caused by a transit eclipse. In W-type systems, the smaller component has a higher temperature than its companion, which means that the primary minimum is caused by an occultation eclipse. The radii of the secondary components of W-type systems are larger than the radii of normal ZAMS stars of the same mass (Binnendijk, 1957; Robertson and Eggleton, 1977; Yakut and Eggleton, 2005). The primary minimum of A-types is deeper than that of W-types. Mass ratios are generally greater than 0.3 for W-types, while for the A-types mass ratios appear to be less than 0.3. Binnendijk (1970) found A-types have earlier spectral types than the W-types. The spectral types of the A-type subclasses range from A to F. W-types tend to have later spectral types which range from G to K. The degree of contact is larger and the envelope thicker for A-type than W-type (van Hamme, 1982).

The two subclasses are usually assumed to be in slightly different states of evolution. Wilson (1978) reported that eight A-type systems with accurately determined parameters all had larger than ZAMS radii and were therefore evolved. Hilditch, King, and McFarlane

(1988) proposed that A-type systems evolve from W-type systems. These systems are binaries which are essentially in equilibrium, but have evolved off the ZAMS according to Woodward and Wilson (1977) and Lucy (1976). In contrast to Hilditch, King, and McFarlane (1988), Gazeas and Niarchos (2006) proposed that W-type systems evolve from A-type systems. The stars are closer to ZAMS than are A-type systems. Clearly, there is still a lot of uncertainty regarding the evolutionary status of A- and W-type systems.

2.5 Starspots and Magnetic Activity

Many contact binaries show a light curve asymmetry in which the two maxima have different heights. This is called the O'Connell effect. An example of the O'Connell effect in the W UMa-type system YY Eri is shown in Fig. 2.4.

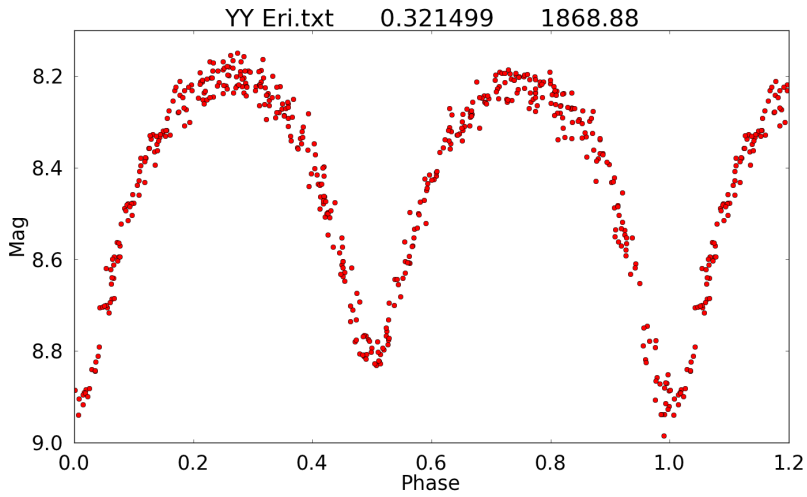

Figure 2.4: Light curve of YY Eri, a W UMa star displaying the asymmetric maxima of the O'Connell effect.

Binnendijk (1970) pointed out that the variations in the light curves of certain W UMa systems can be understood if a dark spot existed on the surface of one of the components. This asymmetry is usually attributed to the presence of starspots associated with strong

magnetic fields, The starspot hypothesis is supported mainly by computer modelling investigations because starspots are the simplest way to explain observed photometric light curves. However, the physical conditions required to produce the starspots often seem untenable; for example, in most cases starspots must be extremely large and fixed in time. Starspots, like sunspots, are usually taken to be cool regions relative to the rest of the stellar surface associated with strong local magnetic fields. In most cases it appears that starspots can be quite large (Bradstreet and Guinan, 1988).

Although spots have been invoked to interpret many light curves, modelling the spots is tricky and the parameters determined are seldom a unique solution to the problem. Many systems do not show asymmetries, but this does not necessarily indicate the absence of starspots.

Wilsey and Beaky (2009) are challenging the starspot hypothesis. They believe the information available in photometric data is far too limited to be a reliable source of confirmation of the starspot hypothesis for the O'Connell effect. They believe other supporting astronomy tools are required to determine the physical conditions which must exist in the binary system to produce the starspots; for example Doppler imagining, Zeeman splitting, polarization measurements, x-ray, ultraviolet and radio emission studies.

There are further indications of magnetic activity in contact binaries (Mullan, 1975). Coronal X-ray and chromospheric emissions have been observed from some W UMa-type stars. For single stars, chromospheric activity and rotation rate appear to be closely related and both decrease with age. A stellar dynamo producing a magnetic field in a single star is expected to work most efficiently in conditions of fast rotation and vigorous surface convection. However, convection is thought to lead to coronal activity, which undergoes hydrodynamic expansion producing a stellar wind. The charged particles in the wind are tied to the magnetic field lines, and as the wind expands away from the star, carries away angular momentum, thereby slowing down the star's rotation. This leads to a decrease in the spin period of a star and accounts for the low mean rotational speed of stars of spectral types F and G on the main sequence. Therefore, in single stars dynamo field strengths appear to be self-limiting.

Contact binaries, which have orbital and phase-locked spin periods of less than a day, rotate much faster than single stars. However, the observed magnetic fields are much

weaker than would be expected by extrapolating single star dynamo models. It appears that the convective envelope surrounding the stars suppresses the creation of magnetic fields in a way that is not well understood at this stage.

Solar measurements indicate that spots do not exist on the Sun unless the magnetic field strength exceeds 1.2 kG. The strongest fields ever observed associated with sunspots are about 5 kG. Crude estimates of toroidal field strength in rapidly rotating W UMa-type stars suggest that magnetic fields are strong enough (2 – 20 kG) to permit starspots to form. The probability of spot formation is larger on the primary component. Starspot flares may occur sufficiently often to explain short term variations from mean light curves.

2.6 Period–Colour Relationship

Eggen (1967) undertook observations of short-period contact binary systems using the Palomar and Mt Wilson telescopes, enabling him to study the location of these binaries in the period–colour diagram as a function of their ages. He followed up these observations with period–colour modelling of the binaries and concluded from his results and the fact that that these systems could only be found in specific areas of the period–colour diagram that they were not simply an evolutionary phase of a detached system, but were themselves a separate class of binary. By observing members of clusters and wide visual pairs, and using the spectroscopic data available to him at the time, he found that contact systems have a total luminosity and mass that is equivalent to two equal single stars of the observed colour.

The convective model developed by Lucy (1968c) does not give detailed agreement with the period–colour relation of Eggen (1967). However, Biermann and Thomas (1972) were able to produce W UMa models with period–colour relations matching observation when they allowed the convective envelopes around the primary and secondary stars in their model to have different adiabatic constants. Lucy (1973) was not able to produce models that fall into the period–colour diagram along the strip which observed systems are found to occupy. However, Lucy and Wilson (1979) found more than a hundred W UMa systems with periods less than approximately 0.4 d which lie well within the boundaries of the period–colour diagram of Eggen (1967).

2.7 Period Changes

Period changes are not unusual among W UMa-type stars. W UMa itself has experienced slight period changes since its discovery in 1903 (Muller and Kempf, 1903). Binnendijk (1957) studied 16 W UMa-type systems for which accurate long-term timing data were available and found that all but one of the systems (TX Cnc) had variable periods. TX Cnc had only been observed for 15 yrs at that stage. Dryomova and Svechnikov (2006) report equal rates of period increase and decrease in W UMa binaries that range from -1×10^{-6} to $+1 \times 10^{-6}$ d yr^{-1}. The distribution peaks about zero. Similarly, Kubiak, Udalski, and Szymanski (2006) looked at 569 contact binaries in the OGLE database and found 134 stars that had period variations. The period variations show period increases and decreases distributed with a half-width of 3.5×10^{-7} d yr^{-1} about zero and a maximum of 1×10^{-6} d yr^{-1}. From the data it was not possible to determine if there was a secular change over several years or periodic changes over short periods. They note that the shortest period systems seem to have the smallest period changes.

From the ASAS data Pilecki, Fabrycky, and Poleski (2007) identified 22 bright eclipsing binaries with high period-change rates. Of these contact binaries, five have increasing periods and the other 17 have decreasing periods. Using data from the Wide Angle Search for Planets (SuperWASP), Skelton (2009) showed that some of the period rates of change found by Pilecki, Fabrycky, and Poleski (2007) are incorrect.

Lohr *et al.* (2012) examined the SuperWASP data of 53 W UMa binaries and could find only three instances showing strong evidence for period change. Prša and Zwitter (2005) applied PHOEBE, eclipsing binary modelling software built on the Wilson and Devinney (1971) code, to two of these three binaries in order to determine the component masses, radii, orbital inclinations, surface potentials and other parameters.

Prasad *et al.* (2013) used the database of minima timings of Paschke and Brat (2006) together with some of their own observations to obtain a total of 67 minima timings for FO Hya over a span of 65 yrs. They found that the system had a long term period variation of 5.77×10^{-8} d yr^{-1} modulated by a sinusoid with a period of 42.30 yr.

The most likely explanation for cyclic variation appears to be the existence of a third body producing a light time-delay effect resulting from orbital motions impressed on the

system. Chandler (1892) interpreted periodic variations in the epoch of light minimum of Algol as a light time-delay effect resulting from the orbital motion of the eclipsing system with a third star. Woodward (1942a,b) noticed that the periods of several contact binaries varied, in particular that of the prototype W UMa, and suggested the possibility of a third body in each system to account for the changes. This idea was supported by Whelan, Mochnacki, and Worden (1974) who used the third body hypothesis to explain a mass ratio discrepancy in the W UMa system. Pribulla and Rucinski (2006) found that more than 50% of contact binaries have a third companion, and suggested that perhaps all W UMa-type systems have a third component which assists in forming the short period binaries. The existence of a third body in all W UMa-type systems is still an open question.

Period change will occur due to the transfer of mass between the components of the binary via the common envelope. The period decreases if the more massive component is losing mass to its companion, and no mass is lost from the system. Mass loss from the system via the L2 point and the concomitant redistribution of angular momentum (Rucinski, 1993b) should lead to a period increase. Pilecki, Fabrycky, and Poleski (2007) suggested that tidal dissipation resulting in orbital to spin angular momentum transfer could change the orbital period.

The presence of magnetic fields may affect the manner in which mass is transferred between components and may cause magnetic braking, which could account for at least some of the observed period change decreases of these systems. Magnetic activity could lead to changes in oblateness which would also result in period changes, Pilecki, Fabrycky, and Poleski (2007).

2.8 Evolution of W UMa Systems

Although observations of EW light curves have been made for more than a century, and successful models of contact binaries have been around for nearly 50 yrs, the origin and evolution of W UMa-type stars is far from clear. Because W UMa stars make up a large proportion of all eclipsing variable stars, it appears unlikely that they are a stage in the evolution of any other type of variable.

A possible birth scenario is fission at the end of the pre-main sequence contraction phase. This process should produce roughly the correct amount of angular momentum (Roxburgh, 1966) and mass ratio (Lucy, 1977). Binaries with a combined stellar mass of $M \leq 4M_{\odot}$ in the crude models of Roxburgh (1966) formed contact binaries, while more massive systems ended up as detached systems. Many astronomers were of the opinion that the fission theory was discredited, Boss (1988), Bodenheimer, Ruzmajkina, and Mathieu (1993) and Bonnell (2001), but Tohline (2002) was not convinced and recommended further modelling. An alternative model is that stars are born as detached binaries and evolve through a semi-detached phase before becoming contact binaries. To change from detached to contact systems, the component stars must gain mass or lose angular momentum. Examples of angular momentum loss mechanisms are magnetised stellar winds producing braking torque, or gravitational radiation.

2.8.1 Angular Momentum Loss

Angular momentum losses due to gravitational radiation do not appear to play a prominent role. Calculations by Robertson and Eggleton (1977) and Webbink (1975) suggest losses of about 10^{-11} to 10^{-10} d yr^{-1} for W UMa systems. Lohr *et al.* (2012) combined expressions from Kolb, Downing, and Clare (2010) and Hilditch (2001) to determine angular momentum loss, but obtained results six orders of magnitude too low. However, Vilhu and Rahunen (1980), Vilhu (1981) and Vilhu (1982) are of the opinion that it is plausible that contact binaries of W UMa-type evolve from detached binaries or semi-detached binaries by gradual angular momentum loss.

Hilditch, King, and McFarlane (1988) examined 31 F – K type binary systems which had been found to be in contact or near contact. They compared the masses, radii and luminosities of these systems with similar data of single stars. Based on these comparisons they concluded that:

- The primary components of shallow contact W-type systems are unevolved main sequence stars.
- The primary components of deeper contact A-type systems are near to terminal age main sequence stars.

- The secondary components of W-type classes have radii of the order of 1.5 times those of ZAMS stars with the same masses.
- The secondary components of A-type classes have radii of the order of 3 times those of ZAMS stars with the same masses.

Consideration of the above factors, together with the specific orbital angular momenta of these systems, led Hilditch, King, and McFarlane (1988) to suggest that there are two types of evolution into contact, as follows:

1. From detached systems, via marginal contact systems to the shallow contact W-type classes where the primary components are all main sequence stars displaying no particular concentration towards the ZAMS or terminal age main sequence.
2. From detached systems, via a mass transfer to semi-detached systems, to marginal contact systems to the deeper contact A-type classes where the primary components are predominantly more evolved than their W-type counterparts, with most of them lying near or beyond the ZAMS. This supports the findings of Lucy and Wilson (1979) that A-type systems are evolved objects.

2.8.2 Nuclear Evolution

It appears that nuclear evolution acts in a similar fashion to the reduction of angular momentum, apart from the fact that the orbital periods are longer for a given effective temperature, (Robertson and Eggleton, 1977; Stepien, 2006a,b; Yakut and Eggleton, 2005).

Long term evolution of a contact binary may be determined by nuclear evolution, particularly for systems with weak or no magnetic fields to provide angular momentum loss by magnetic braking. Yakut and Eggleton (2005) suggest that several near contact binaries do not evolve into contact binaries, but evolve, by nuclear evolution, like normal Algol systems except that they have unusually low mass and angular momentum.

If nuclear evolution is the path followed by W UMa systems, then in all probability they will end up as single stars. A small but significant population of rapidly rotating K sub-giants would be evidence of this route of evolution.

2.8.3 Thermal Relaxation Oscillation Model

Rahunen and Vilhu (1977), Robertson and Eggleton (1977) and Lucy (1976) dropped the assumption of thermal equilibrium and were able to construct ZAMS contact models with equal entropies. These models were in thermal non-equilibrium, caused by net mass transfer from the secondary to the primary. The model evolves on a thermal time scale of $\sim 10^7$ yrs and breaks contact when the inner contact surface is reached by the common surface of the stars. Following the idea of Rucinski (1973), Lucy (1976) and Flannery (1976) suggested that ZAMS W UMa binaries evolve by means of a series of periodic thermal relaxation oscillations (TRO) about a state of marginal contact as a result of being unable to achieve stable contact thermal equilibrium. After first breaking contact, the system evolves in the reverse direction, with mass transfer from the secondary to the primary. During this phase, the system is semi-detached so no energy transfer is possible. Nuclear evolution and angular momentum loss continue until contact is reached again, and the evolution of the system proceeds in cycles consisting of these two phases.

Lucy (1976) and Robertson and Eggleton (1977) stressed, however, that cycling models do not satisfy the observational requirements because in the semi-detached phase these systems should exhibit EB-type light curves and the duration of the contact and the semi-detached phases should be of the same order of magnitude for systems with average mass ratios of W-type systems. Therefore, it is expected that comparable numbers of short-period ($P < 0.4$ d) EB and EW stars should be observed. Lucy and Wilson (1979) searched for W UMa systems that appear to be in poor thermal contact (i.e. inclined to EB type) and found only three or four possible candidates, while more than a hundred EW systems in the same period range were found.

ASAS data on the distribution of bright variable stars shows equal numbers of systems where both eclipses have the same depth and systems where the two eclipses have different depths (Paczyński *et al.*, 2006; Pilecki *et al.*, 2007). These results provide qualitative

confirmation of the ideas of the thermal relaxation model where the binary oscillates between thermal contact, when the two eclipses have almost equal depth, and a semi-detached phase, when one eclipse is much deeper than the other.

2.8.4 Thermal Equilibrium Models

Biermann and Thomas (1972) constructed thermal equilibrium models with considerable entropy differences between the envelopes of the components. Although these models are in good agreement with Eggen (1967) period–colour relation, they fail to explain the equal light curve minima. Furthermore, Hazlehurst (1974), Hazlehurst and Refsdal (1980) and Rahunen (1981) showed that unequal entropy models are unstable on a short time scale and hence the evolution of these models is unclear.

2.8.5 Contact Discontinuity Model

Shu, Lubow, and Anderson (1976) postulated a contact binary structure different from TRO. They postulated that stars in contact develop a temperature discontinuity below the shared envelope in the less massive component. The magnitude of this discontinuity adjusts itself so that there is no net mass transfer between components. As a result the masses remain constant. This model is clearly wrong because it contradicts observations.

Chapter 3

Entropy Theory

3.1 Introduction

Clausius introduced the word Entropy in 1865. It is a thermodynamic variable. Boltzmann showed that there existed a relationship between the macroscopic variables of a system and its microscopic states. This relationship between entropy and the microscopic states of a system was facilitated by his development of statistical mechanics. Boltzmann showed that for a particular set of conditions thermodynamic equilibrium equated to maximum entropy.

Shannon (1948) extended the idea of entropy to information content, with minimum entropy corresponding to maximum information about a system.

In this chapter, the development of statistical mechanical concepts and the extension of these ideas to information and information transfer will be discussed. One of the aims of this section is to show that minimising the entropy (Shannon, 1948) of a set of symbols (or data points) maximises the information about the system. As will be described later in this chapter the definitions of entropy for statistical mechanics and information theory are different.

3.2 Statistical Mechanics

Systems of many particles are highly complex and are impossible to solve using the basic principles of physics even when the forces between atoms and molecules are known, (Reif, 1965). The interactions between particles are not normally of interest in engineering problems. It is the properties of the system as a whole which are important. Problems are usually studied from an equilibrium point of view, this is because equilibrium conditions represent an unchanging situation and lend themselves to theoretical study.

It is not the detailed behaviour of every particle in the system which is important then, so the laws and rules of statistics can be applied to these large numbers of particles to obtain the macroscopic dimensions and variables of the system. When statistics is applied to numbers are as large as Avogadro's number, i.e. of order 10^{23}, the macroscopic variables obtained are extremely accurate. The statistical mechanics definition of entropy S is (Reif, 1965)

$$S = k \ln \Omega(\alpha)$$

where $k = 1.38 \times 10^{-23}$ J K^{-1} is Boltzmann's constant and Ω is the number of microstates corresponding to a given macrostate specified by α. α could be described by quantities such as the volume V of a gas, its energy E, and the number of particles N in the sample.

Consider an isolated system in equilibrium consisting of N identical particles with a total energy E. The interactions of the particles must be conservative and so the total energy of a closed system must stay constant. There are many different ways in which the particle energies can be distributed meet the above conditions. The laws of mechanics do not favour one way over another and therefore each way is possible in statistical language. Each one of these ways is equally probable. So how many ways are possible?

Look at an isolated system with energy in the narrow range E to $E + dE$ and denote by $\Omega(E)$, the number of ways the system can arrange itself in this energy range. It was discussed above that this system can equally be found in any one of these arrangements.

Statistics asserts that the probability $P(E)$ that the system is in a state of energy E is:

$$P(E) = \frac{\Omega(E)}{\Omega_{total}}$$

where Ω_{total} is the total number of ways the system can arrange itself for all energies E and below.

If the energy E is changed, the system will be able to arrange itself in a different number of ways. The laws of statistics say that the system will be found in the energy range where it has the greatest number of ways of existing. This energy range will correspond to equilibrium and to the state of maximum disorder. Increasing the energy allows the system to become more ordered and reduce its entropy.

3.3 Information Theory

Entropy as it applies to communication was first introduced by Shannon (1948). Communication concerns the accurate transfer of information from a source to a receiver and Shannon[1] developed a method for measuring the information transferred. Hartley (1928) introduced the idea of logarithm of the size of the alphabet as a measure of information and Shannon showed that the logarithmic function was indeed the most natural choice for measurement of information in communication systems.

Shannon (1948) was the first to define entropy and mutual information, when he developed methods for analysing and coding information for transmission over communication systems. His communication system consists of an information source, a transmission channel and a receiver.

The definitions of information and entropy used in information theory are different to their meaning in physics, thermodynamics and language.

To Shannon (1948) information and entropy are functions specifying the probability of receiving the different alphanumeric characters in a set of alphanumeric characters which

[1] Carter (2011) was consulted when this theory was researched

he knew could be transmitted. If information transmitted by a particular source is received by many different observers the information they believe they have received will depend on the codes they are using. The observers who do not have the correct code and who use statistical methods based on the assignment of equal probabilities to the alphanumeric characters being received will clearly get a very different message to observers with the same code as the transmitter and who therefore assign the correct probabilities.

The entropy of information theory refers to the average amount of information received per symbol transmitted when symbols are transmitted over a communication network. This has nothing to do with the value of the information when the received symbols are assembled into a message. Its usefulness lies mainly in the fact that it permits the efficiency of a communication system to be predicted, especially in terms of how efficient its symbol coding systems are. The smaller the entropy in this case, the more efficient is the coding system. So again the objective is to minimise entropy.

Alphanumeric characters from a defined set are selected for transmission in Shannon's model. These characters are encoded and transmitted through the communication system to the receiver where it is decoded. It is important that the codes be uniquely decodable and efficient. Shannon (1948) defined information as follows:

> Information is the result of a choice; a given selection of letters of the alphabet is given a certain information value without reference to its meaning. That is "information" is defined as being distinct from "knowledge" for which there is no numerical measure.

Information theory tells us the following:

- How efficiently can information to be transmitted be encoded so that it can be uniquely decoded at the receiver?
- How the lower bound of encoding system efficiency is determined by the entropy.
- Since the largest amount of channel consumption for a given transmission code is indicated by the entropy for that code, better probability theorems must be developed in order to improve encoding algorithms.

- It is possible to encode the input symbols of a transmission system so the it can operate at almost full capacity and with error rates as low as required.

The fact that it is possible to use a transmission system so near to its full capacity is amazing. It is unnecessary to provide large amounts of error detection and correction algorithms, so according to Shannon, with proper design, error rates can be reduced to low values even when the system is being used at full capacity.

Shannon does not provide all the answers. He proves that an efficient code exists but the proof does not describe how to find this code. He also proves that in order to operate the system, with low errors at full capacity, large amounts of data must be encoded before it can be transmitted, greatly slowing transmission.

If the probability of a_i occurring is $p(a_i)$, and $\sum p(a_i) = 1$, the expectation value $\langle f(a) \rangle$ or average value of a function $f(a)$ is defined as

$$\langle f(a_i) \rangle = \sum_i p(a_i) f(a_i) \ .$$

Now let $f(a_i) = \log(1/p(a_i))$ then

$$\langle f(a_i) \rangle = \sum_i p(a_i) \log\left(\frac{1}{p(a_i)}\right) = -\sum_i p(a_i) \log(p(a_i)) \ .$$

Define a set of n independent symbols $A = \{a_1, a_2, \ldots, a_n\}$, which can occur with probabilities $\{p_1, p_2, \ldots, p_n\}$, respectively. The average amount of information received from the transmission of a list of N symbols, chosen from this list must be determined. From the above definition, the amount of information received from the observation of the symbol a_i is $\log(\frac{1}{p_i})$, therefore by the definition of probabilities this means that in a list of N symbols created from the list A one can expect to see $N \cdot p_i$ occurrences of the symbol a_i which represents $N \cdot p_i \cdot \log\left(\frac{1}{p_i}\right)$ units of information. Therefore, the total information received from the N transmitted symbols must be

$$I = \sum_{i=1}^{n} N \cdot p_i \cdot \log\left(\frac{1}{p_i}\right) \ .$$

Hence the average amount of information obtained per symbol observed must be

$$I/N = 1/N \sum_{i=1}^{n} N \cdot p_i \cdot \log\left(\frac{1}{p_i}\right) = \sum_{i=1}^{n} p_i \cdot \log\left(\frac{1}{p_i}\right)$$

where, because $\lim_{x \to 0} x \cdot \log(x) = 0$, $p_i \cdot \log(\frac{1}{p_i})$ can be defined to be 0 when $p_i = 0$.

Based on the above definitions, Shannon (1948) defined the entropy $S(p)$ in terms of the distribution of the probabilities p_i of A as

$$S(p) = \sum_{i=1}^{n} p_i \log\left(\frac{1}{p_i}\right) \ .$$

which means that the entropy is the average value of $\log(1/p(a_i))$.

The logarithmic measure of entropy can be justified axiomatically, as described below, by defining the properties of entropy measure (Carter, 2011).

When the probability is 0 or 1 there is no uncertainty and the entropy must be zero. When the probability is 1/2, maximum uncertainty exists and entropy must be maximum. Maximum uncertainty of course means the least information is available. So in order to reduce uncertainty and maximise information, entropy must be minimised.

Information measure is defined in terms of the probability p, of a particular symbol being observed, for example the letter A.

Information measure, $I(p)$, is required to have the following properties:

- Information must be positive, i.e. $I(p) \geq 0$.
- If the probability of a symbol occurring is 1, then $I(1) = 0$ i.e. no information available.
- If the probability of a symbol occurring is 0, then $I(0) = 0$ i.e. no information available.
- If two independent symbols a_1 and a_2 can occur with respective probabilities p_1 and p_2 then the probability of them both occurring is $p_1 \cdot p_2$, but the sum of the information obtained from observing both symbols must be $I(p_1 \cdot p_2) = I(p_1) + I(p_2)$.

- $I(p)$ must be continuous and monotonic.

Application of these rules yields the following relationships:

- $I(p^2) = I(p \cdot p) = I(p) + I(p) = 2 \cdot I(p)$
- $I(p^n) = n \cdot I(p)$
- $I(p) = I((p^{\frac{1}{m}})^m) = m \cdot I(p^{\frac{1}{m}})$, so $I(p^{\frac{1}{m}}) = \frac{1}{m} \cdot I(p)$ and $I(p^{\frac{n}{m}}) = \frac{n}{m} \cdot I(p)$ and so by continuity when $0 < p \leq$ and $a > 0$, a a real number: $I(p^a) = a \cdot I(p)$.

The above properties are satisfied by the logarithm (except $I(0)$). Therefore, it seems reasonable to define information measure $I(p)$ in terms of the logarithm; $I(p) = -\log_b(p) = \log_b(\frac{1}{p})$ for some positive constant base b. The base b determines the units we are using. The base b (and therefore the units) can be changed by using the logarithmic property; $\log_{b_2}(x) = \log_{b_2}(b_1) \cdot \log_{b_1}(x)$ for $b_1, b_2, x > 0$.

As an example, flipping a coin 100 times with each outcome having a probability of $\frac{1}{2}$ yields $-\log_2(\frac{1}{2})^{100} = 100 \log_2(2) = 100$ bits of information. This corresponds to the 100 binary digits (bits) which would be required to represent the results of the 100 flips. So 100 bits of information requires 100 binary digits to specify.

3.4 Properties of Entropy

In the next few paragraph the properties of $S(p)$ are investigated and the Gibbs inequality is used to show that that the entropy has a maximum value of $\log(n)$ where n is the total number of symbols, all symbols having equal probability $p = \frac{1}{n}$.

That is $S_{max} = \log n$ corresponds a situation where n symbols will be sent and this fact is all that is known about the transmission. So S_{max} corresponds to a situation of minimum information. Clearly the lower the value of Shannon entropy $S(p)$, the more is known about the transmission, so minimising the Shannon entropy maximises the amount of information about the set of symbols.

Since the tangent to $\ln(x)$ at $x = 1$ is the line $y = x - 1$ and since the gradient of $\ln x$ is negative, when $x > 0$, it must be true that $\ln(x) \leq x - 1$ with equality only when $x = 1$.

This means that given two probability distributions, $P = \{p_1, p_2, \ldots, p_n\}$ and $Q = \{q_1, q_2, \ldots, q_n\}$, where $p_i, q_i \geq 0$ and $\sum p_i = \sum q_i = 1$, it must be true that

$$\sum_{i=1}^{n} p_i \ln\left(\frac{q_i}{p_i}\right) \leq \sum_{i=1}^{n} p_i \left(\frac{q_i}{p_i} - 1\right) = \sum_{i=1}^{n} (q_i - p_i) = \sum_{i=1}^{n} q_i - \sum_{i=1}^{n} p_i = 1 - 1 = 0$$

with equality only when $p_i = q_i$ for all i.

The properties of the Gibbs inequality provide a way of finding a distribution of probabilities which allows the entropy function to achieve a maximum value. Given the probability distribution $P = p_1, p_2, \ldots, p_n$ with the same properties as above. Consider the following:

$$\begin{aligned}
S(p) - \log(n) &= \sum_{i=1}^{n} p_i \log\left(\frac{1}{p_i}\right) - \log(n) \\
&= \sum_{i=1}^{n} p_i \log\left(\frac{1}{p_i}\right) - \log(n) \sum_{i=1}^{n} p_i \\
&= \sum_{i=1}^{n} p_i \log\left(\frac{1}{p_i}\right) - \sum_{i=1}^{n} p_i \log(n) \\
&= \sum_{i=1}^{n} p_i (\log\left(\frac{1}{p_i}\right) - \log(n)) \\
&= \sum_{i=1}^{n} p_i \left(\log\left(\frac{1}{p_i}\right) + \log\left(\frac{1}{n}\right)\right) \\
&= \sum_{i=1}^{n} p_i \left(\log\left(\frac{1}{n\, p_i}\right)\right)
\end{aligned}$$

The Gibbs inequality states that

$$\sum_{i=1}^{n} p_i \left(\log\left(\frac{1}{n\, p_i}\right)\right) \leq 0$$

which can be applied to the previous expression to give $S(p) - \log(n) \leq 0$, and equality

is achieved for only one value; $p_i = \frac{1}{n}$ for all i. Therefore we get the important inequality

$$0 \leq S(p) \leq \log(n) \ .$$

From the above we get that $S(p) = 0$ when exactly one value of $p_i = 1$ and all the rest are zero. Furthermore, $S(p) = \log(n)$ only when all the symbols have exactly the same probability $p_i = \frac{1}{n}$. Clearly, the maximum value of the entropy function is $\log(n)$ where n is the number of possible symbols, and it occurs when all the events are equally likely.

Chapter 4

Application of Minimum Entropy

4.1 Introduction

W UMa stars are known to undergo period changes, the origin of which is still uncertain but could be related to their evolution. Therefore, it is important to be able to measure the period accurately and determine whether it is changing with time, and if so by how much.

The task of obtaining an accurate shape and period for a light curve of a variable star is not always easy. Astronomical measurements are often unevenly sampled and incomplete. Brightness measurements are distorted by temperature and atmospheric density variations which affect the measured values, causing errors in the measured brightness values.

Cincotta, Mendez, and Nunez (1995) showed that information entropy can be used to identify periods in astronomical times series data and Cincotta *et al.* (1999) did a mathematical analysis of the method of minimisation of entropy and showed that it could be used to extract two periods from simulated data which normal Fourier methods could not. Deb and Singh (2011) used the technique of minimum entropy to determine the period of 62 binary stars in the ASAS database for which mass determinations are known from radial velocity measurements.

This chapter discusses how a minimum entropy method has been implemented using a programme written in Python to determine the period of EW light curves. The programme uses data from the publicly available ASAS database which is described in the next section.

4.2 Method of Minimisation of Entropy

As discussed in chapter 3, information theory considerations point to the fact that minimum Shannon entropy corresponds to maximum information. Entropy is a measure of chaos, lack of order or lack of information, the more ordered a system is, the lower it's entropy and the more is known about it. Entropy is also therefore a statistical measure which can be quantitatively evaluated and because of this, the more system data points available the more accurate the entropy calculation will be.

Consider a large collection of points on a pure sine wave, evenly spread over a large number of periods, plotted on a horizontal time axis. Because each complete cycle of the sine wave is identical to every other cycle, corresponding points of each cycle are said to correspond to a specific and identical phase. Therefore a time series of the sine wave can be converted to a PMD in exactly the same way as described later in section 4.3 for EW light curves. An example of a pure sine wave time series folded on its true period producing a curve consisting of only one cycle in the phase–magnitude plane is shown in Fig. 4.1. This is clearly a state of great order. If, however, the period used to calculate the phase of each point of the sine wave is incorrect, the phases of corresponding points will not be identical and when the points are plotted on a phase axis, a neat sine wave will not result. Instead a diagram with data points spread fairly uniformly over it will be produced and the sine wave will not be evident. This can be clearly seen in the sine wave series Fig. 4.2 to Fig. 4.8. These diagrams correspond to states of increasing disorder.

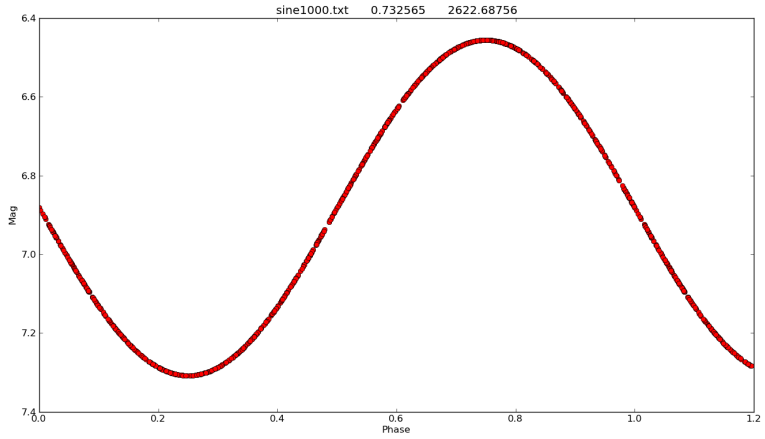

Figure 4.1: Sine wave with a period of 0.732565 made up of 1000 points.

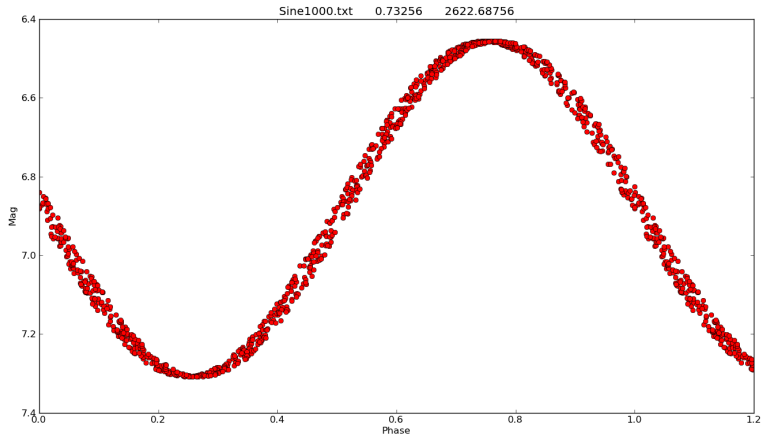

Figure 4.2: The following series of diagrams Fig. 4.2 to Fig. 4.8 shows sine waves folded on periods increasingly far from the true period.

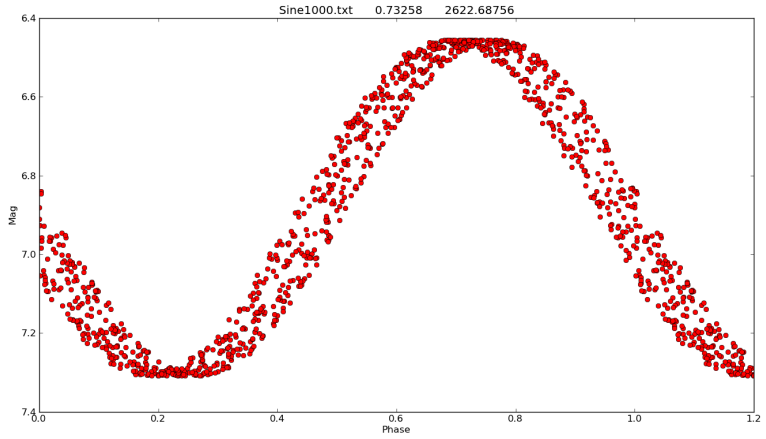

Figure 4.3

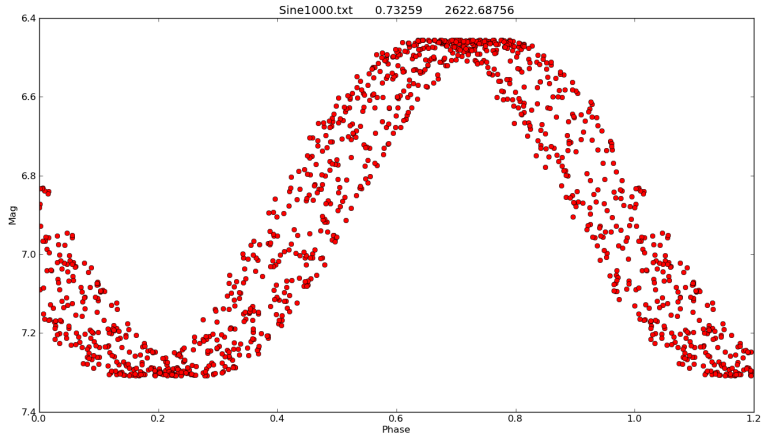

Figure 4.4

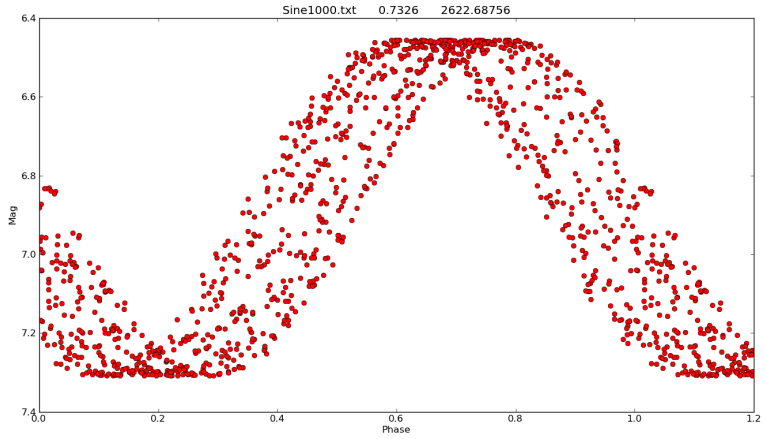

Figure 4.5

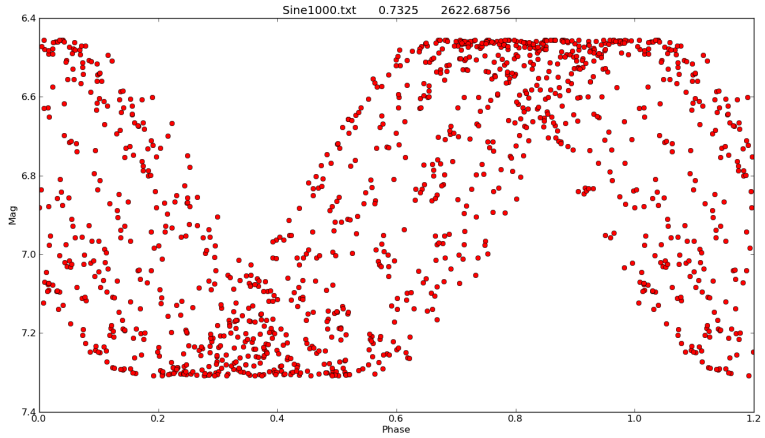

Figure 4.6

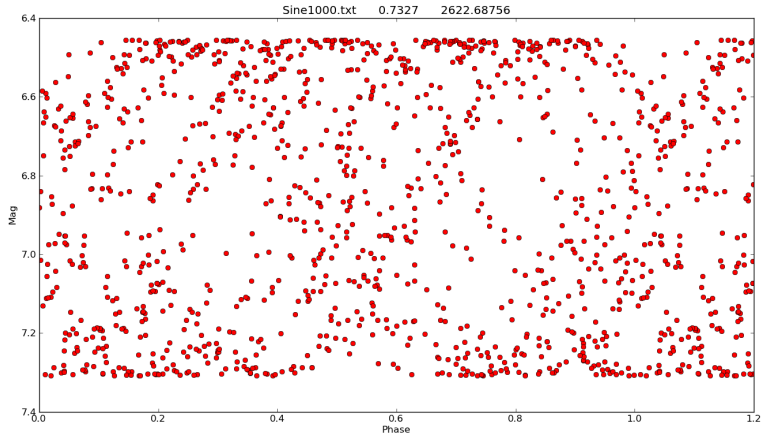

Figure 4.7

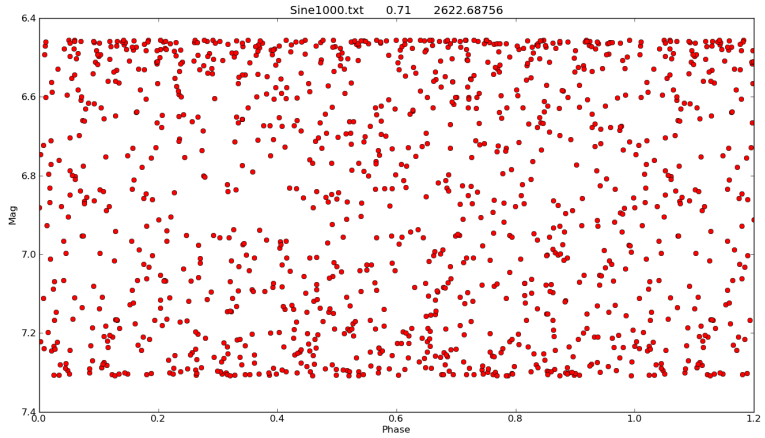

Figure 4.8: Sine wave folded on a period far from its true period and is unrecognisable.

When an incorrect period is used for folding a light curve, the data are spread widely over the phase–magnitude plane. A state of disorder exists and it can be expected that this state constitutes a state of relatively great entropy. When the correct period is used for folding the data, a varying light curve should be apparent, corresponding to a state of great order. Under this condition we expect to calculate the minimum entropy value.

Following the above example, the minimum entropy method of determining the period of the variable stars is facilitated by dividing the phase–magnitude plane into a grid of equal sized rectangles with no spaces in between them. Each rectangle is called a bin and has a label assigned to it. The data in the plane are then examined with respect to these bins.

The formula used by Cincotta, Mendez, and Nunez (1995), Cincotta *et al.* (1999) and Deb and Singh (2011) to calculate the entropy S is based on the Shannon information theory (Shannon, 1948) definition of entropy which is given by

$$S = -\sum_{i=1}^{n}\sum_{j=1}^{m} \mu_{ij} \ln(\mu_{ij}) \quad \text{for} \quad \mu_{ij} \geq 0 \tag{4.1}$$

where μ_{ij} is the normalised number of points or the probability of finding a point in a particular bin labelled ij of the light curve phase–magnitude plane. As described in the above sine wave example the method of minimum entropy always requires that the time information be converted to phase. However, the amplitude information, or brightness information in the case of light curves, can be expressed in units of flux, normalised flux or normalised magnitude. For this MSc minimum entropy programs using Python programming language were produced using all three of these amplitude units and gave identical results. The Python routine normalises magnitudes automatically, without operator intervention, by dividing by the largest magnitude value.

The phase axis is divided into n subdivisions and the normalised magnitude (n_{mag}) axis is divided into m subdivisions. In this manner the phase–n_{mag} plane is divided into $n \times m$ bins each having dimensions of $1/n \times 1/m$. Each bin is identified by the coordinate pair (i, j), where i represents the phase coordinate of the bin and j represents the magnitude coordinate of the bin. The number of data points (or observations) that lie in element (i, j) is divided by the total number of data points and is denoted by the variable μ_{ij}. The entropy S for each period P is calculated using formula 4.1.

When the data points are spread evenly over the phase–magnitude plane then each of the $n \times m$ elements in the plane will contain an equal number of data points, and the entropy S will have its maximum value. If there are N data points in total, then each element

will contain N/nm points and

$$\mu_{ij} = \frac{N}{mnN} = \frac{1}{mn} \ .$$

Substitute this into equation (4.1) and sum over i and j to get

$$S_{max} = -nm \ \left(\frac{1}{mn}\right) \ln\left(\frac{1}{mn}\right) = \ln(nm) \ .$$

A normalised entropy S_{norm} can be written as

$$S_{norm} = \frac{S}{S_{max}} = \frac{\left[-\sum_{i=1}^{n}\sum_{j=1}^{m}\mu_{ij}\ln(\mu_{ij})\right]}{\ln(nm)}. \tag{4.2}$$

This is the equation used by Sharma and Johnston (2009) in their paper on a group finding algorithm for multidimensional data sets.

4.3 The Data

The All Sky Automated Survey[1] (Pojmanski, 2000), ASAS, has two observatories, one in Las Campanas, Chile, which has been operating since 1997, and the other in Haleakala, Maui, which has been collecting data since 2006. The observatories are equipped with two wide-field 200 mm f/2.8 lenses attached to CCD cameras on mounts that track the sky at the sidereal rate. The telescopes observe simultaneously through V and I band photometric filters. A 3 min exposure is taken of a patch of sky and the telescope is then moved to another patch and the next exposure is taken. In this way, the southern telescope covers the sky from a declination of $\delta = +28°$ all the way to the South Pole in about three days. This means that for any star, a brightness measurement is obtained at most once every three days, but because of cloud and other factors the actual number of observations is reduced. However, by looking at the time-series data collected over several years, ASAS has produced extensive catalogues of variable stars with magnitudes in the range $8 \leq V \leq 13$. About 80% of the detected stars are not listed in the GCVS, and

[1] http://www.astrouw.edu.pl/asas

therefore are new discoveries. All photometric V-band data of the southern hemisphere up to December 2009 are currently (August 2014) available, and can be accessed and downloaded over the internet using a web browser.

The ASAS data contain a Heliocentric Julian Day (HJD) time stamp for each data point together with calibrated V band magnitudes with uncertainties determined for four different apertures. The magnitude data are arranged with what they estimate to be the most accurate data in the first column. They also assess the quality of the data, giving each point a rating in four categories labelled A for best, B for reasonable, and C and D which are not reliable. For each variable star, once sufficient data have been collected, ASAS has used an automated algorithm to determine a period P and an epoch of primary minimum T_0, and they have suggested what type of variable it is based on its period and the shape of the folded light curve. The data are cross-correlated with other databases such as the GCVS and 2MASS. The ASAS period is used to fold the data to produce a phase–magnitude diagram (PMD) for each star in its database.

EW light curves have periods less than a day, and therefore between consecutive points of ASAS data it is not possible to ascertain what the shape of the light curve looks like, or what the star's period is. From the time of minimum T_0 to the next observation, the star varies through an integral number of cycles and a fraction of a cycle. The fraction of the cycle is called its phase and varies between 0 and 1. Because contact binaries are in circular orbits, at phase 0.5, an EW light curve is at its secondary minimum while phases 0.25 and 0.75 correspond to the two maxima. The phase ϕ for an observation taken at an arbitrary time T is calculated using

$$\phi = \frac{(T - T_0)}{P} - \text{the integer part of } \left\{ \frac{(T - T_0)}{P} \right\} .$$

Note that it is standard practice in binary star work to normalise the phase axis so that it extends from 0 to 1, rather than expressing the phase in terms of 2π radians or 360° degrees. Sometimes the phase axis is drawn from –1 through 0 to +1 or from 0 to 2 so that two cycles are represented. For eclipsing binaries, the primary minimum of the light curve is chosen as phase 0.

After downloading data from ASAS for chosen contact binaries, the data needs to be

cleaned before it is processed. Using a programme written by Skelton (private communication), the file is opened and the A and B rated data for the aperture that ASAS estimate to be the best are extracted, together with the timestamp in HJD. Even though this is classified as good data, there are still points that are clearly outliers and need to be removed. The cleaning programme provides a graphical user interface to remove these noisy data points which lie above or below the mean curve. The cleaning programme can be run more than once if it is required to remove points after processing. The clean data is used in the minimum entropy programme. Fig. 4.9 shows a typical ASAS light curve before cleaning and Fig. 4.10 shows the same light curve after cleaning. With the noisy data removed the magnitude scale of the light curve increases so that the points on the light curve appear to be further apart.

4.4 Python Minimisation of Entropy Program

Python programs were written for this MSc using equation (4.2) to calculate the entropy in the phase–magnitude plane of cleaned ASAS EW data. The method of minimum entropy has the advantage that it can work with unevenly sampled data. Minimum entropy is found by calculating the entropy of the data for a range of periods around the ASAS period and reporting the period corresponding to the lowest value of entropy.

A number of different versions of the Python ME programme were written. One of these versions allows the user to select the range of periods around the ASAS period which the programme searches for minimum entropy. This version is useful when it is discovered (by examining the period - entropy plot output by the programme) that the period estimated by ASAS is far from the period to which the ME programme would converge or when the period of the light curve is very large. However when the user inputs the period range the programme will normally have to be run a number of times before the user gets the correct time resolution for satisfactory accuracy of period determination.

A result is obtained much more quickly if the version of the programme used has a pre-set period range around which it searches. The version of the Python code, with a pre-set period search, works as follows; the initial trial period for which the programme calculates

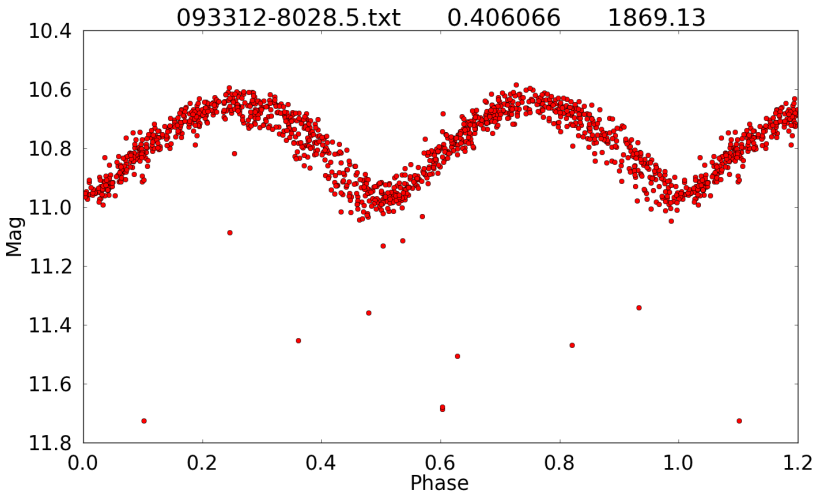

Figure 4.9: Light curve plotted with raw ASAS data.

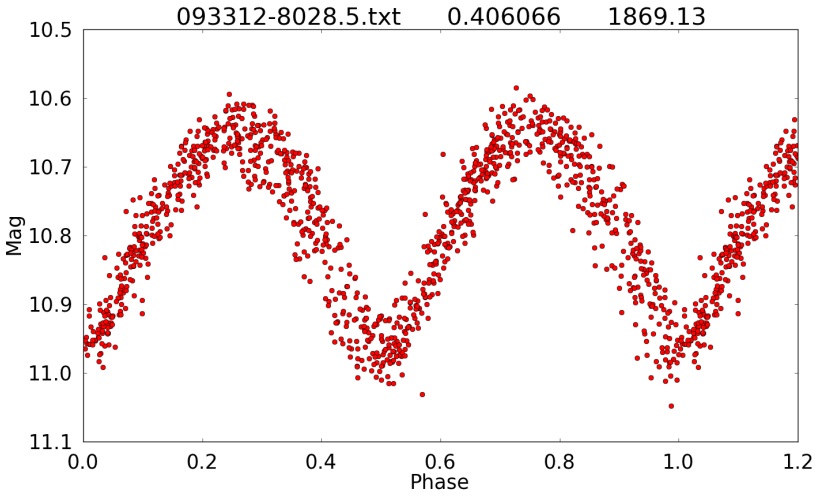

Figure 4.10: Light curve with clean ASAS data.

the entropy is the ASAS period with the least significant digit reduced by a value of 5. The programme then increments the trial period by a value of 0.1 x the order of the least significant digit and again calculates the entropy. The programme repeats this process until the least significant digit of the ASAS period has been increased by 5. For example if the ASAS period were 0.364879 d the initial trial period would be 0.364874 d and the final trial period would be 0.364884 d. This process requires 100 iterations. This automated period search range is generally adequate for the accuracy of the periods reported by ASAS.

The programme requires the file name of the cleaned ASAS data, the period P and the epoch of minimum T_0 determined by ASAS. The number of divisions, n and m, into which the phase and magnitude axes are divided must be entered. Chapter 5 includes a discussion regarding the sensitivity of the accuracy of the period detemined by the ME programme to the values assigned to n and m. The conclusion of this discussion resulting in the recommendation that both n and m be set to 50.

The minimise entropy program has three main outputs: the period P_{ME} at which the entropy is a minimum, a graph of the entropy versus period that has been calculated, and a phase–magnitude plot of the light curve folded on the period P_{ME} determined by the programme. Fig. 4.11 and Fig. 4.12 show a graph of entropy versus period for a 1064 data point sine wave and the corresponding light curve folded on the resultant period at minimum entropy. Similarly Fig. 4.13 to Fig. 4.16 show the entropy–period plots for the two ASAS stars YY Eri and SZ Hor and their corresponding light curves, folded on the minimum period determined from these entropy–period plots. Above each PMD, the programme prints out the star ID, the period used to generate the plot, and the Modified Julian Day, MJD, where MJD = HJD – 2450000.

The application of this programme to real data is discussed in the next chapter.

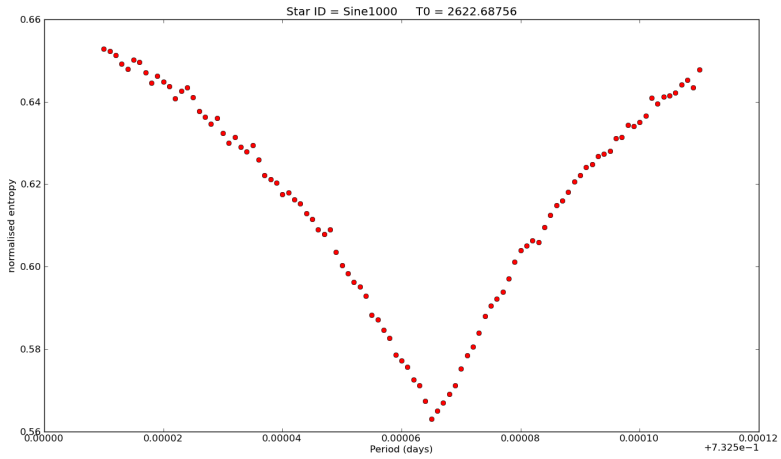

Figure 4.11: Period - Entropy plot for a 1064 data point sine wave

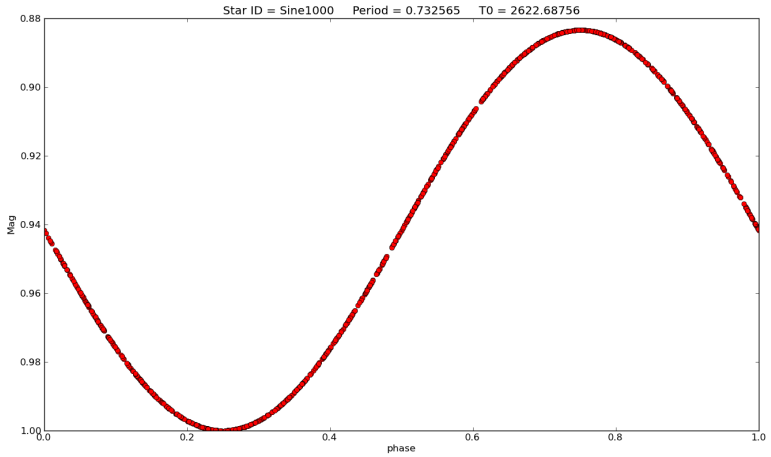

Figure 4.12: Sine wave folded on period determined by ME programme.

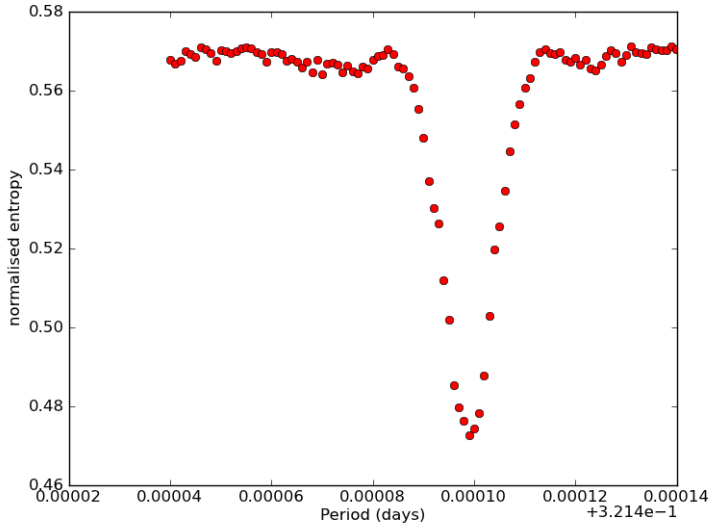

Figure 4.13: Period - Entropy plot for YY Eri.

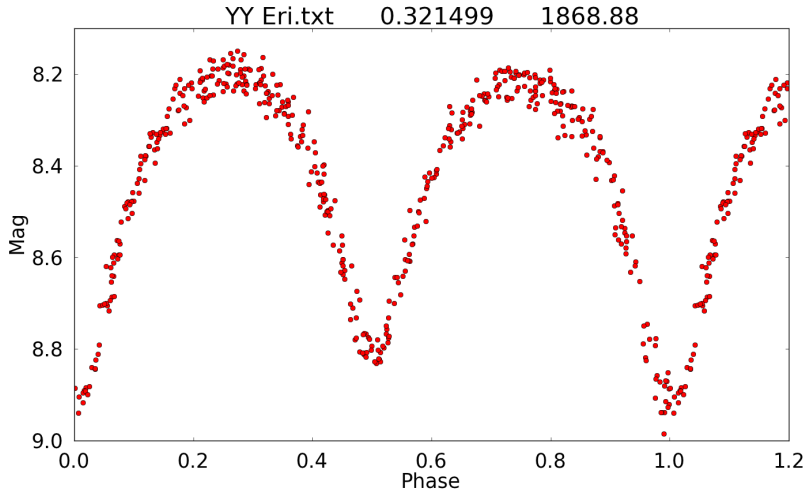

Figure 4.14: Light curve of YY Eri folded on the ME period.

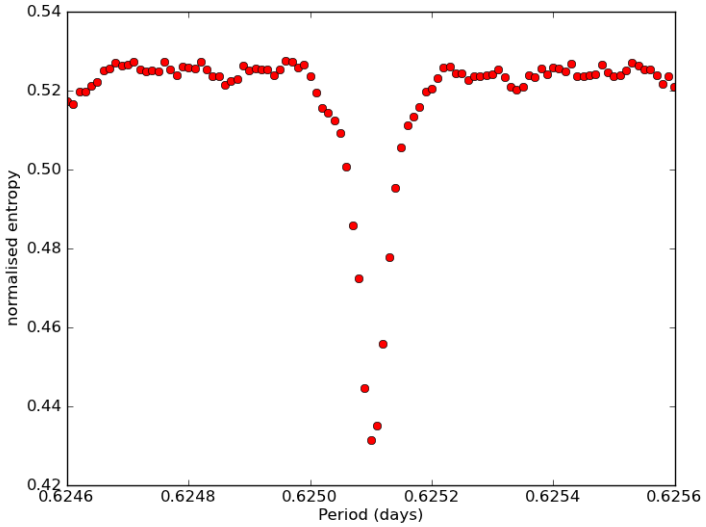

Figure 4.15: Period - Entropy plot for SZ Hor.

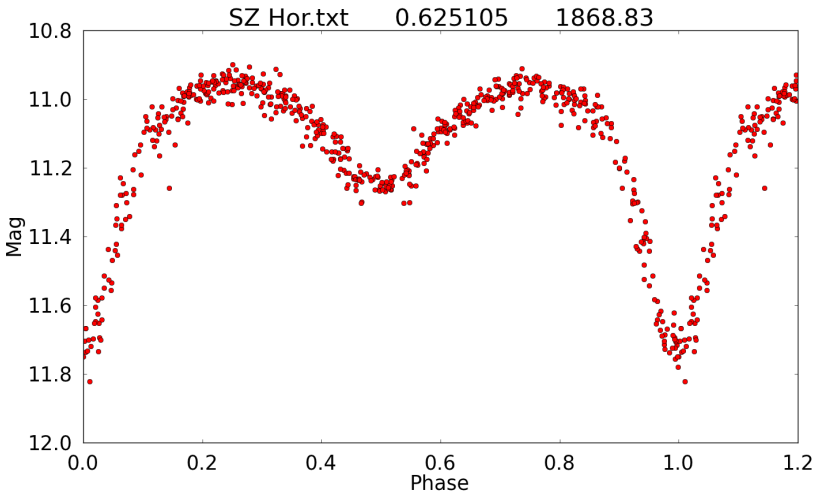

Figure 4.16: Light curve of SZ Hor folded on the ME period

Chapter 5

Testing and Applying the Python Code

5.1 Introduction

The number of useful data points obtained for each star in the ASAS database varies widely. This is a factor which impacts the accuracy of the periods which can be determined for a variable star. In this chapter the minimum entropy (ME) programme is used to investigate the effect on the period determined by the program, of changing the number of data points available and changing the number of divisions along each of the phase–magnitude plane axes.

There is a price to be paid for increasing the number of elements because the time required to run the ME programme increases dramatically with the number of elements.

5.2 Sensitivity to Number of Magnitude Elements

In the ME programme, the phase–magnitude plane is divided into $n \times m$ bins where n and m are any positive integers. This raises the question: Is there an optimum number of subdivisions or bins required to achieve an acceptable level of accuracy when determining the period of EW light curves, and is there a minimum number of data points required for the programme to work effectively?

5.2.1 Testing ME Programme Accuracy Using Sine Waves

Cincotta, Mendez, and Nunez (1995) compared their results using $8 \times 8 = 64$ elements with the results obtained using $4 \times 4 = 16$ elements for a simulated light curve. In both these cases the true period was detected. The authors noted that the 64 element division produced more harmonics of the true period than did the 16 element division.

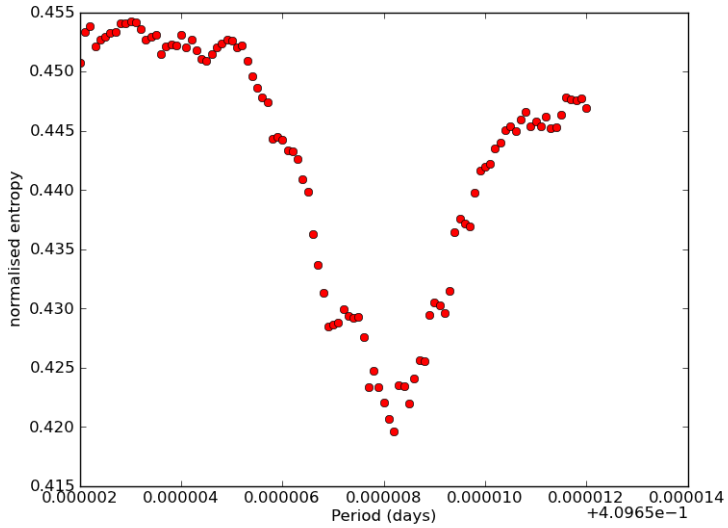

Figure 5.1: Typical ragged edged period–entropy diagram

The normalised entropy does not decrease smoothly nor monotonically as the test period approaches the true period of the pure sine wave (or variable star), but instead approaches it in small increasing and decreasing random steps, Fig. 5.1. Increasing the number of elements in the unit phase–magnitude plane does not result in a continuous reduction in the minimum entropy of the associated period of the variable star, nor does it result in a continuous approach to a specific value of period.

In order to have a control for calculation and graphical comparison purposes, computations were performed on two perfect sinusoids with periods of 0.732565 d and 0.389172 d. The 0.389172 d sinusoid was tested with a number of data points near the lowest, roughly halfway between the lowest and second lowest and a number of data points equal to the

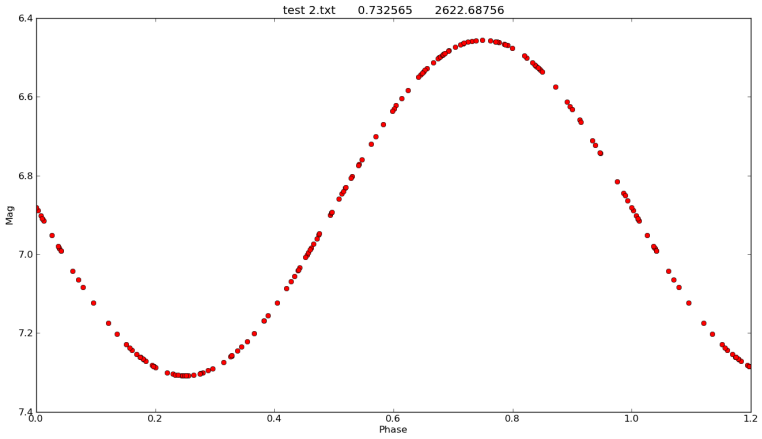

Figure 5.2: A PMD of a pure sine wave with a period of 0.732565 d consisting of 157 data points.

second highest (50, 97 and 337 respectively) of the 0.732565 d sinusoid number numbers of data points. The objective was to determine if there was any significant deviation with the lower intermediate number of data points for the higher frequency sinusoid. It was not considered necessary to repeat the excercise with the larger number of data points (1064) used for the low frequency sinusoid because not many of the ASAS data files contains such high numbers of data points and it was considered that the results of the investigation confirmed that such high numbers of data points ensured high accuracy for the ME method.

Figs. 5.2 and 5.3 show the PMD of a pure sine wave with a period of 0.732565 days. Fig. 5.2 is plotted using 157 points and Fig. 5.3 has 1000 points. The points are randomly distributed across all phases of these curves in a manner similar to real data from ASAS stars.

The tests carried out on the pure sine waves are illustrated in Figs. 5.4 and Fig. 5.5. In Fig. 5.4 with 50 magnitude subdivisions the period stabilises around $m = 50$ phase subdivisions. For $m < 50$ the period varies by less than 10^{-5} d which means the period is accurate to five significant figures. The variation is largest for the data set with only 50 points and improves as the number of data points increases.

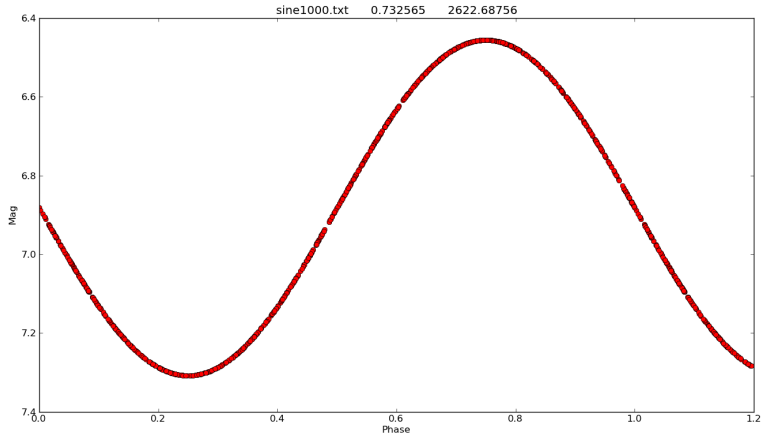

Figure 5.3: A PMD of a pure sine wave with a period of 0.732565 d consisting of 1000 data points.

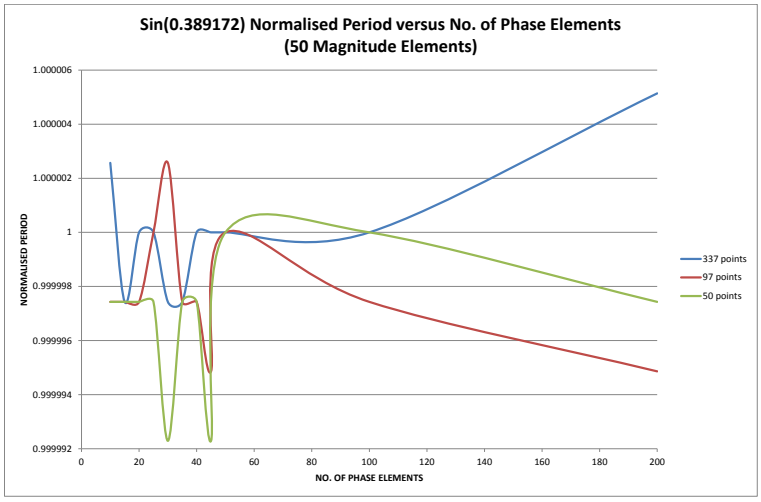

Figure 5.4: Plot of ME period versus number of phase elements for perfect sine waves, of period 0.389172, with 50, 97 and 337 data points.

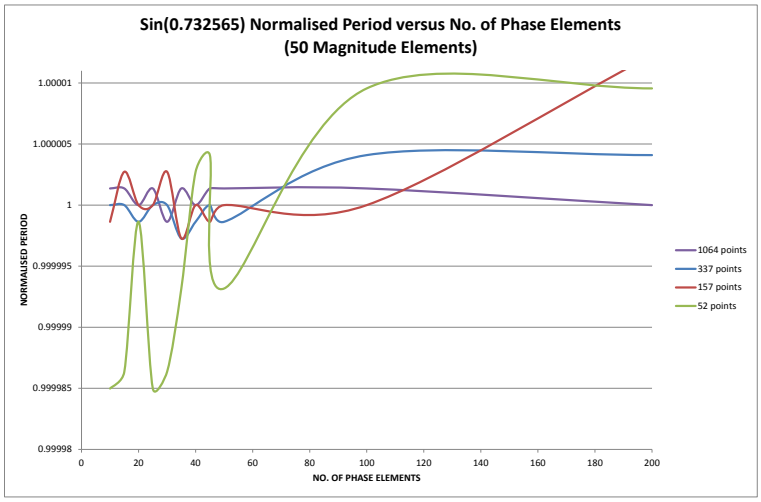

Figure 5.5: Plot of ME period versus number of phase elements for perfect sine waves, of period 0.732565, with 52, 157, 337 and 1064 data points evenly distributed over the phases of the sine wave.

The same pattern is seen in Fig. 5.5. With only 52 points in the data set, the period varies by nearly 2×10^{-5} d and the period with 200 phase elements lies above 1. This is not unreasonable considering that with 50 data points, only 1 out of every 4 phase bins will contain a data point. This clearly demonstrates that working with too few points is going to lead to inaccurate results. When 1064 points are used, the ME programme resolves the period accurately even with less than 50 phase bins. However few of the ASAS data files investigated had such high numbers of data points.

5.2.2 Testing ME Programme Accuracy Using ASAS Data

The next step is to look at real data and compare it to the results obtained with a pure sine wave. In Fig. 5.6 the normalised ME period is plotted against the number of phase elements used by the ME program in the determination of this period, for a pure sine wave with a period of 0.732566 d and for ASAS 204628–7157.0 (MW Pav) with an ASAS

period of 0.795 d. The sine wave has 1064 data points and the ASAS source has 1040 data points. The sine waves are pure oscillations with no noise. Real data of course contains noise which makes the determination of the ASAS binary periods more difficult. For $m < 50$ there are small variations of the period amounting to changes of less than 10^{-5} d for both sets of data. The pure sine wave varies by less than the ASAS source, but for $m > 50$ the results are stable and the periods are close to the normalised value.

The above results, and the fact that the normalised magnitudes processed by the Python programme vary between only 0 and 1, lead to the conclusion that 50 magnitude elements is more than sufficient for the accurate determination of the light curve period. The Python program for the remainder of the investigation was therefore preset to 50 magnitude divisions.

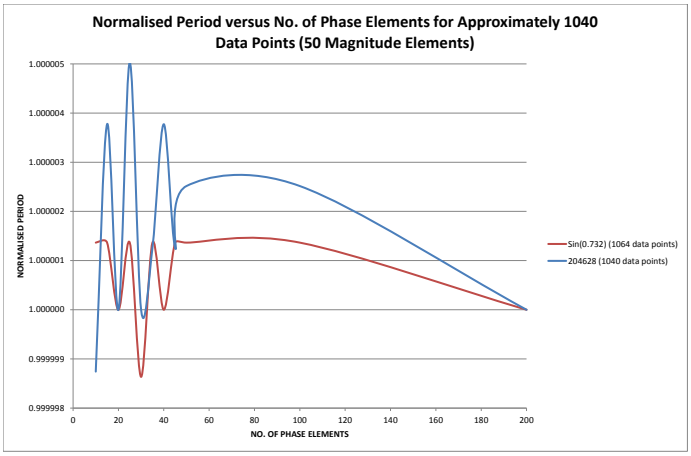

Figure 5.6: ME Period versus number of phase elements for ASAS 204628–7157.0 and a perfect sine wave with approximately 1040 data points and 50 magnitude elements.

In order to compare the periods of different stars on the same graph it is necessary to normalise their periods. From the results of Fig. 5.6 it is reasonable to adopt the period used to normalise ASAS 204628–7157.0 as the normalising period for all sine waves and other ASAS stars plotted on the same graph as ASAS 204628–7157.0. The period

determined for ASAS 204628–7157.0 by the ME program is $P = 0.794993$ d. The light curve folded on this period is shown in Fig. 5.7.

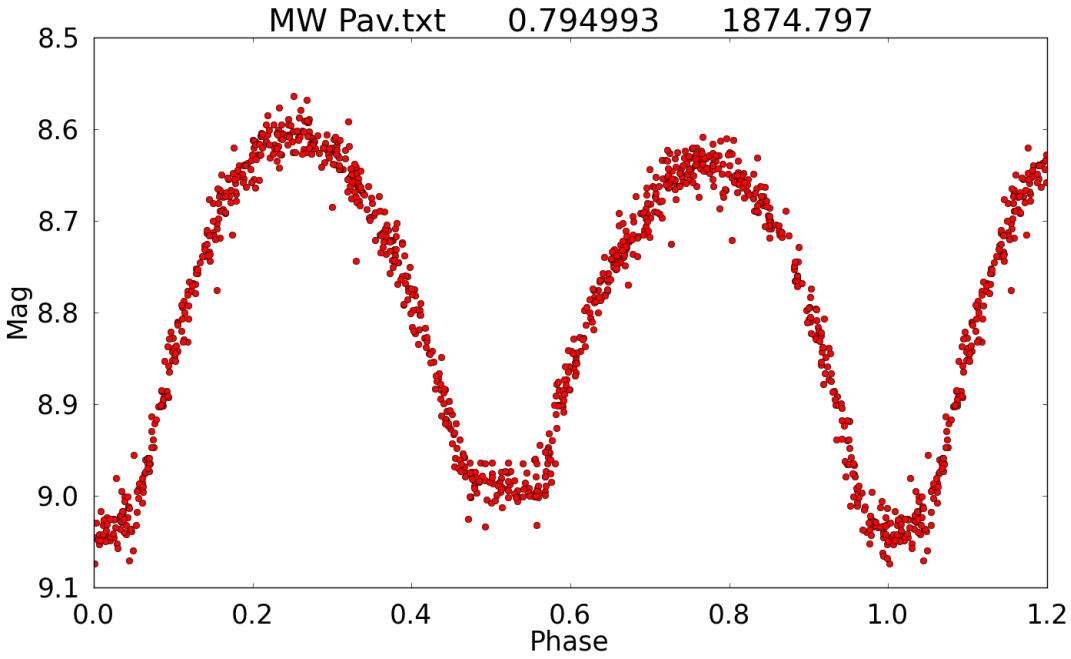

Figure 5.7: Light curve of ASAS 204628–7157.0 (MW Pav) folded on a period of 0.794993 d.

The effect of the number of data points on the calculation of the period by the ME programme was done as follows. Starting with the original number of ASAS data points, noisy data was removed to create a set of clean data points. The Python ME program was used to compute the variable star period. This was followed by the removal of data points from the clean data set, and the period was calculated again. This process was repeated until the period started to deviate substantially from the value calculated with the full data set. When points were removed, this was done in a way that ensured the remaining data were spread uniformly across the phase–magnitude plane. To determine the period, the number of subdivisions on the magnitude axis was kept at $m = 50$ while the number of subdivisions n on the phase axis were varied. The results of these tests are presented in Table 5.1.

Table 5.1: The period of ASAS 204628–7157.0 calculated with the ME programme using $m = 50$ subdivisions on the magnitude axis and a varying number of subdivisions n on the phase axis for a range of data points N. The number of subdivisions on the phase axis are labelled by n, and the period P in days for N = 145, 353, 499, 735 and 1034 data points are labelled as P(N).

n	$P(145)$	$P(353)$	$P(499)$	$P(735)$	$P(1034)$
10	0.795008	0.795007	0.795024	0.795017	0.795029
15	0.795008	0.795007	0.795024	0.795017	0.795029
20	0.795008	0.794997	0.794993	0.794993	0.794993
25	0.795008	0.794991	0.794993	0.794995	0.794993
30	0.794984	0.794991	0.794993	0.794993	0.794993
35	0.794995	0.794991	0.794993	0.794994	0.794993
40	0.794996	0.794991	0.794993	0.794993	0.794993
45	0.794997	0.794997	0.794993	0.794993	0.794993
50	0.795008	0.794991	0.794991	0.794993	0.794993
100	0.794997	0.794994	0.794993	0.794993	0.794993
200	0.794997	0.794993	0.794993	0.794993	0.794993

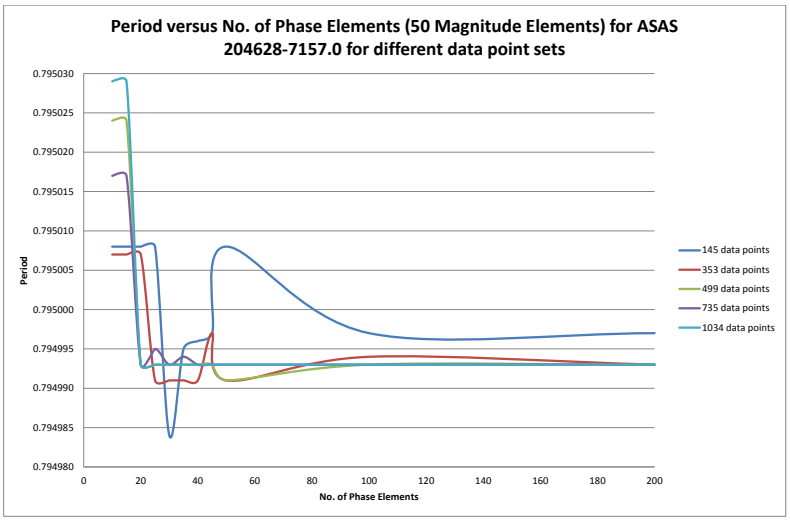

Figure 5.8: A plot of the results of Table 5.1

Plots of period versus number of phase elements for several ASAS sources with ~ 350 data points and ~ 500 data points are shown in Figs. 5.9 and 5.10. From these it is clear that the more data points are used, the better are the period estimates. If there are less than 50 subdivisions on the phase axis, results are scattered by about 10^{-5} of the normalised period. In order to plot a graph of the normalised period versus number of phase elements for each star and for each of the two sine waves, the Minimum Entropy program was used calculate the ME period for each of the binning combinations shown in column m of Table 5.1 with the number of magnitude elements kept constant at 50. The mean value of all these ME periods was then calculated for each star or sine wave and this mean value was used to normalise all the ME periods for the corresponding star or sine wave. When all the periods have been normalised in this manner, it is possible to compare, on the same graph, stars with different periods.

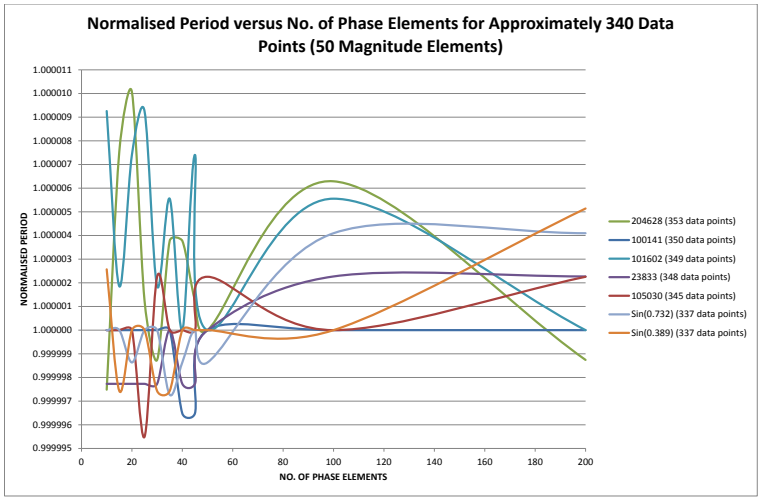

Figure 5.9: ME Period versus number of phase elements for a selection of ASAS binaries and perfect sine waves with approximately 340 data points and 50 magnitude elements. The data points are spread as evenly as possible over all phases

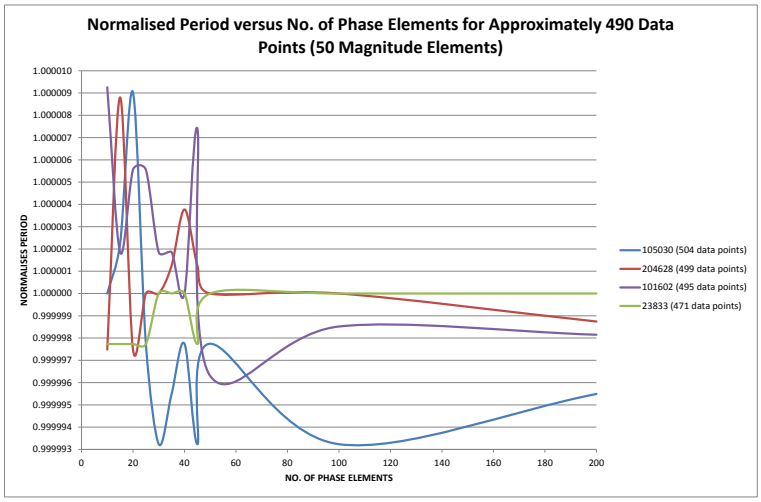

Figure 5.10: ME Period versus number of phase elements for a selection of ASAS binaries with approximately 500 data points and 50 magnitude elements.

The divisions of the phase–magnitude plane that were investigated were as follows:

- Keeping the number of phase divisions constant at 50, the number of magnitudes divisions is increased from 10 to 200.
- In a similar fashion, the number of magnitude divisions was kept constant at 50 while the number of phase divisions increased from 10 to 200.

The results for the 1040 data points of ASAS 204628–7157.0 are shown in Table 5.2.

Table 5.2: Variation of period as function of the number of elements in the phase–magnitude plane for ASAS 204628–7157.0. The columns labelled n and m list the number of subdivisions of the phase and magnitude axes respectively, and P is the period returned by the ME programme.

n	m	P [d]	n	m	P [d]
50	10	0.794990	10	50	0.795029
50	15	0.794994	15	50	0.795029
50	20	0.794991	20	50	0.794993
50	25	0.794995	25	50	0.794993
50	30	0.794991	30	50	0.794993
50	35	0.794992	35	50	0.794993
50	40	0.794994	40	50	0.794993
50	45	0.794992	45	50	0.794993
50	50	0.794993	50	50	0.794993
50	100	0.794993	100	50	0.794993
50	200	0.794991	200	50	0.794993

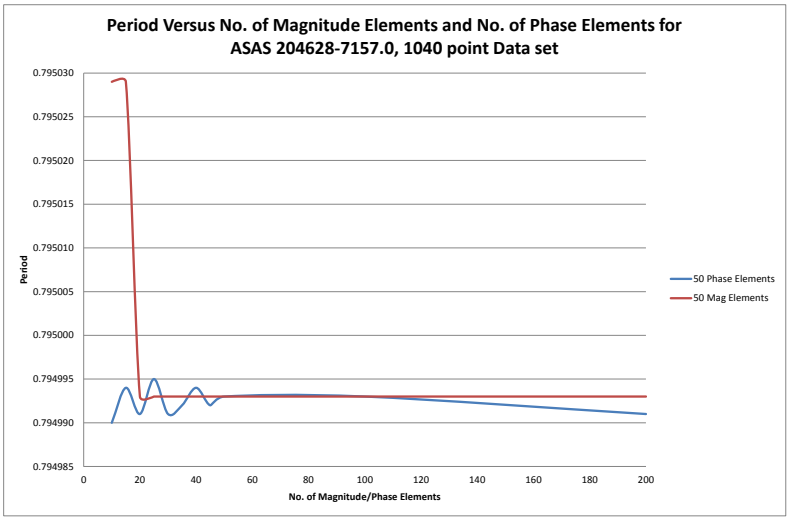

Figure 5.11: A plot of the results of Table 5.2

In actual fact accurate periods can be determined for a far coarser division of the phase–magnitude plane as shown by Cincotta, Mendez, and Nunez (1995) and as can be seen from some of the results of this investigation. However the graphs show that if a sufficient number of well distributed data points are available, the period remains substantially constant for 50 or more phase and magnitude elements. It is reasonable then, in order to keep computing time to a minimum and to maximise accuracy of the calculated periods, to divide the phase–magnitude plane into 50×50 segments.

5.3 Comparison with the Results of Deb and Singh (2011)

Deb and Singh (2011) were the first researchers to conduct a thorough study of the determination of ASAS periods using the ME method. Their results for 62 variable stars therefore provided a good yardstick against which to measure the effectiveness of the Python programme written for this dissertation. The periods determined by ASAS and the periods determine by Deb and Singh (2011) for these 62 stars were compared against the periods determined by the Python minimum entropy programme. The results are shown in Table 5.3.

Deb and Singh (2011) selected 62 eclipsing binary stars for their study from the ASAS data base. Their selection criteria were; reasonably clear light curves, ASAS data files containing between 96 and 1221 data points and accurate mass ratio's had previously been determined for them by other researchers, notably Rucinski and Lu (1999). Not all the Deb and Singh (2011) stars were W UMa stars (A-type and W-type). TZ Pyx (ASAS 084108–3212.1) and MR Del (ASAS 203113+0513.2) are detached binaries. DD Mon (ASAS 064558–0017.5), V753 Mon (ASAS 071058–0352.8), PY Vir (ASAS 131032–0409.5), HT Vir (ASAS 134607+0506.9), EL Boo (ASAS 144803+1356.7) and V2610 Oph (175332–0354.9) are all semi-detached binary stars.

As can be seen in table 5.3 the value of the period for Y Sex (ASAS 100248+0105.7), apparently determined by the authors, appears to be significantly different to the values determined by ASAS and by the Python programme. However the Deb and Singh (2011)

period is clearly a typographical error as their period is exactly the same as the period of XZ Leo directly above the Y Sex entry in the authors table.

Also, as can be seen in table 5.3, the periods of V2357 Oph and V1003 Her as determined by Deb and Singh (2011) and the ME programme are very different from the periods determined by ASAS. In the case of V2357 Oph the ASAS period is half the period determined by the ME Programme and in the case of V1003 Her the ASAS period is many times greater than the ME period. When the Python programme is run with the initial pre-set period search range around the ASAS period for these stars, the period-entropy output plot does not show a minimum value, but the slope of the curve shows in which direction to search for the correct period. After running the programme a few times it becomes clear that the true period lies far away. In this case a version of the programme is run which gives the user the option of choosing the period search range. However it has proved necessary to run the programme for longer than 24 hours to converge on these periods. In addition, in cases like this, the programme also converges on harmonics of the true periods. This is particularly true for periods exceeding 1 day.

In general the results of Deb and Singh (2011) and the Python ME programme are in agreement.

Table 5.3: Comparison of Deb and Singh (2011) results with ASAS and ME results. The column labelled N lists the number of ASAS data points used in the ME programme, while the columns labelled ASAS, D&S and ME respectively list the periods, in days, determined by ASAS, Deb and Singh (2011) and the ME programme.

ASAS ID	GCVS Name	N	ASAS	D&S	ME
003628+2132.3	DZ Psc	204	0.366125	0.366131	0.366135
011638–3942.5	AD Phe	488	0.379920	0.379919	0.379917
012104+0736.3	AQ Psc	312	0.475611	0.475604	0.475610
014656–0945.1	TT Cet	454	0.485960	0.485952	0.485952
014854–2053.6	TW Cet	747	0.316849	0.316851	0.316851
023833–1417.9	DY Cet	470	0.440790	0.440790	0.440789
024952+0856.3	EE Cet	302	0.379920	0.379925	0.379925
030701–5608.1	SZ Hor	606	0.625110	0.625102	0.625105
030953–0653.6	UX Eri	479	0.445280	0.445289	0.445289
033459+1742.6	V1123 Tau	352	0.399946	0.399947	0.399951
034814+2218.9	EQ Tau	286	0.341347	0.341350	0.341350
034928+1254.7	V1128 Tau	318	0.305372	0.305371	0.305372
035153–1031.8	BV Eri	486	0.507654	0.507655	0.507652
041209–1028.2	YY Eri	508	0.321499	0.321498	0.321499
042925–3334.6	CT Eri	968	0.634190	0.634196	0.634206
051114–0833.4	ER Ori	577	0.423400	0.423406	0.423408
051832–6813.6	RW Dor	923	0.285461	0.285463	0.285462
062605+2759.9	AH Aur	90	0.247053	0.494106	0.494131
064558–0017.5	DD Mon	430	0.568030	0.568019	0.568020
071058–0352.8	V753 Mon	629	0.677050	0.677045	0.677046
073246–2047.5	TY Pup	743	0.819250	0.819243	0.819249
073338–5007.4	HI Pup	593	0.432618	0.432618	0.432621
073905–0239.1	V868 Mon	502	0.637704	0.637704	0.637705
084002+1900.0	TX Cnc	489	0.382882	0.382883	0.382885
084108–3212.1	TZ Pyx	947	2.318500	2.318530	2.318547
100141+1724.5	XY Leo	348	0.284098	0.284101	0.284101
100234+1702.8	XZ Leo	347	0.487736	0.487736	0.487734

Table 5.3 cont.

ASAS ID	GCVS Name	N	ASAS	D&S	ME
100248+0105.7	Y Sex	370	0.419820	0.487736	0.419821
101602–0618.5	XX Sex	494	0.540111	0.540108	0.540113
104033+1334.0	UZ Leo	297	0.618060	0.618057	0.618056
105030–0241.7	VY Sex	737	0.443432	0.443433	0.443432
110211+0953.7	AM Leo	330	0.365798	0.365799	0.365801
110505+0509.1	AP Leo	336	0.430356	0.430358	0.430360
120103+1300.5	AG Vir	416	0.642650	0.642648	0.642647
121206+2232.0	CC Com	234	0.220686	0.220686	0.220685
123300+2642.9	RW Com	345	0.237348	0.237346	0.237347
131032–0409.5	PY Vir	393	0.311251	0.311248	0.311248
134607+0506.9	HT Vir	334	0.407672	0.407672	0.407674
141726+1234.1	VW Boo	398	0.342315	0.342315	0.342316
141937+0553.8	NN Vir	336	0.480687	0.480688	0.480690
143504+0906.8	CK Boo	345	0.355154	0.355152	0.355150
144803+1356.7	EL Boo	297	0.413767	0.413766	0.413759
152243+1615.7	OU Ser	318	0.148382	0.296768	0.296771
153152–1541.1	VZ Lib	496	0.358259	0.358256	0.358254
155649+2216.0	AU Ser	240	0.386498	0.386498	0.386496
164121+0030.4	V502 Oph	374	0.453390	0.453388	0.453390
165717+1059.8	V2357 Oph	422	0.207783	0.415568	0.415566
171358+1621.0	AK Her	302	0.421522	0.421524	0.421525
173356+0810.0	V2377 Oph	349	0.425403	0.425406	0.425422
175332–0354.9	V2610 Oph	550	0.426520	0.426514	0.426516
180921+0909.1	V839 Oph	368	0.409000	0.409008	0.409005
182913+0647.3	V2612 Oph	350	0.375300	0.375309	0.375305
185318+2113.5	V1003 Her	332	21.84685	0.493322	0.493326
193524+0550.3	V417 Aql	334	0.370306	0.370314	0.370313
194813+0918.5	OO/P Aql	347	0.506786	0.506794	0.506797
203113+0513.2	MR Del	393	0.521690	0.521692	0.521684
204628–7157.0	MW Pav	1034	0.795000	0.794994	0.794990
205710+1939.0	LS Del	247	0.363840	0.363842	0.363844
222257+1619.4	BB Peg	300	0.361487	0.361502	0.361503
233655+1548.1	V407 Peg	232	0.636880	0.636882	0.636886
234535+2528.3	V357 Peg	271	0.578450	0.578450	0.578461
234718–0805.2	EL Aqr	321	0.481410	0.481412	0.481411

5.4 Bright and Faint ASAS stars

The optimum magnitude range of ASAS is 8 to 13 magnitudes (Pojmanski, 2000), so what is the effect on the accuracy with which ASAS and the minimum entropy program can determine the periods of W UMa stars when the observed magnitudes are on the edge of these limits? In order to investigate the accuracy of the period determination at these limits a number of ASAS dim stars with magnitudes varying as high as 15.043 magnitude and a number of bright stars with magnitudes varying as low as 6.389 magnitudes were examined. This was done by comparing the periods determined by ASAS with the periods determined by the minimum entropy program. The results are listed in Tables 5.4 and 5.5.

Table 5.4: Bright W UMa stars for which periods have been determined.

ASAS ID	N	ASAS	ME	Magnitude range
012104+0736.3	305	0.475611	0.475604	8.49 – 8.88
035153–1031.8	483	0.507654	0.507652	8.10 – 8.65
035734–5421.5	581	0.490100	0.490100	8.15 – 8.93
041209–1028.2	507	0.321499	0.321499	8.15 – 8.99
052650–8135.2	1092	0.461660	0.461666	8.05 – 8.59
061618+0901.7	426	1.388060	1.388053	7.69 – 7.93
141937+0553.8	321	0.480687	0.480687	7.46 – 7.92
175653+0459.2	357	0.409652	0.409657	7.44 – 7.95
181550–3538.3	1264	1.087000	1.087020	7.29 – 7.76

Table 5.5: Faint W UMa stars for which ME periods have been determined.

ASAS ID	N	ASAS	ME	Magnitude range
000653+1646.4	176	0.277709	0.277707	12.99 – 14.06
001508–5335.4	401	0.239485	0.239500	13.06 – 14.27
023130–1252.4	378	0.258565	0.258563	13.35 – 14.63
023525–1518.7	189	2.870900	2.875400	13.81 – 14.79
032038–5902.4	500	0.354960	0.354955	13.18 – 14.09
033148–2631.7	435	0.300162	0.300165	13.28 – 14.49

Faint stars have relative noise levels greater than stars in the middle of the ASAS brightness range (Pojmanski, 2000). This makes it more difficult to clean up the data. The bright stars on the other hand tend to saturate the CCD's and they too reduce the number and reliability of the data.

As the tables for both the faint and bright stars show, the ASAS period and the minimum entropy period are either equal, or they differ by small amounts. Comparison of ASAS and ME period light curves (shown in appendix) of the bright stars TY Men (Figs. A.3 and A.4) and ASAS 175653+0459.2 (Figs. A.8 and A.9) and the faint stars ASAS 01508–5335.4 (Figs. A.16 and A.17) and ASAS 033148–2631.7 (Figs. A.22 and A.23) show clear improvements using the ME periods, although the light curves remain very noisy. In many cases it is hard to discern any improvement in the clarity of the light curves using the ME period. General comparisons of light curves generated with the ASAS and ME periods are shown in Fig. 5.12 to Fig. 5.15 and in the appendix.

5.5 High Period Change Rate Stars

Pilecki *et al.* (2007) listed 31 high period change rate stars (HPCR) observed by ASAS. These stars are contact and semi-detached eclipsing binaries which were observed by ASAS for 5 years. It is expected that as the data accumulated for these stars by ASAS increases with time, the reliability and accuracy of the period change measurements will improve.

19 of these stars (refer table 5.6) were selected for ME period analysis based on the fact that they are W UMa stars and also that they are listed in the SuperWASP data base. Pilecki *et al.* (2007) reports that the highest increasing period change rate for this group of 19 stars is $+0.38 \times 10^{-5}$ d yr^{-1} , (ASAS 060557-5342.9) and their highest decreasing period change rate is -0.77×10^{-5} d yr^{-1}, (ASAS 074537-3109.6). The highest increasing period change rates and the highest decreasing period change rates for the complete group of 31 stars was reported to be $+1.67 \times 10^{-5}$ d yr^{-1} , (ASAS 113333-6353.7) and -2.5×10^{-5} d yr^{-1}, (ASAS 114757-6034.0) respectively. These changes will result in a change in at least the sixth decimal digit of the light curve period every year. It turned out that very few of the 19 stars had actually been assigned periods by SuperWASP,

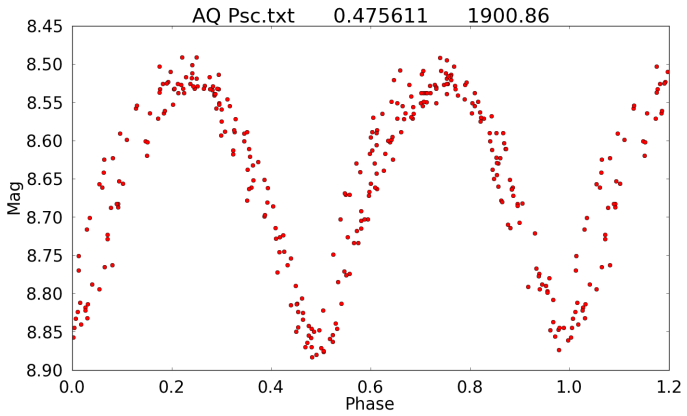

Figure 5.12: Light curve of bright star 012104+0736.3 folded on ASAS period 0.475611 d.

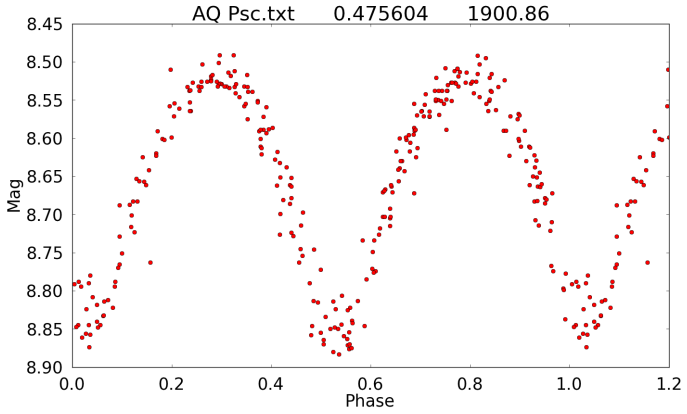

Figure 5.13: Light curve of bright star 012104+0736.3 folded on ME period 0.475604 d.

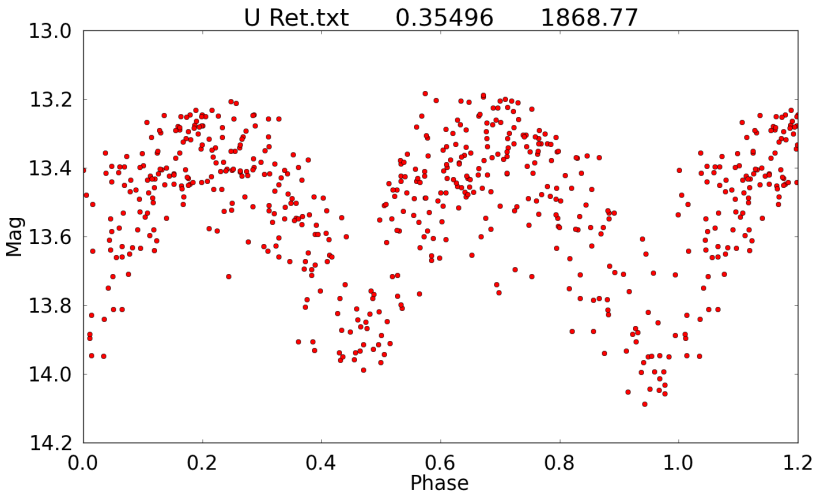

Figure 5.14: Light curve of faint star 032038–5902.4 folded on ASAS period 0.354960 d.

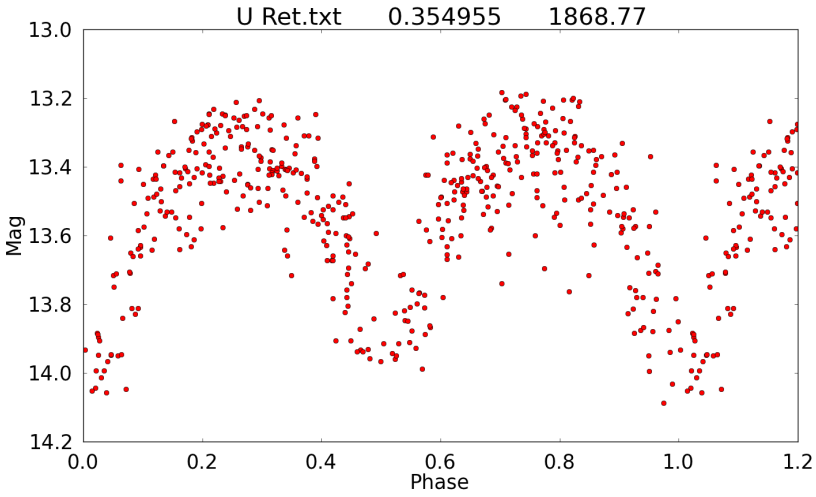

Figure 5.15: Light curve of faint star 032038–5902.4 folded on ME period 0.354955 d.

probably because they are HPCR stars. It is noteworthy that the Pilecki *et al.* (2007) periods are often closer in value to the ME periods than they are to the ASAS periods.

In spite of this last observation however, the ME program is only be capable of determining an average period for the data of the HPCR star being analysed. Hence, if the period of the star whose data is being analysed is changing, the ME period will reflect only the average period of the binary for the time over which the data was collected, and will not give the period for any one instant of time. Therefore if data collected over a few weeks, months or years, while the period is changing, is plotted using the average period determined by the ME programme for this data, it cannot be expected that the light curve will be sharp.

During the investigations for this dissertation the ASAS data for the HPCR stars was broken down into smaller sets. The data in these sets had to be kept in the correct time sequence. The results were indeterminate as no trend could be observed. It is believed that this indeterminacy is due to the fact that there is insufficient data in these data sets over the short periods of time when the periods of the binary can be regarded as constant. The ME program was simply producing averages for the data in the data packs which was being input for the given star and therefore the periods it was calculating for these sets was cycling around the average period with no specific trend.

Table 5.6: Pilecki *et al.* (2007), ASAS and ME periods for 19 Pilecki *et al.* (2007) HPCR stars. The column labelled N lists the number of ASAS data points used in the ME programme while the columns labelled ASAS, Pilecki *et al.* (2007) and ME respectively list the corresponding periods, in days, determined by Pilecki *et al.* (2007), ASAS and the ME programme.

ASAS ID	Other ID	N	Pilecki *et al.* (2007)	ASAS	ME
002449–2744.3	-	515	0.313661	0.313670	0.313661
002821–2904.1	-	526	0.269892	0.269896	0.269892
004717–1941.6	CPD 20 88	751	0.488810	0.488810	0.488810
014933–1937.6	VY Cet	708	0.340809	0.340812	0.340812
052851–3010.2	-	589	0.302101	0.302101	0.302097
060557–5342.9	GSC 08521–01468	731	0.463634	0.463630	0.463639
062254–7502.0	-	1015	0.257707	0.257704	0.257706
062426–2044.9	GSC 05959–01748	738	0.384692	0.384698	0.384692
065232–2533.5	HD 50494	589	0.418639	0.418634	0.418637
070959–3639.5	HD 55100	772	0.371829	0.371832	0.371832
071727–4007.7	GZ Pup	619	0.320265	0.320267	0.320264
072729–5056.5	-	594	0.330557	0.330552	0.330559
074537–3109.6	GSC 07106–00494	582	0.602926	0.602930	0.602919
082456–4833.6	-	587	0.364875	0.364879	0.364873
093312–8028.5	GSC 09404–00233	1172	0.406067	0.406071	0.406065
095048–6723.3	NSV 4657	818	0.276943	0.276944	0.276943
114757–6034.0	SV Cen	685	1.657589	1.657640	1.657536
135243–5532.5	V758 Cen	866	0.580784	0.580790	0.580788
144047–3725.3	HD 128910	632	0.353410	0.353414	0.353410

Chapter 6

Conclusions

6.1 General

A number of different versions of the Python ME programme were written for this dissertation. The version found to be most useful for the study of ASAS W UMa stars in general is the version with a pre-set period search range around the ASAS period. This is because the ASAS periods of the stars which were studied were generally found to be accurate to at least the 5^{th} decimal point. With a pre-set period search around the 5^{th} and 6^{th} decimal point, it was necessary only to provide the program with an ASAS data file with noise removed, the ASAS period and epoch of minimum brightness and the program allowed to run. When the program reaches the end of the search range it outputs the minimum value of entropy and the corresponding period calculated for this search range, as well as the period–entropy plot and the light curve plotted on the determined period.

There were occasions, however. when the periods assigned by ASAS were far from the true period. When this occurred, the period–entropy plot did not show a minimum, but the slope of the curve indicated whether the true period was greater or less than the period output by the programme. By this means it is possible to select a new period around which the programme searched. However, this required multiple runs of the programme which could take a long time.

In a few case the ASAS period was so far away from the true period that the above procedure was impractical and a second version of the programme was used. This version allowed the user to select the range of periods around the ASAS period which the programme searched. Although this version does not require to be run as many times as the standard version discussed above, it could take well over 24 hours to complete a run. On completion of this long run, the output was sometimes an harmonic of the true period. When this occurred, although the light curve was sharp, it was not continuous and looked as if some sections had been cut out of the complete light curve and joined together.

The accuracy of the ME programme is also a function of the number of data points in the ASAS data file and the distribution of this photometric data over the light curve. When the photometric data are well distributed over all the phases of the light curve, accurate period determination can be obtained, even for low numbers of data points. However, large numbers of data points are required in order to ensure adequate distribution over the light curve and this requires longer programme running times.

Under circumstances when the ASAS period is relatively accurate the ME programme works well. But when the ASAS period is far removed from the true period and there are a large number of data points the programme may take too long to be practical for application to large groups of binaries.

6.2 Tests on Sinusoidal light Curves

The ME programme was tested on perfect sinusoids with data points spread uniformly over all phases of the sinusoid and with numbers of data points corresponding to numbers typical of the numbers of data points found in the selected ASAS files. These tests showed that the entropy does not decrease smoothly or monotonically as the trial period approaches the true period of the sine wave. Based on these tests and tests carried out using the data set of MW Pav (ASAS 204628-7157.0) which had a period similar to the 0.732566 d sinusoid and a number of photometric data point similar to the number of data points used for this sinusoid it was established that the ME programme would calculate a period of acceptable accuracy in about 20 minutes if it was pre-set to divide the period-magnitude plane into a 50 x 50 matrix.

6.3 Comparison with Deb and Singh (2011)

The periods determined by the ME programme showed general agreement with the periods determine by Deb and Singh (2011).

6.4 Light Curves of Faint and Light systems

Faint stars are very noisy because system and atmospheric noise makes up a larger proportion of the data signals. Bright stars cause pixel saturation and again contribute to noise and distortion of the data signals. The ASAS and ME periods of the selected stars are close. The ME programme improved on the ASAS periods for 3 of the 6 dim stars and for 3 of the 9 bright stars but light curves remained noisy.

6.5 Light Curves of the HPCR stars

The apparent rate of period change in the 19 stars selected from the Pilecki *et al.* (2007) report amounts to a change in at least the 6^{th} decimal digit of the ASAS/ME period every year. In most cases the ME period was closer to the Pilecki *et al.* (2007) period than the ASAS period and the light curves showed improvements but were still noisy. In the case of ASAS 004430—3606.5 (CR Scl) which has a fairly large number of data points in its ASAS data file and which has a brightness in the middle of the ASAS system specification range, it was expected that the light curve would be sharp. When this did not prove to be the case, as the light curve resembled those of the 19 HPCR stars, investigations revealed that American Association of Variable Star Observers (AAVSO) had determined that this star is an HPCR star as it has a period change rate of 0.26×10^{-5} dyr^{-1}.

The ASAS data sets of these HPCR stars were broken into smaller temporal sets in order to determine if the binary periods were changing with time. However no temporal trend in the periods could be discerned and the periods calculated revolved around the period determined for the full set of data with no apparent trend. It was realised that there was insufficient well distributed data in the ASAS data sets to get results of any value.

Appendix A

Additional Material

A.1 Light Curves of Bright Stars

In this section folded light curves of the bright ASAS stars listed in Table 5.4 are presented, folded on both ASAS and ME periods for comparison. ASAS 012104+0736.3 is shown in Fig. 5.12 and 5.13 and is not repeated here.

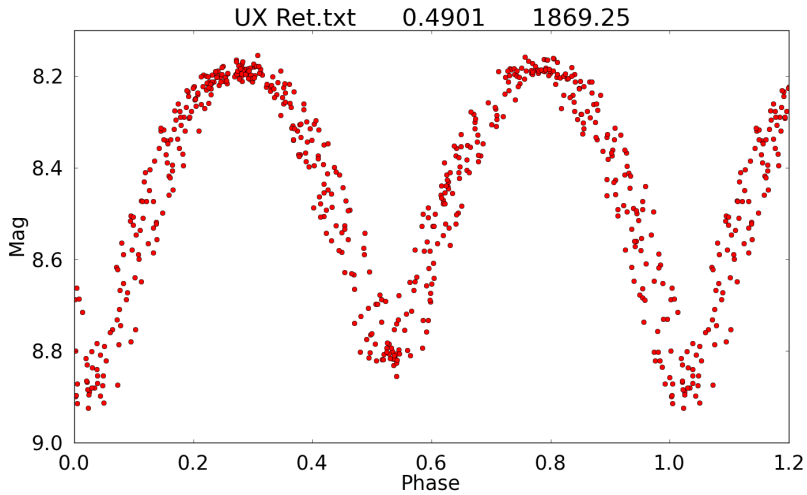

Figure A.1: Light curve of ASAS 035734–5421.5 folded on a period common to both ASAS and ME.

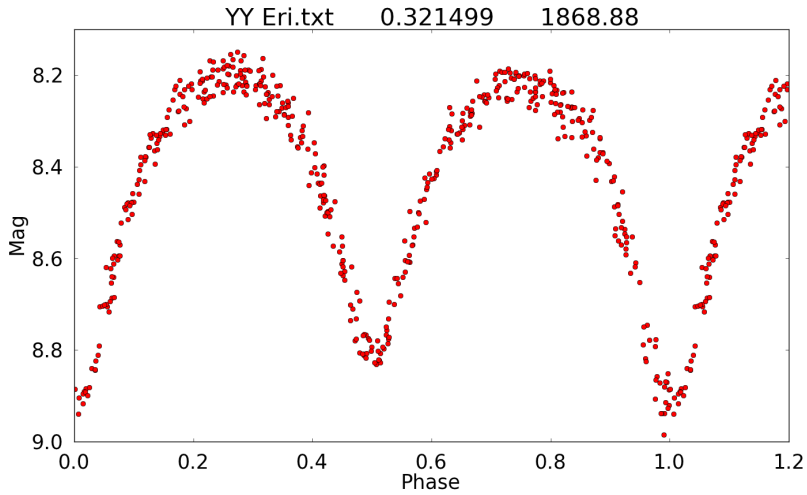

Figure A.2: Light curve of ASAS 041209–1028.2 folded on a period common to both ASAS and ME.

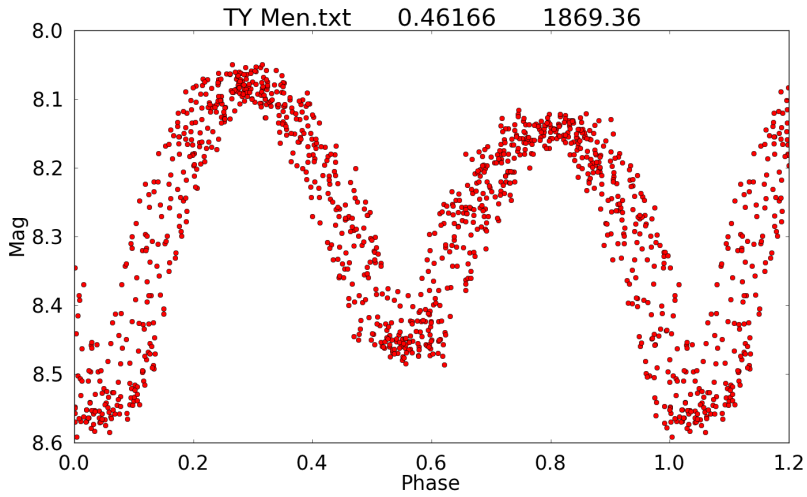

Figure A.3: Light curve of ASAS 52650–8135.2 folded on the ASAS period.

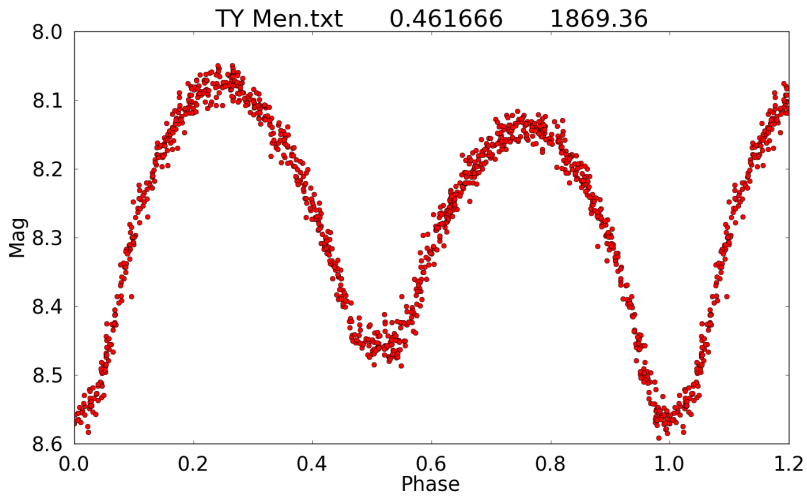

Figure A.4: Light curve of ASAS 52650–8135.2 folded on the ME period.

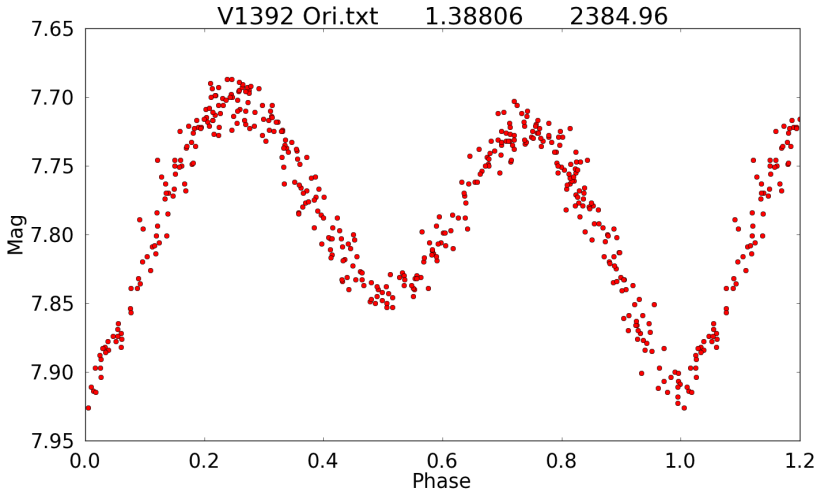

Figure A.5: Light curve of ASAS 061618+0901.7 folded on the ASAS period.

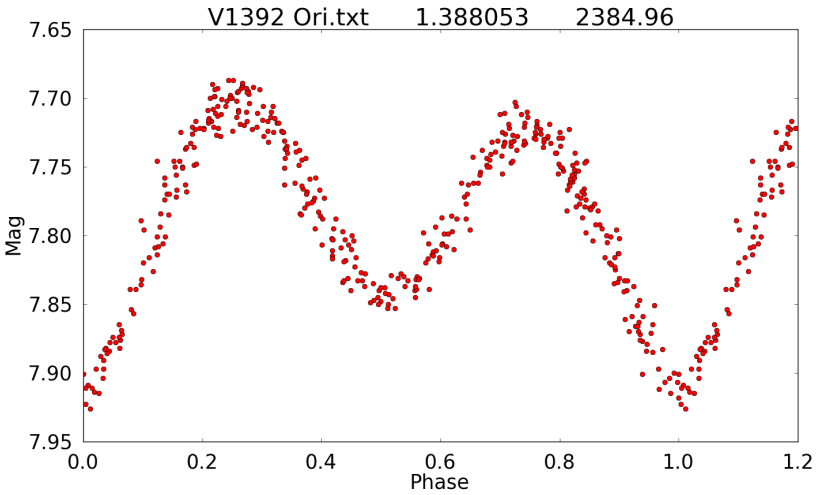

Figure A.6: Light curve of ASAS 061618+0901.7 folded on the ME period.

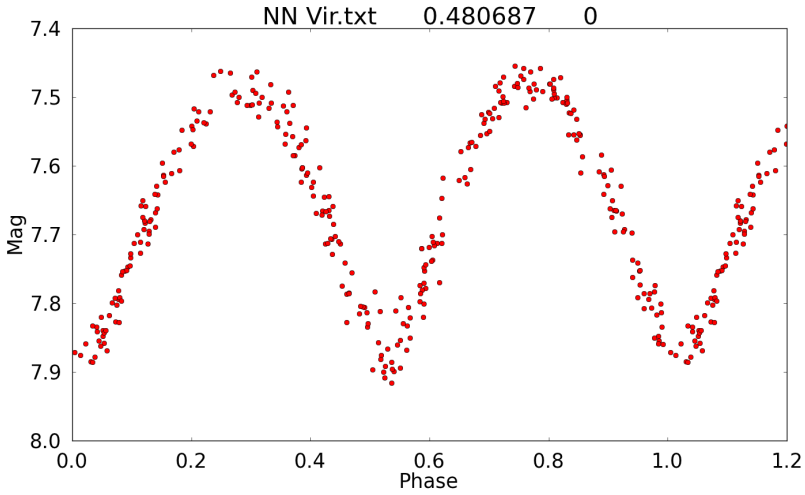

Figure A.7: Light curve of ASAS 141937+0553.8 folded on a period common to both ASAS and ME.

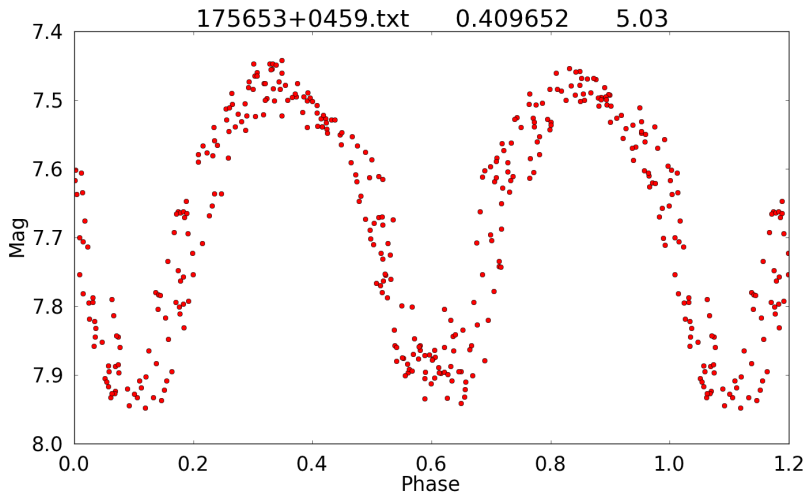

Figure A.8: Light curve of ASAS 175653+0459.2 folded on the ASAS period.

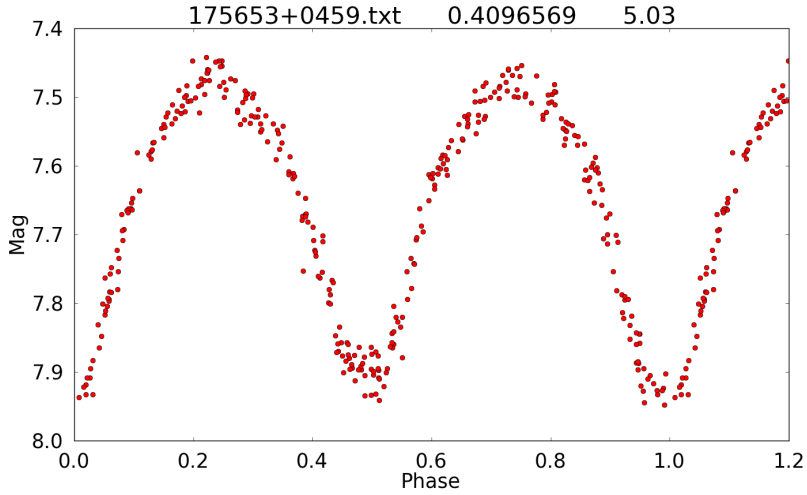

Figure A.9: Light curve of ASAS 175653+0459.2 folded on the ME period.

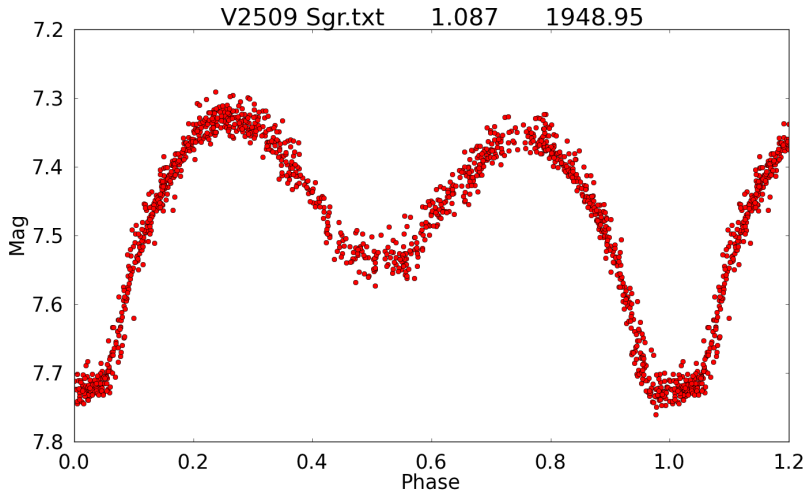

Figure A.10: Light curve of ASAS 181550–3538.3 folded on the ASAS period.

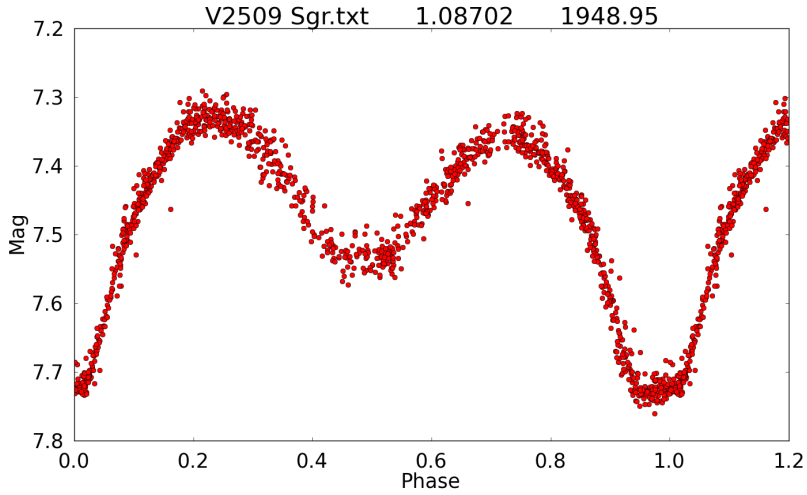

Figure A.11: Light curve of ASAS 181550–3538.3 folded on the ME period.

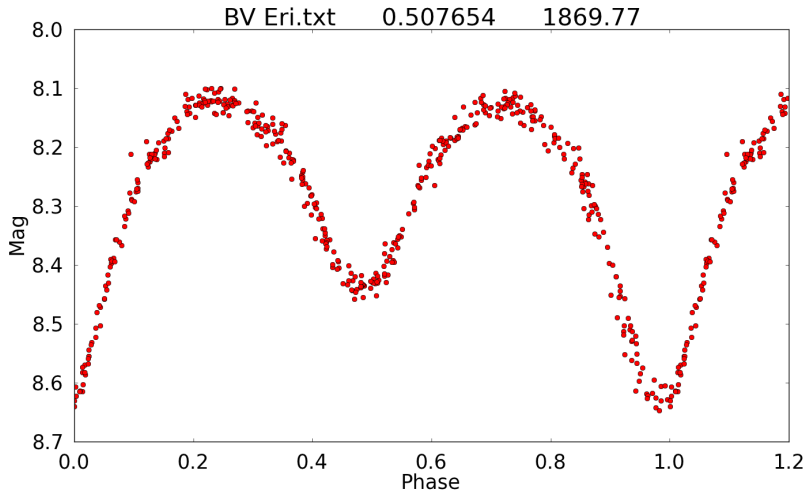

Figure A.12: Light curve of ASAS 035153–1031.8 folded on the ASAS period.

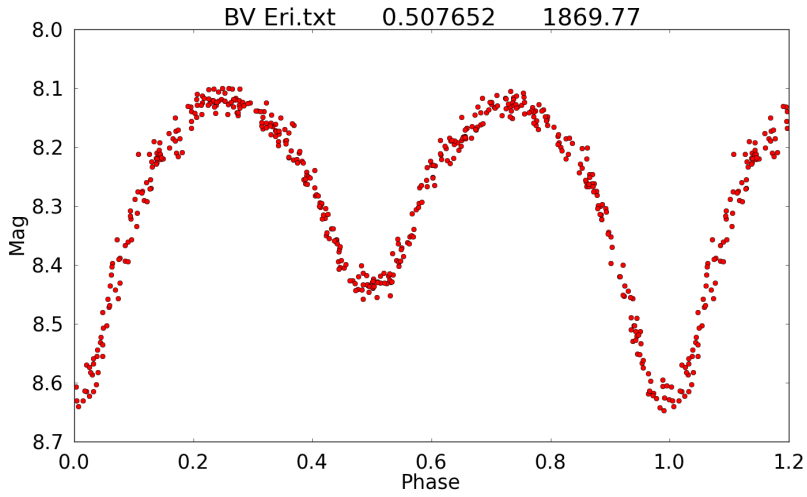

Figure A.13: Light curve of ASAS 035153–1031.8 folded on the ME period.

A.2 Light Curves of Faint Stars

In this section folded light curves of the faint ASAS stars listed in Table 5.5 are presented, folded on both ASA and ME periods for comparison. ASAS 032038–5902.4 is shown in

Figs. 5.14 and 5.15 and is not repeated here.

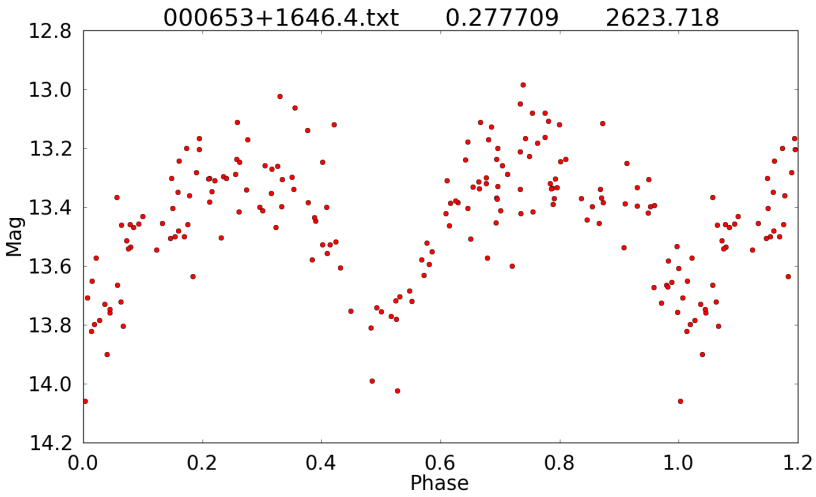

Figure A.14: Light curve of ASAS 000653+1646.4 folded on the ASAS period.

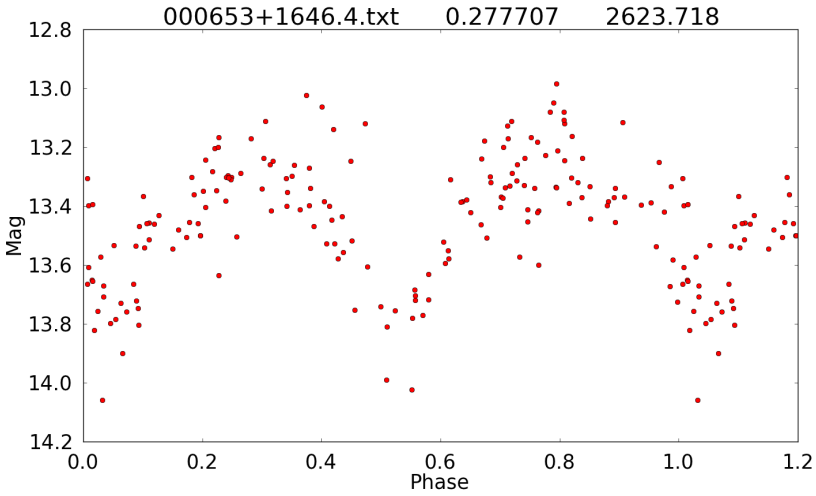

Figure A.15: Light curve of ASAS 000653+1646.4 folded on the ME period.

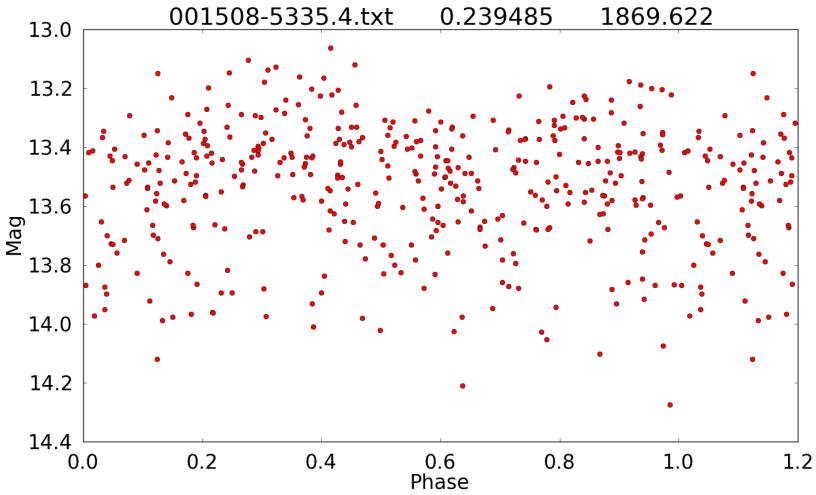

Figure A.16: Light curve of ASAS 01508–5335.4 folded on the ASAS period.

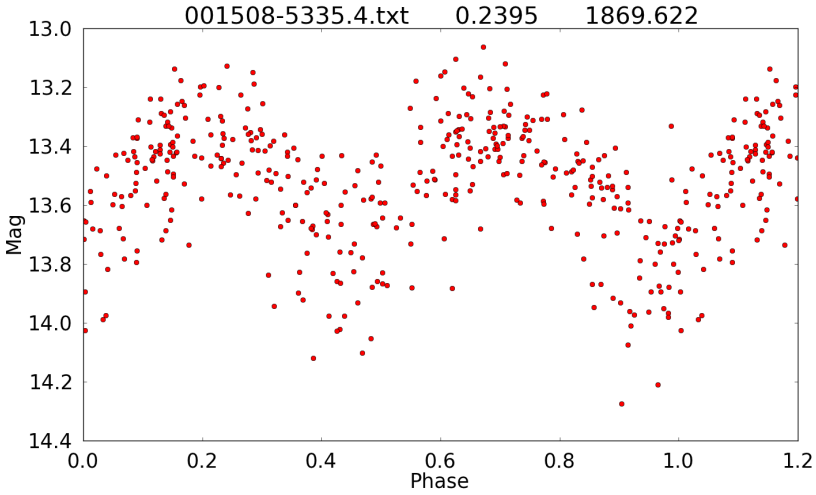

Figure A.17: Light curve of ASAS 01508–5335.4 folded on the ME period.

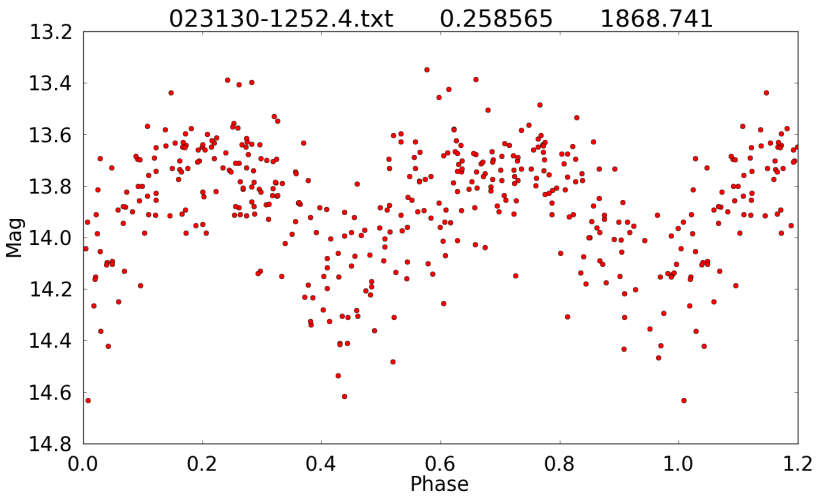

Figure A.18: Light curve of ASAS 023130–1252.4 folded on the ASAS period.

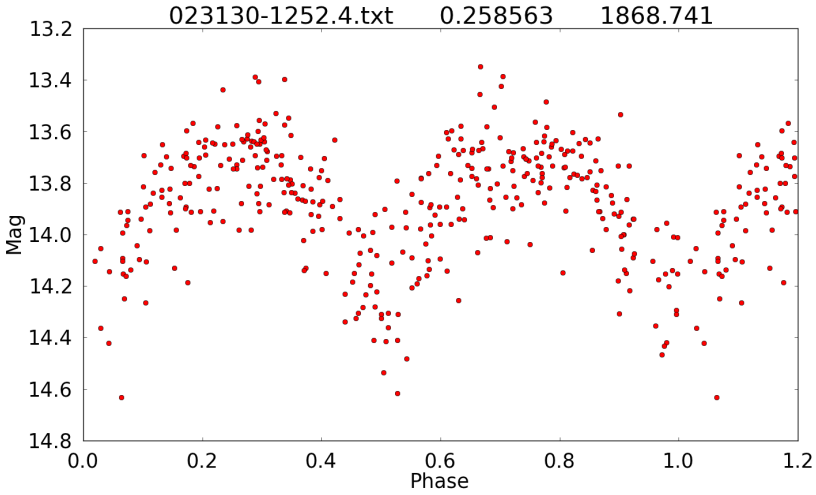

Figure A.19: Light curve of ASAS 023130–1252.4 folded on the ME period.

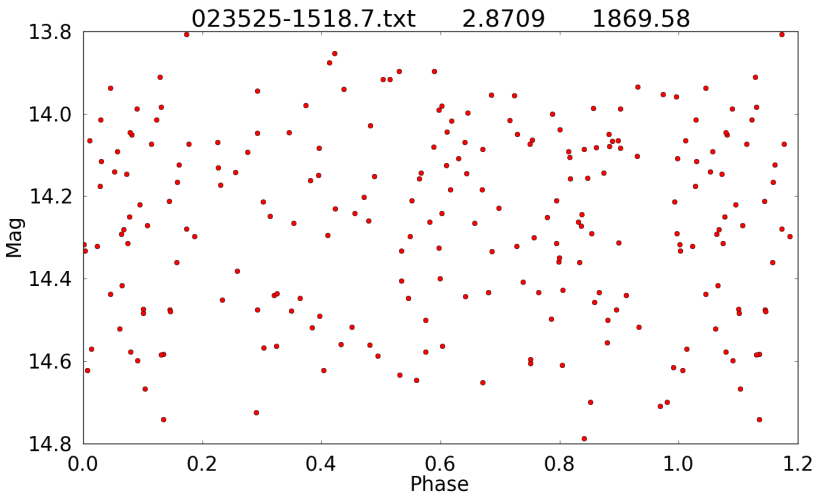

Figure A.20: Light curve of ASAS 023525–1518.7 folded on the ASAS period.

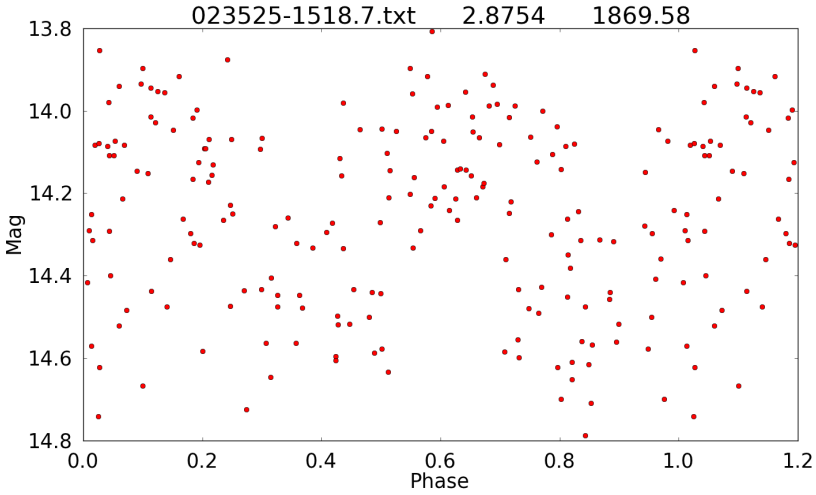

Figure A.21: Light curve of ASAS 023525–1518.7 folded on the ME period.

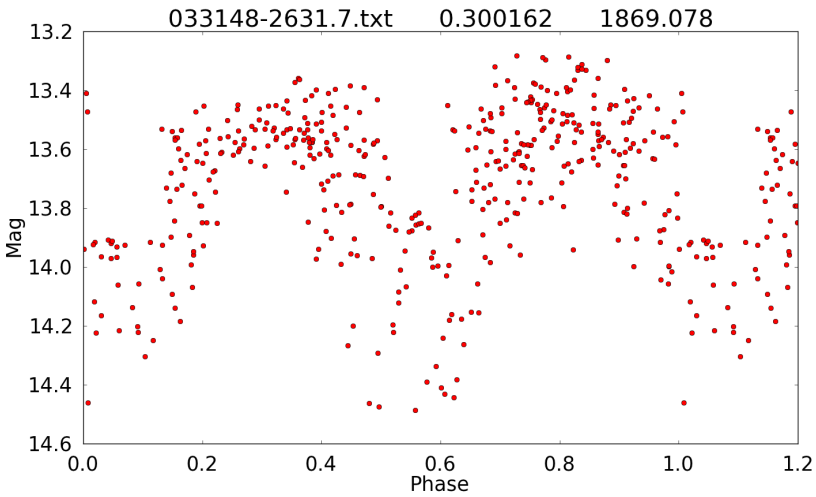

Figure A.22: Light curve of ASAS 033148–2631.7 folded on the ASAS period.

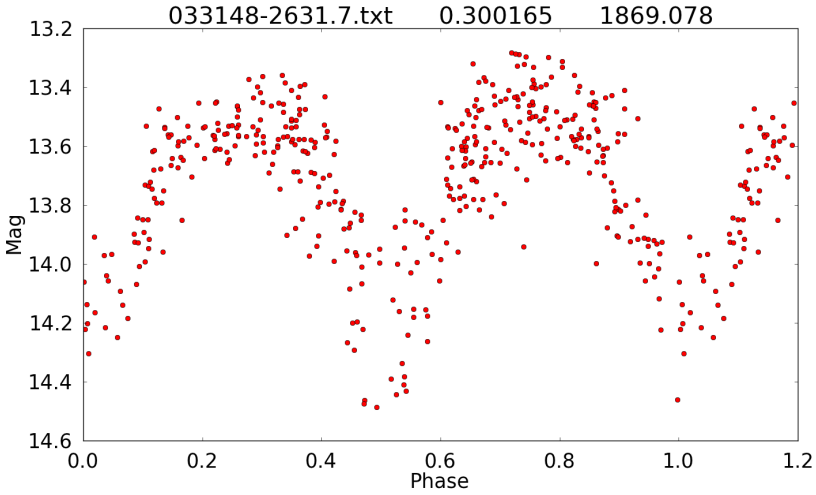

Figure A.23: Light curve of ASAS 033148–2631.7 folded on the ME period.

A.3 Light and Period–Entropy Plots of High Period Change Rate Stars

Because of the fact that these stars are all HPCR stars they were binned on 100 magnitude elements x 100 phase elements, in an effort to improve accuracy resolution, when the ME program was run. The light curve folded on its ASAS period is presented here too and it can be seen that the ME period often makes a substantial improvement on the ASAS period, but hardly ever results in a sharply defined light curve (except for SV Cen Fig. A.71). In this section the period–entropy curve is also plotted, this is in order to show that that the period on which the ME programme converges sometimes seems to dither rather than converge on a sharply defined period. Perhaps this is because of the rapidly varying period of these stars.

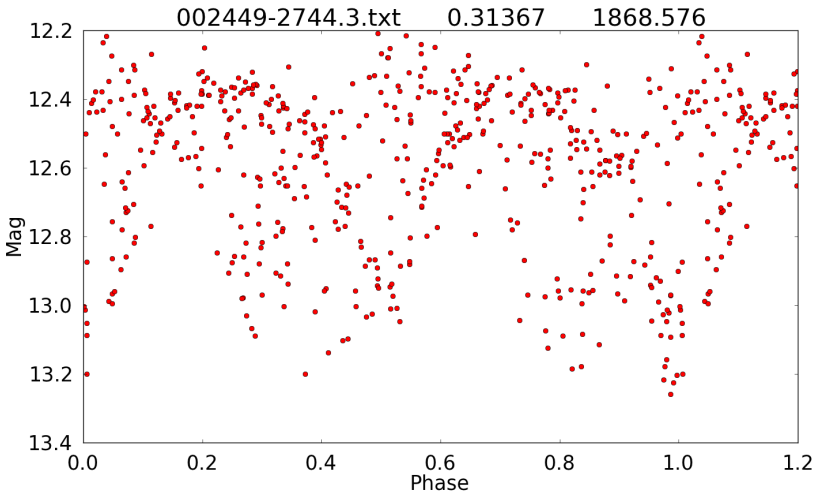

Figure A.24: Light curve of ASAS 002449–2744.3 HPCR star folded on the ASAS period.

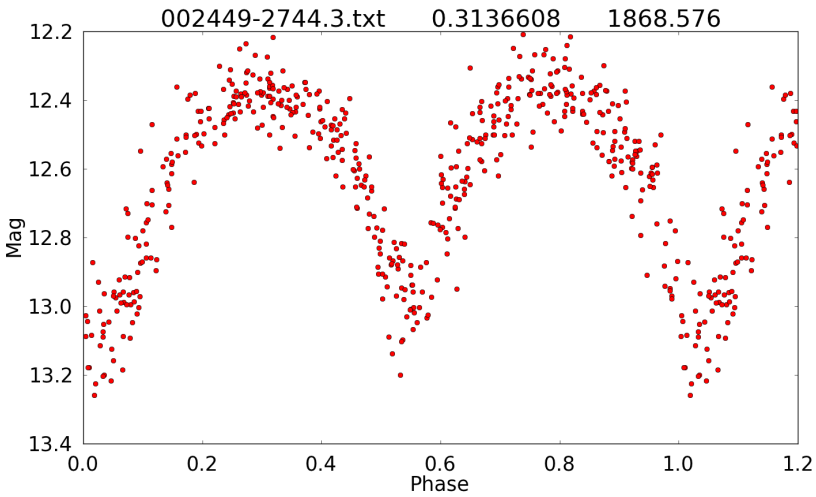

Figure A.25: Light curve of ASAS 002449–2744.3 HPCR star folded on the ME period.

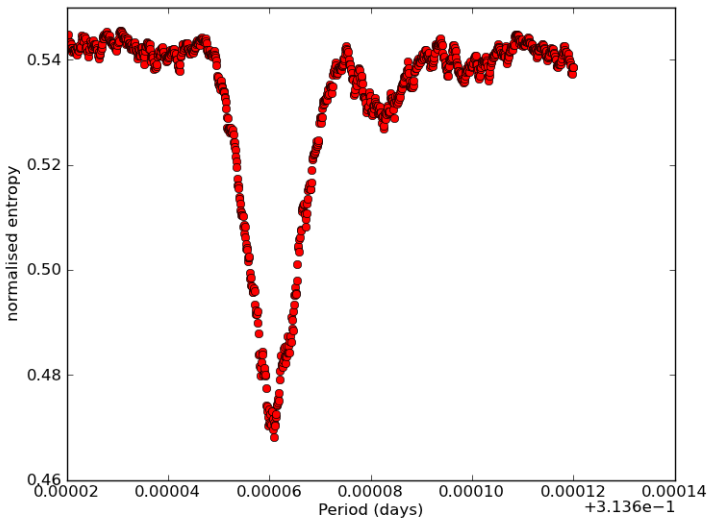

Figure A.26: Period–entropy curve of ASAS 002449–2744.3 HPCR star.

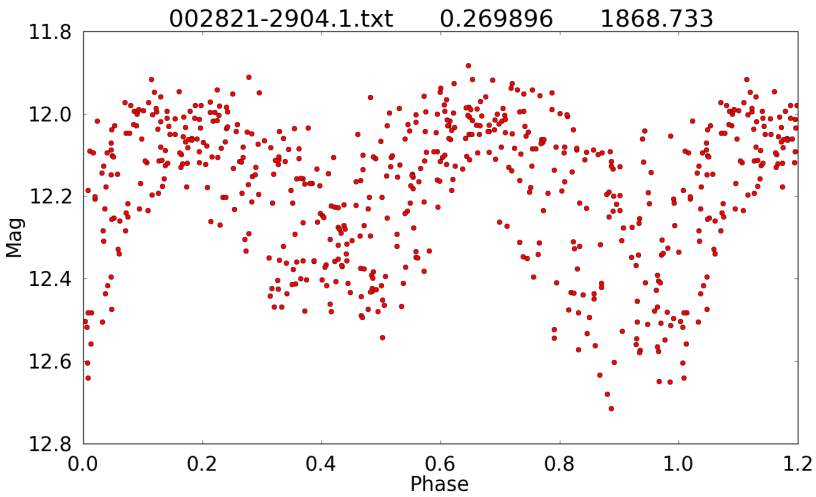

Figure A.27: Light curve of ASAS 002821–2904.1 HPCR star folded on the ASAS period.

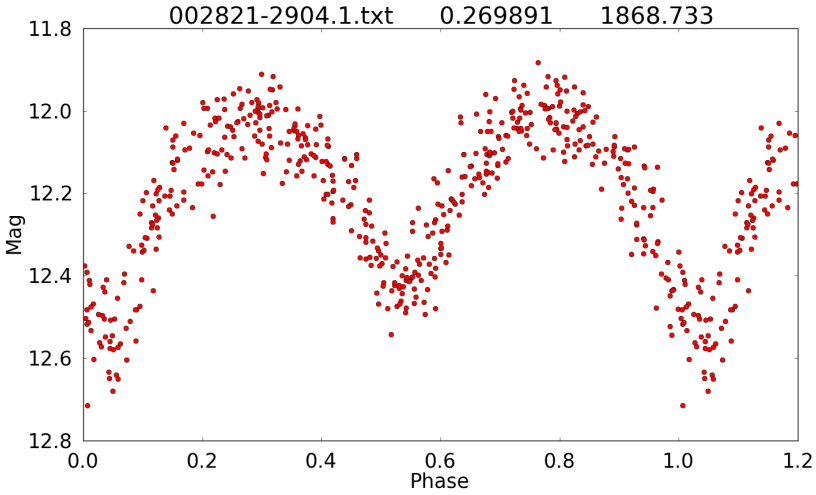

Figure A.28: Light curve of ASAS 002821–2904.1 HPCR star folded on the ME period.

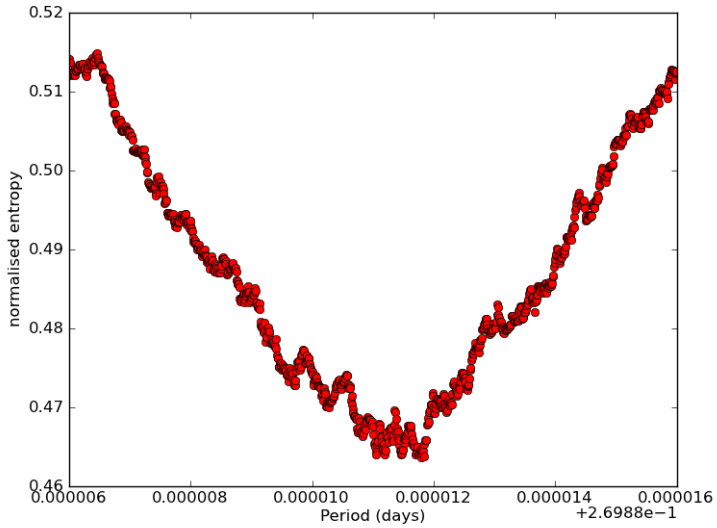

Figure A.29: Period–Entropy curve of ASAS 002821–2904.1 HPCR star.

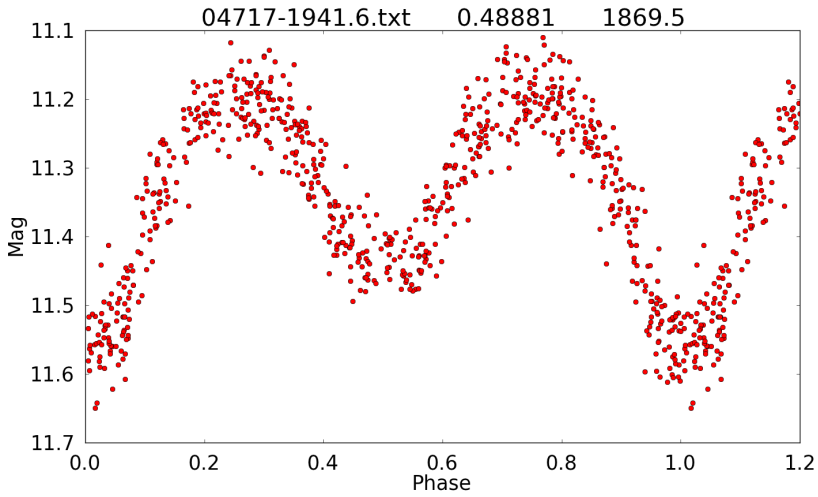

Figure A.30: Light curve of ASAS 004717–1941.6 (Cape Photographic Durchmustering (CPD) 20 88) HPCR star folded on a period common to both ASAS and ME.

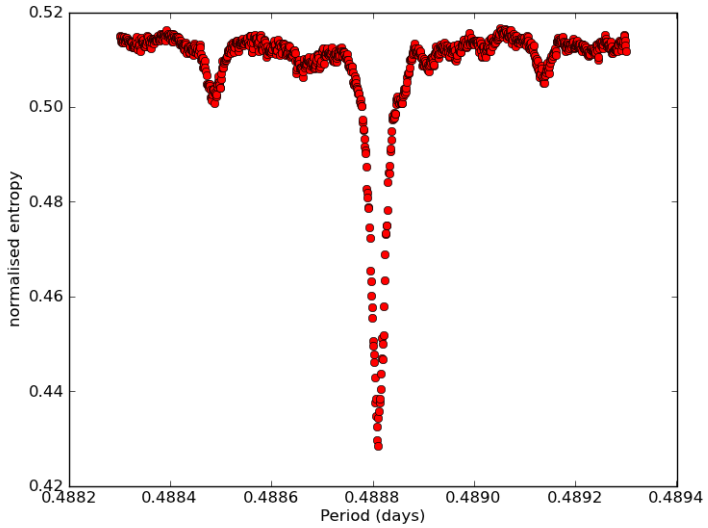

Figure A.31: Period–Entropy curve of ASAS 004717–1941.6 (CPD 20 88) HPCR star.

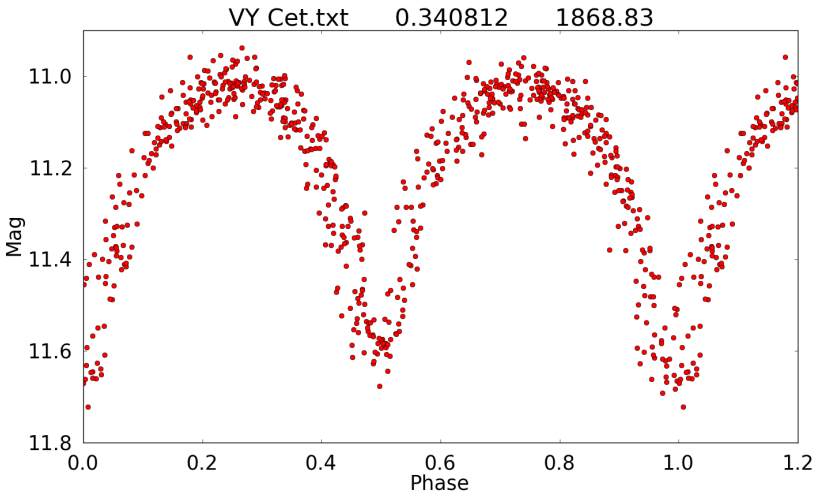

Figure A.32: Light curve of ASAS 014933–1937.6 (VY Cet) HPCR star folded on a period common to both ASAS and ME.

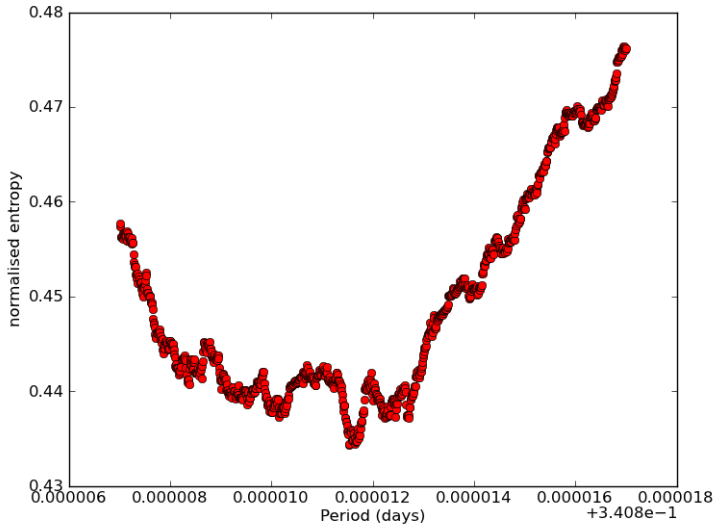

Figure A.33: Period–Entropy curve of ASAS 014933–1937.6 (VY Cet) HPCR star.

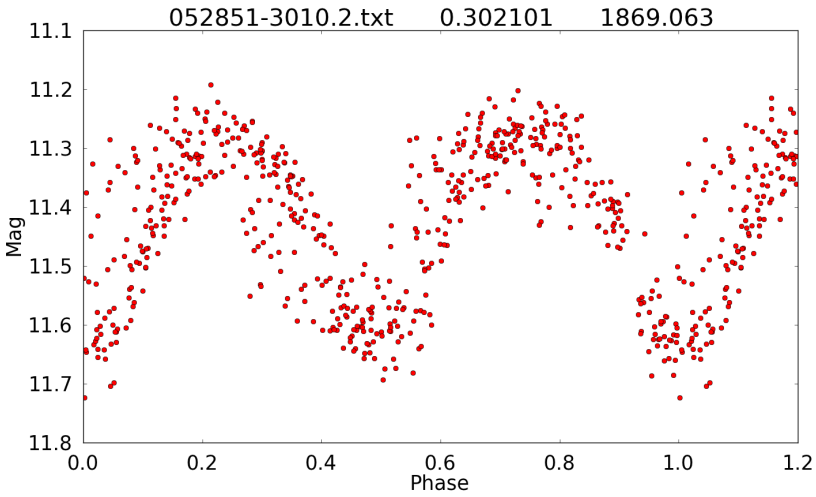

Figure A.34: Light curve of ASAS 052851–3010.2 HPCR star folded on the ASAS period.

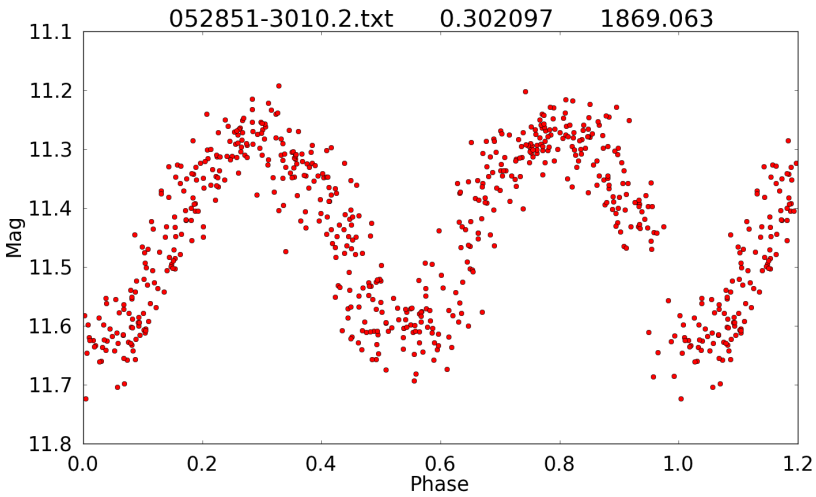

Figure A.35: Light curve of ASAS 052851–3010.2 HPCR star folded on the ME period.

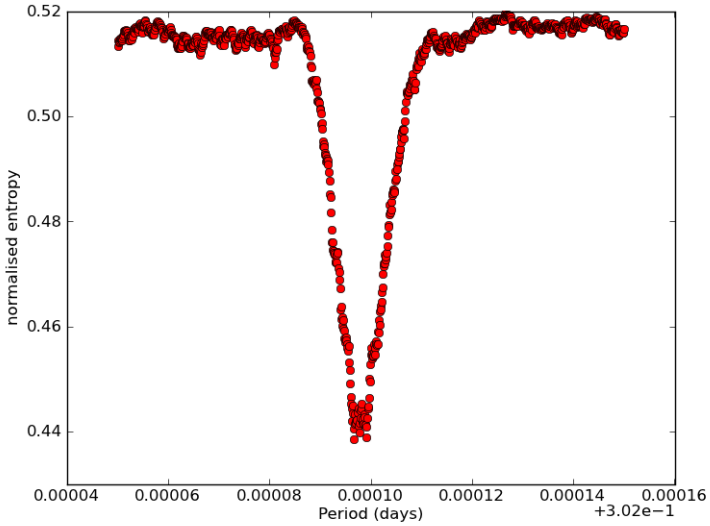

Figure A.36: Period–Entropy curve of ASAS 052851–3010.2 HPCR star.

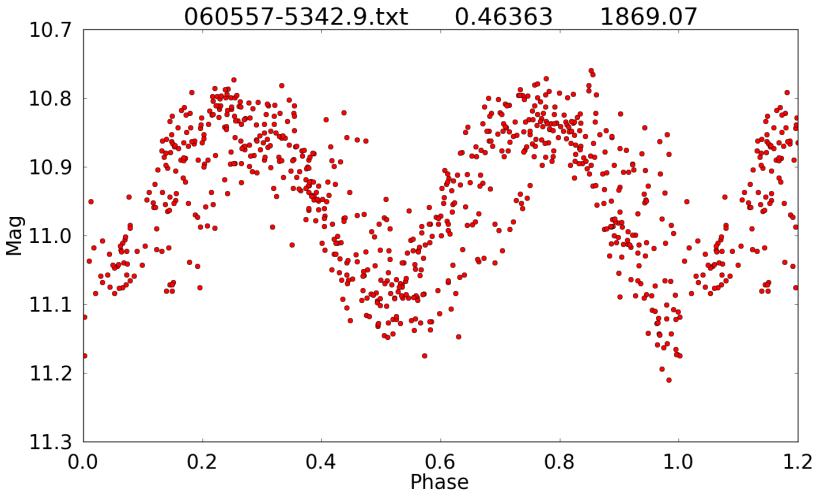

Figure A.37: Light curve of ASAS 060557–5342.9 (GSC 08521–01468) HPCR star folded on the ASAS period.

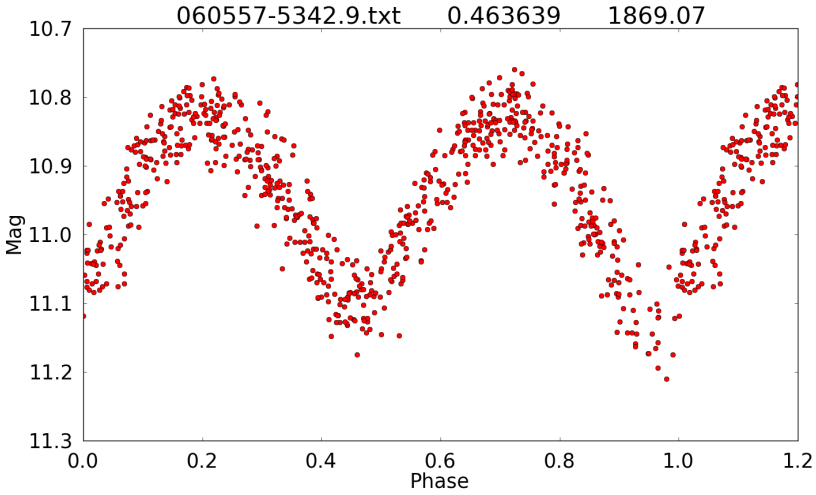

Figure A.38: Light curve of ASAS 060557–5342.9 (GSC 08521–01468) HPCR star folded on the ME period.

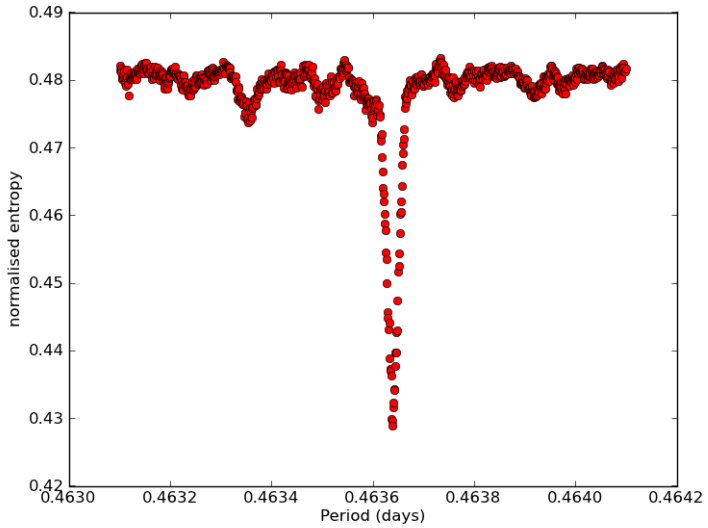

Figure A.39: Period–Entropy curve of ASAS 060557–5342.9 (GSC 08521–01468) HPCR star.

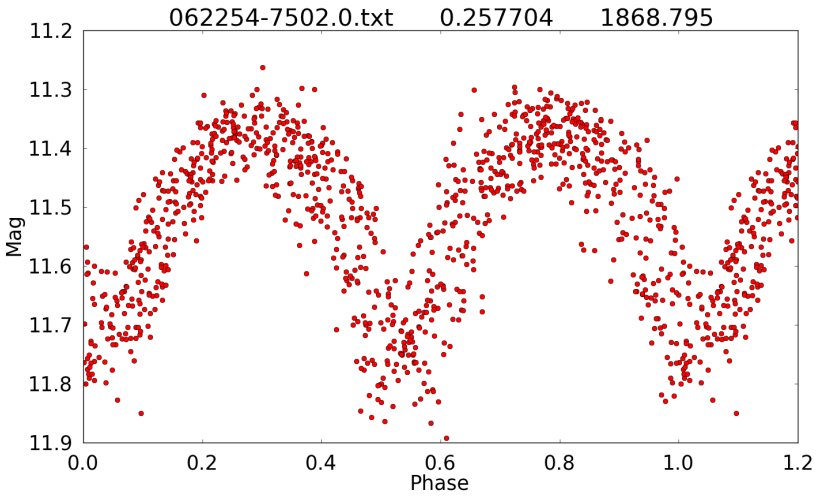

Figure A.40: Light curve of ASAS 062254–7502.0 HPCR star folded on the ASAS period.

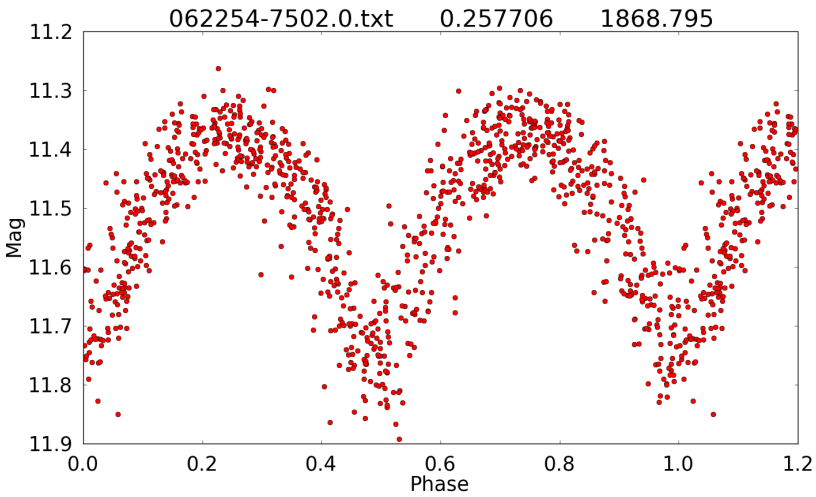

Figure A.41: Light curve of ASAS 062254–7502.0 HPCR star folded on the ME period.

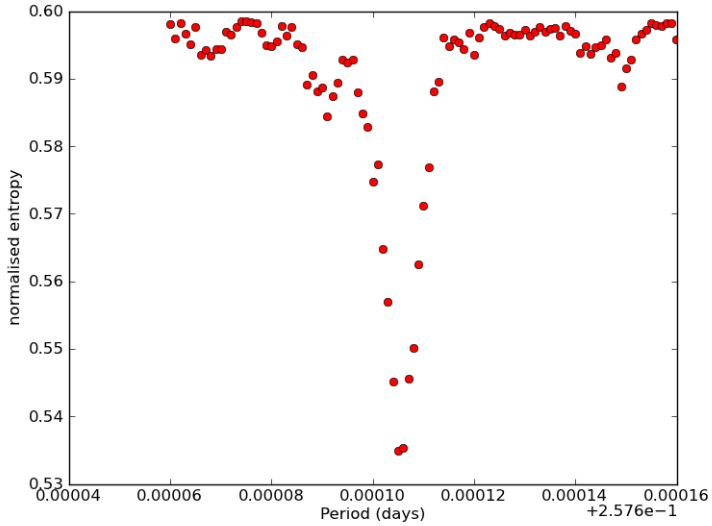

Figure A.42: Period–Entropy curve of ASAS 062254–7502.0 HPCR star.

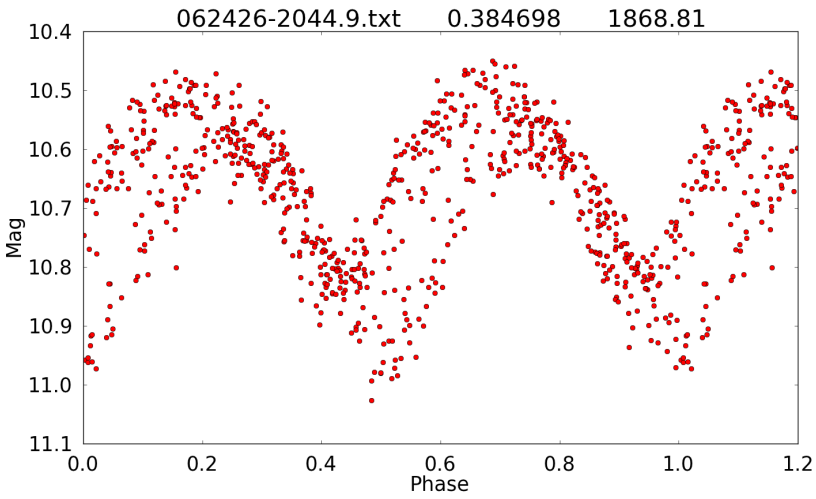

Figure A.43: Light curve of ASAS 062426–2044.9 (GSC 05959–01748) HPCR star folded on the ASAS period.

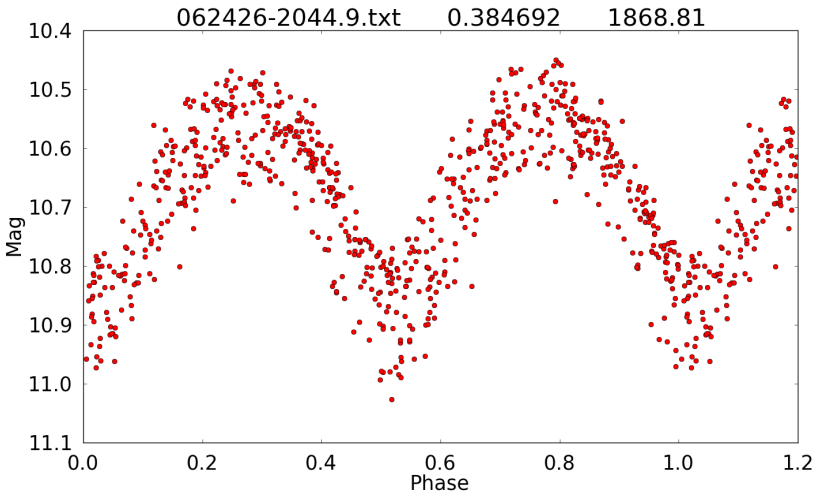

Figure A.44: Light curve of ASAS 062426–2044.9 (GSC 05959–01748) HPCR star folded on the ME period.

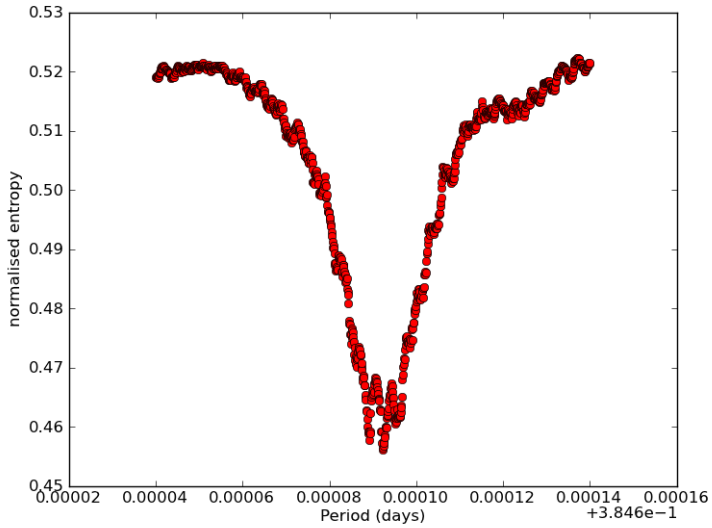

Figure A.45: Period–Entropy curve of ASAS 062426–2044.9 (GSC 05959–01748) HPCR star.

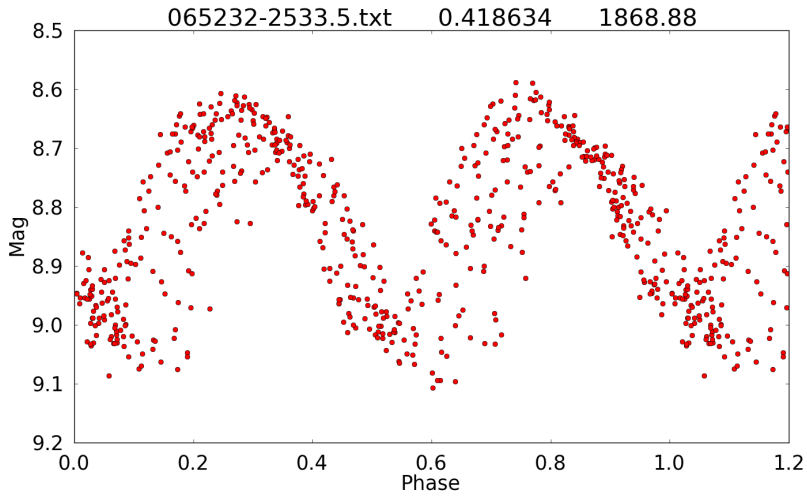

Figure A.46: Light curve of ASAS 065232–2533.5 (HD 50494) HPCR star folded on the ASAS period.

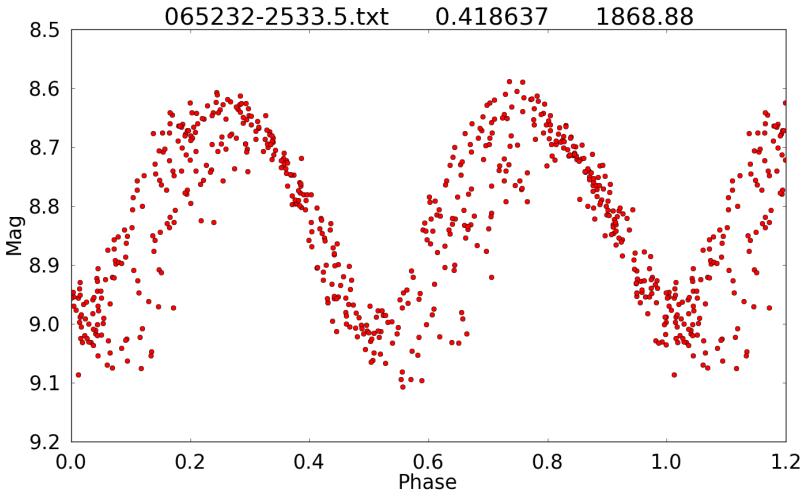

Figure A.47: Light curve of ASAS 065232–2533.5 (HD 50494) HPCR star folded on the ME period.

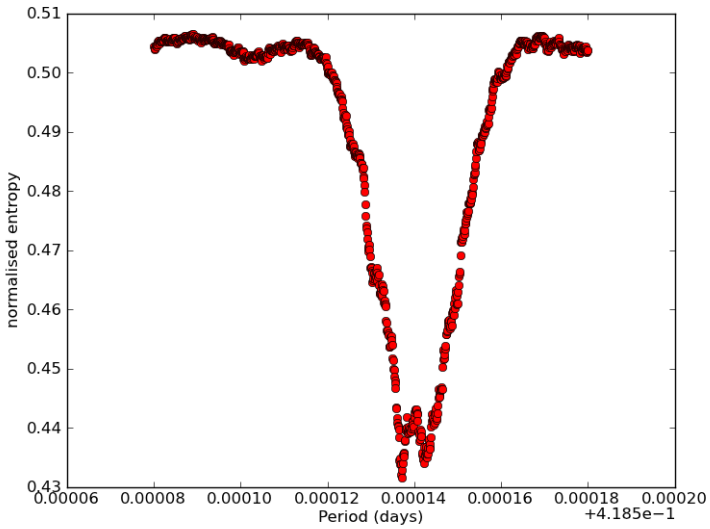

Figure A.48: Period–Entropy curve of ASAS 065232–2533.5 (HD 50494) HPCR star.

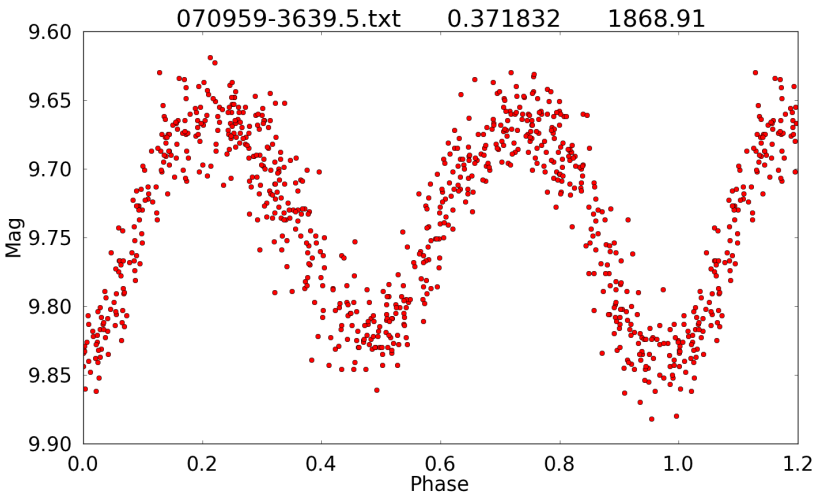

Figure A.49: Light curve of ASAS 070959–3639.5 (HD 55100) HPCR star folded on the ASAS period.

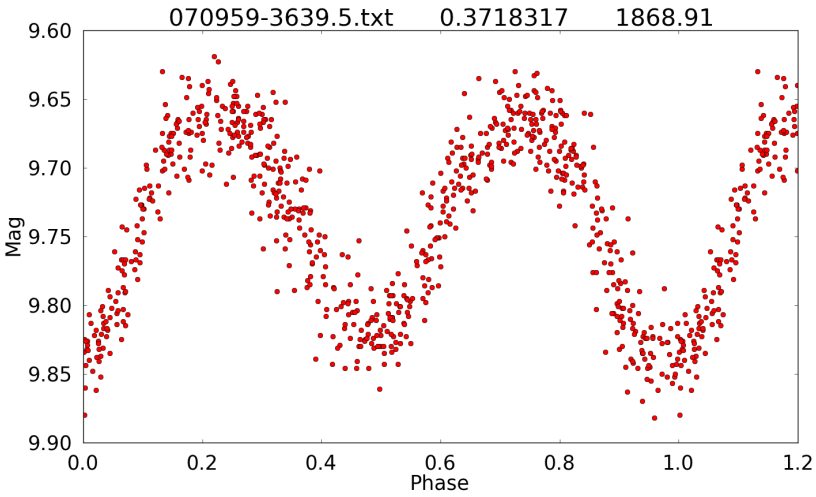

Figure A.50: Light curve of ASAS 070959–3639.5 (HD 55100) HPCR star folded on the ME period.

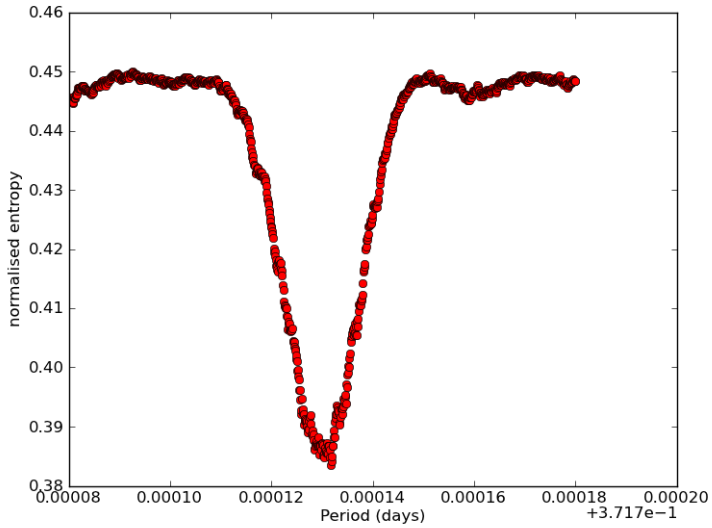

Figure A.51: Period–Entropy curve of ASAS 070959–3639.5 (HD 55100) HPCR star.

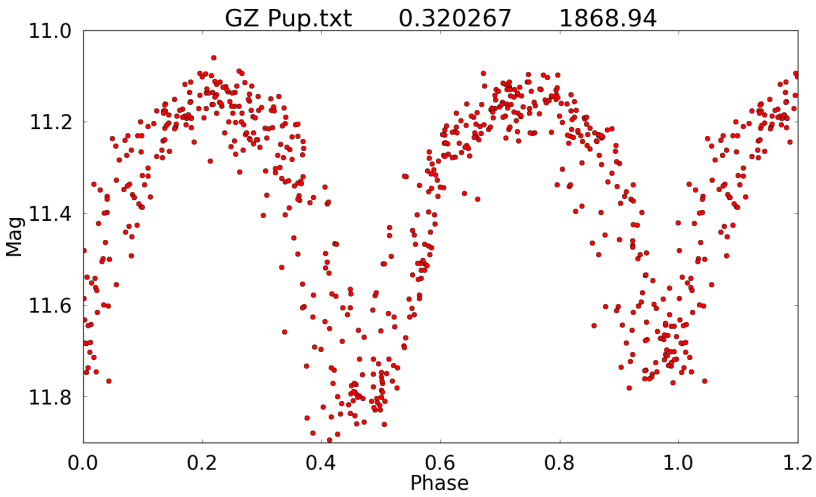

Figure A.52: Light curve of ASAS 071727–4007.7 (GZ Pup) HPCR star folded on the ASAS period.

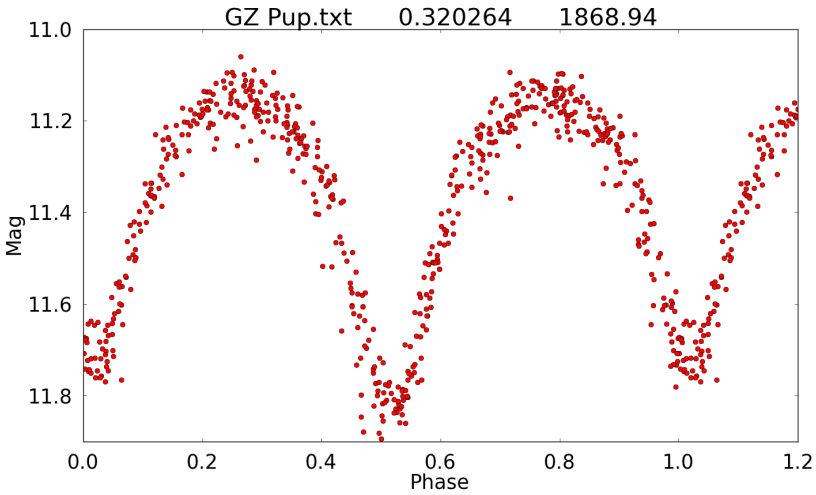

Figure A.53: Light curve of ASAS 071727–4007.7 (GZ Pup) HPCR star folded on the ME period.

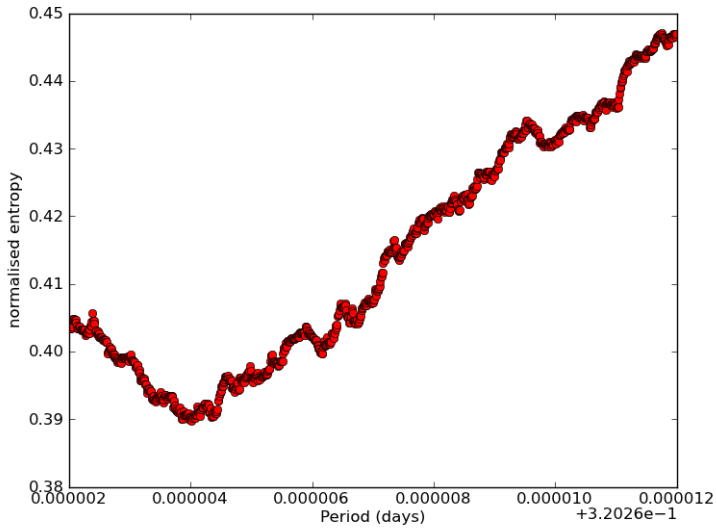

Figure A.54: Period–Entropy curve of ASAS 071727–4007.7 (GZ Pup) HPCR star.

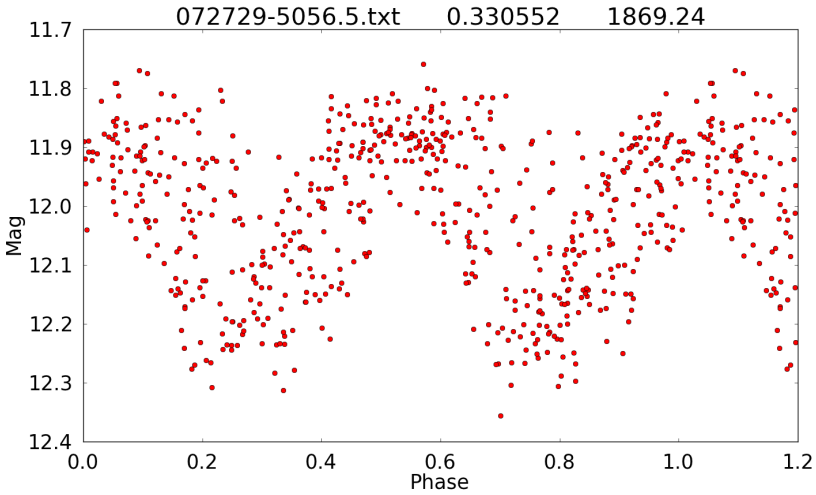

Figure A.55: Light curve of ASAS 072729–5056.5 HPCR star folded on the ASAS period.

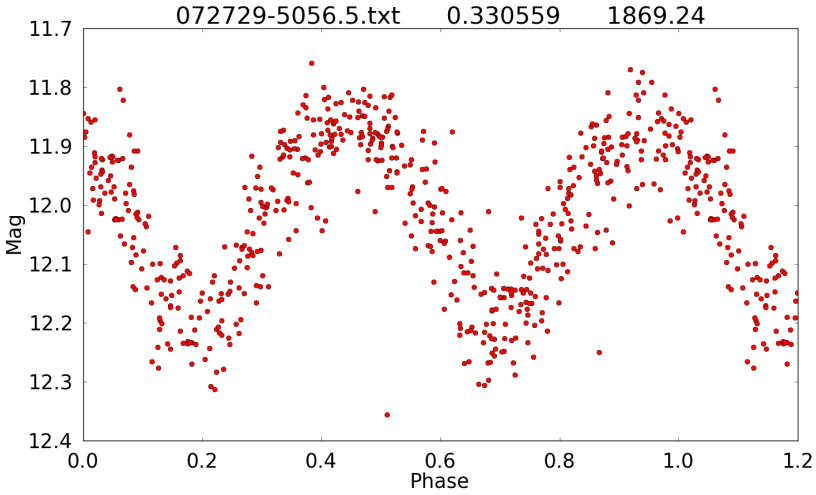

Figure A.56: Light curve of ASAS 072729–5056.5 HPCR star folded on the ME period.

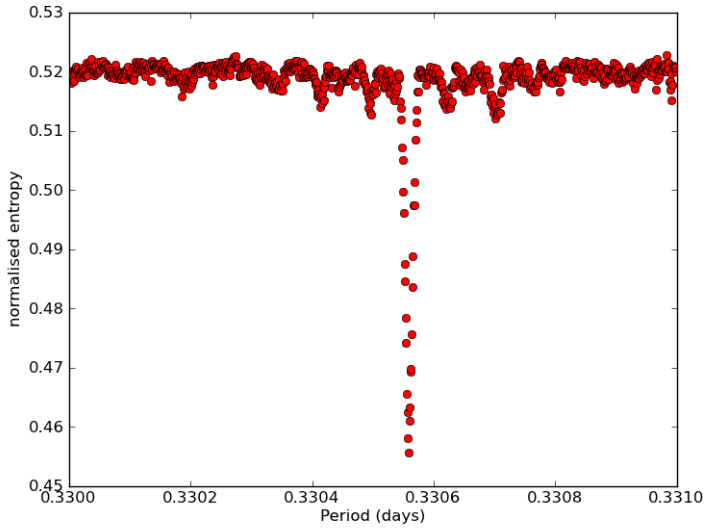

Figure A.57: Period–Entropy curve of ASAS 072729–5056.5 HPCR star.

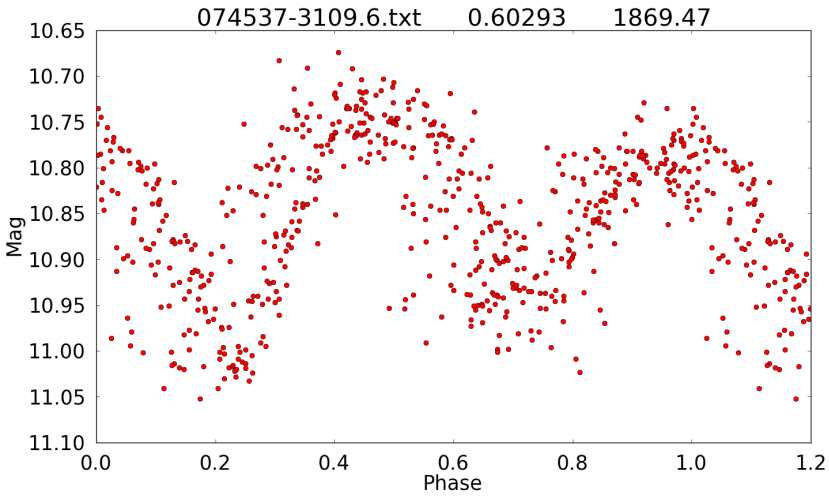

Figure A.58: Light curve of ASAS 074537–3109.6 (GSC 07106–00494) HPCR star folded on the ASAS period.

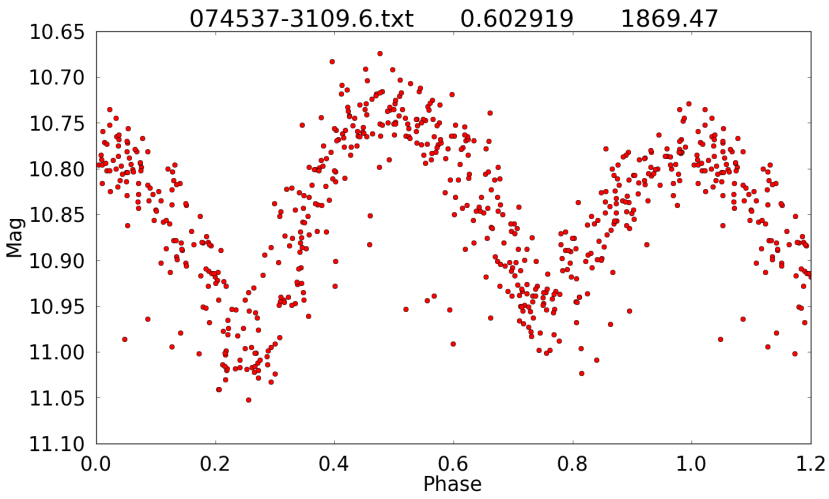

Figure A.59: Light curve of ASAS 074537–3109.6 (GSC 07106–00494) HPCR star folded on the ME period.

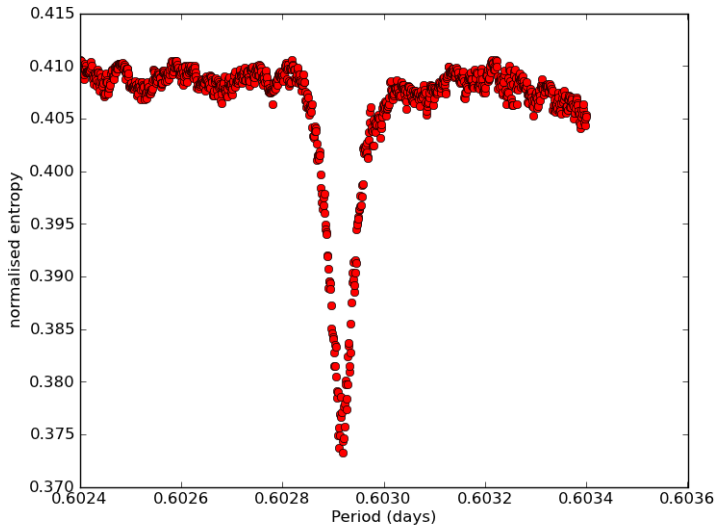

Figure A.60: Period–Entropy curve of ASAS 074537–3109.6 (GSC 07106–00494) HPCR star.

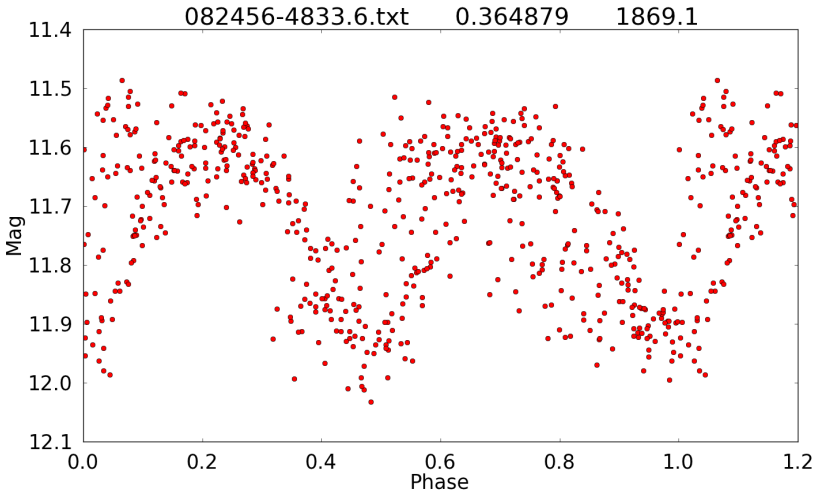

Figure A.61: Light curve of ASAS 082456–4833.6 HPCR star folded on the ASAS period.

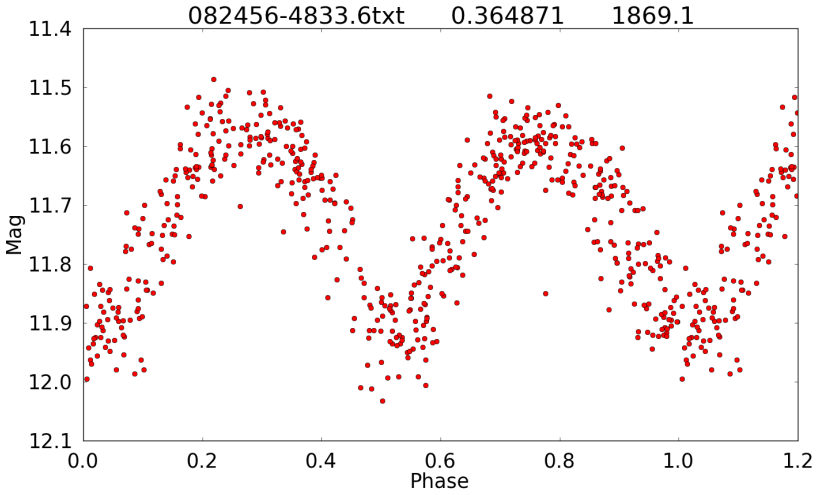

Figure A.62: Light curve of ASAS 082456–4833.6 HPCR star folded on the ME period.

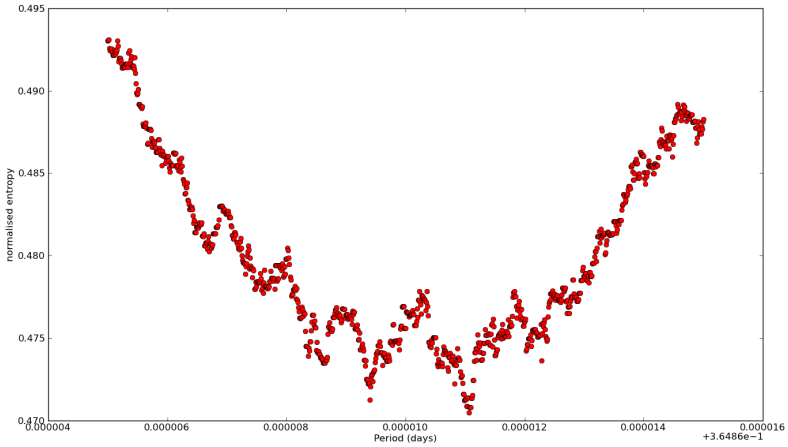

Figure A.63: Period–Entropy curve of ASAS 082456–4833.6 HPCR star.

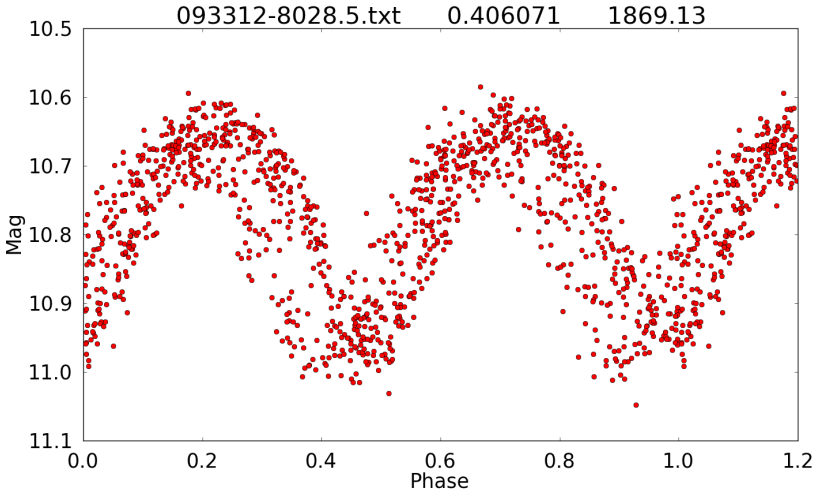

Figure A.64: Light curve of ASAS 093312–8028.5 (GSC 09404–00233) HPCR star folded on the ASAS period.

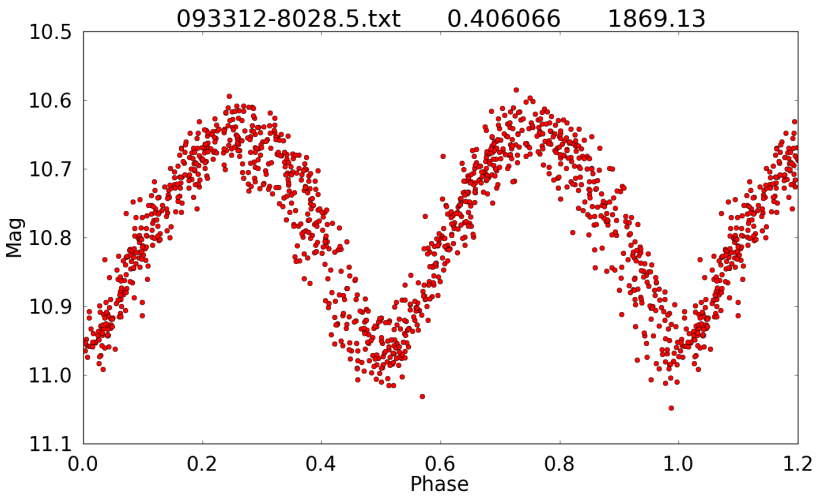

Figure A.65: Light curve of ASAS 093312–8028.5 (GSC 09404–00233) HPCR star folded on the ME period.

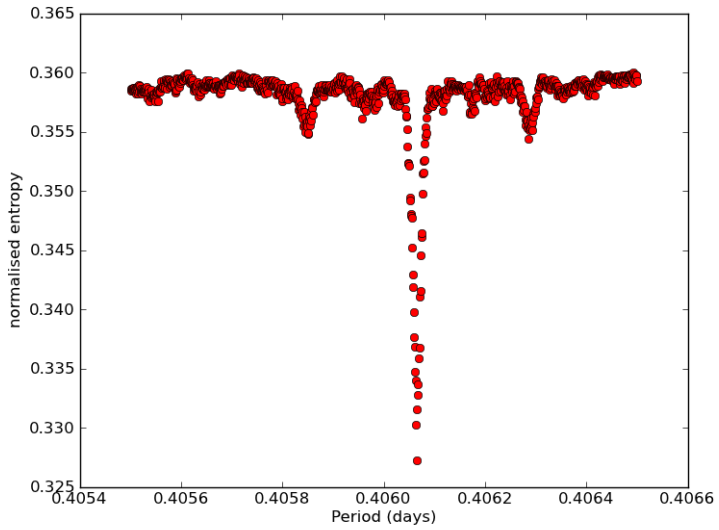

Figure A.66: Period–Entropy curve of ASAS 093312–8028.5 (GSC 09404–00233) HPCR star.

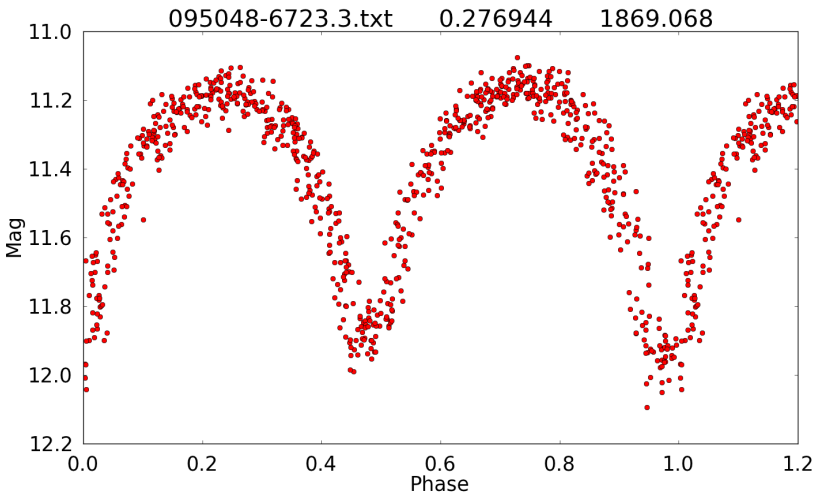

Figure A.67: Light curve of ASAS 095048–6723.3 (New Suspect Variable (NSV) 4657) HPCR star folded on the ASAS period.

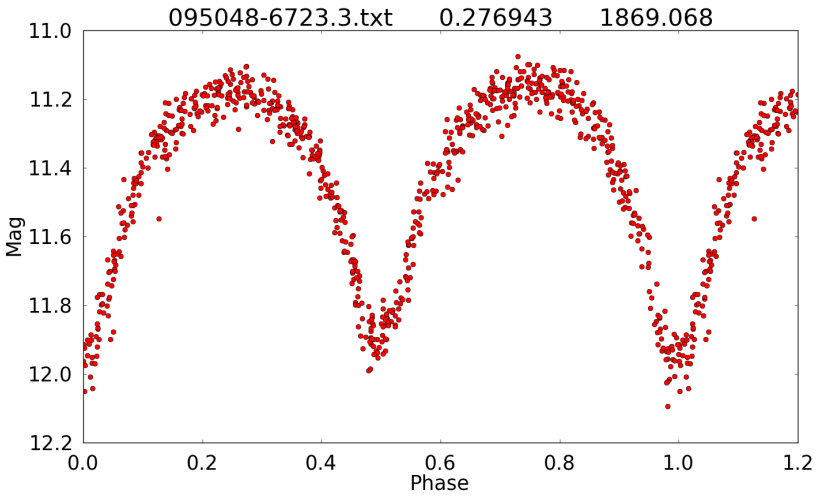

Figure A.68: Light curve of ASAS 095048–6723.3 (New Suspect Variable (NSV) 4657) HPCR star folded on the ME period.

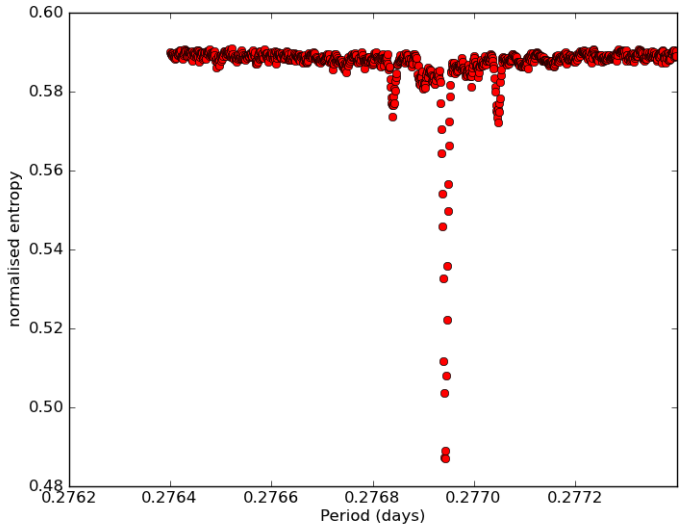

Figure A.69: Period–Entropy curve of ASAS 095048–6723.3 (NSV 4657) HPCR star.

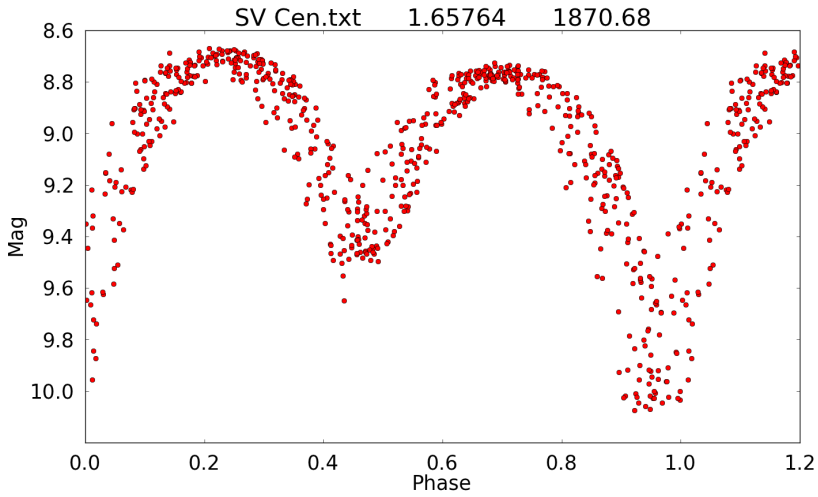

Figure A.70: Light curve of ASAS 114757–6034.0 (SV Cen) HPCR star folded on the ASAS period.

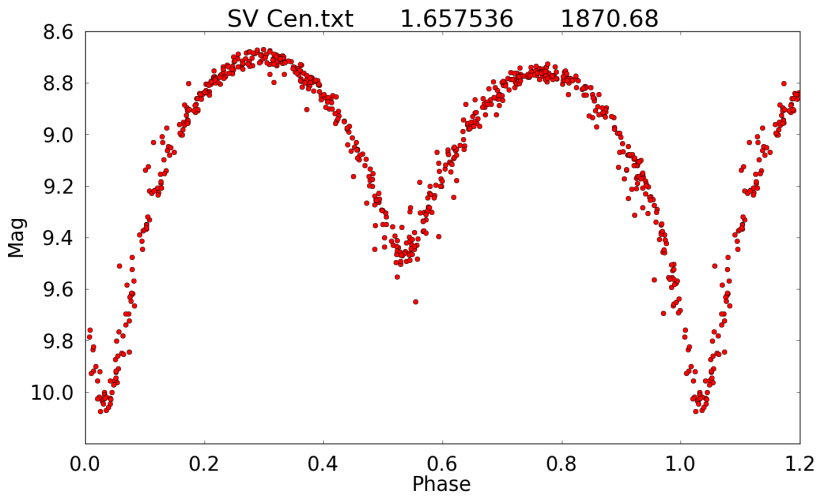

Figure A.71: Light curve of ASAS 114757–6034.0 (SV Cen) HPCR star folded on the ME period.

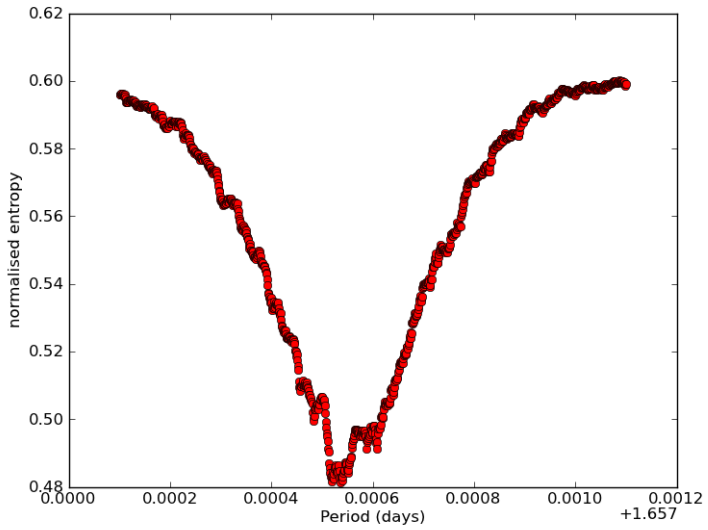

Figure A.72: Period–Entropy curve of ASAS 114757–6034.0 (SV Cen) HPCR star.

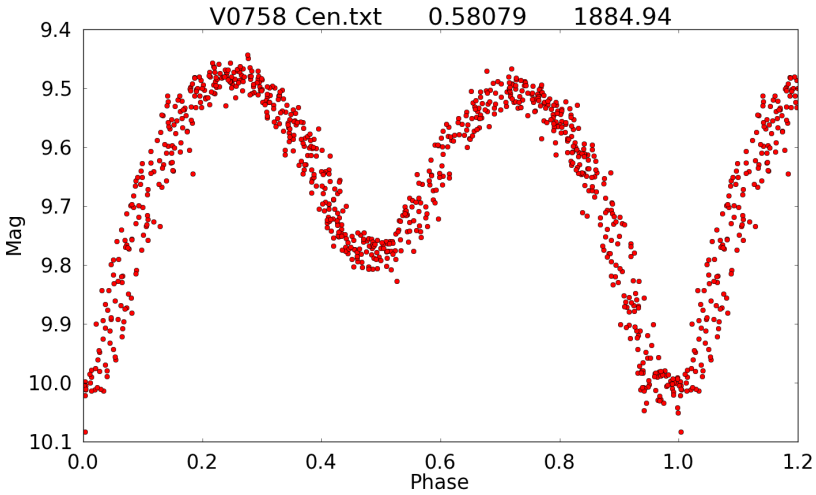

Figure A.73: Light curve of ASAS 135243–5532.5 (V758 Cen) HPCR star folded on the ASAS period.

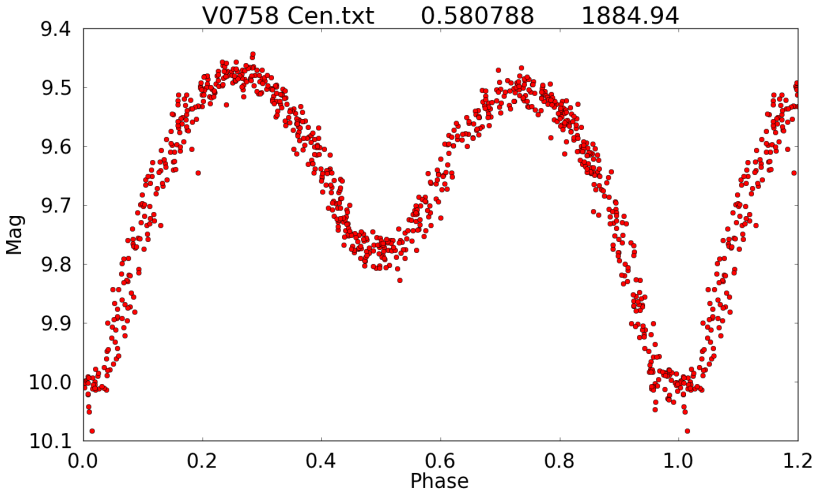

Figure A.74: Light curve of ASAS 135243–5532.5 (V758 Cen) HPCR star folded on the ME period.

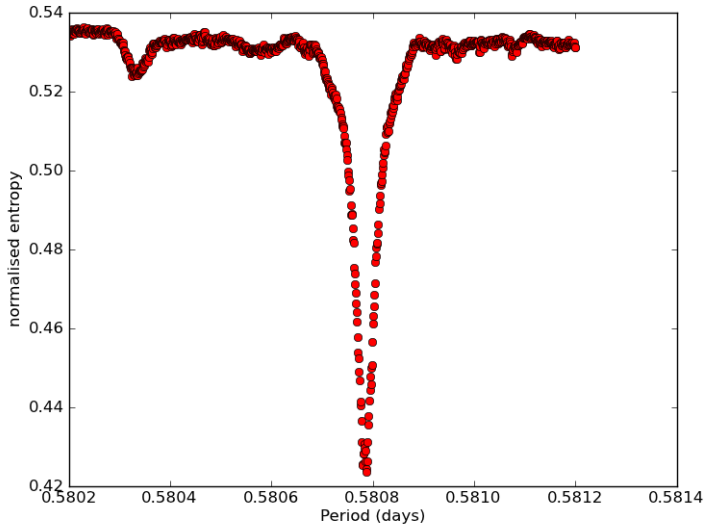

Figure A.75: Period–Entropy curve of ASAS 135243–5532.5 (V758 Cen) HPCR star.

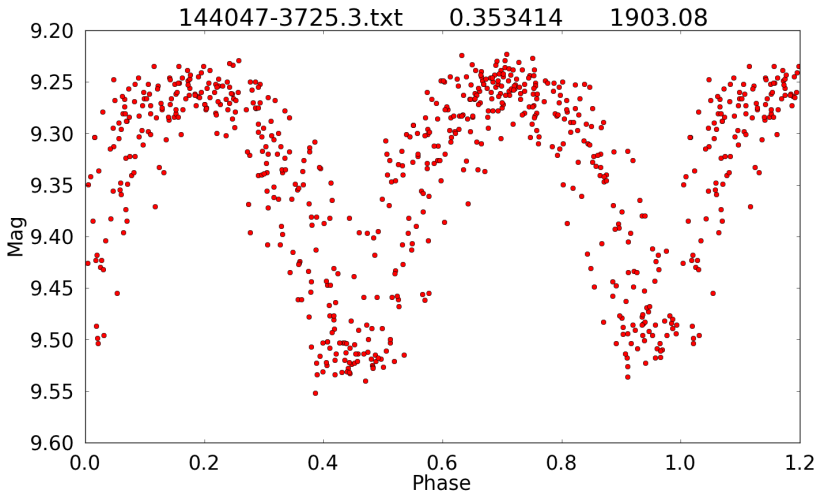

Figure A.76: Light curve of ASAS 144047–3725.3 (HD 128910) HPCR star folded on the ASAS period.

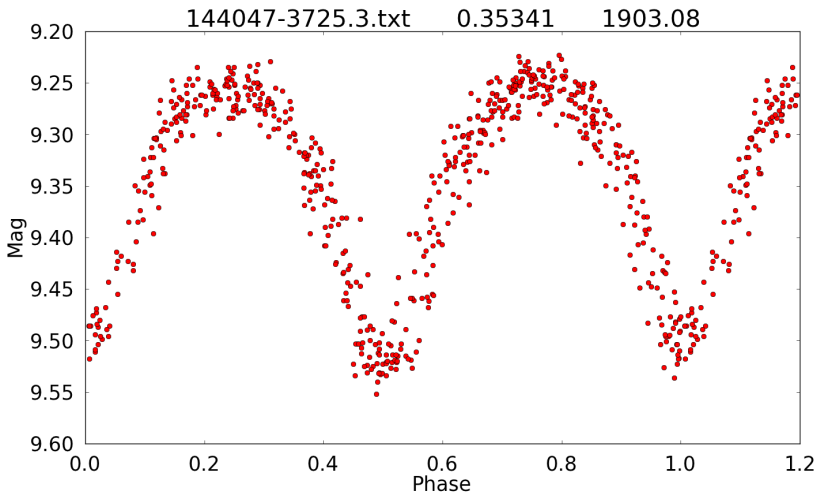

Figure A.77: Light curve of ASAS 144047–3725.3 (HD 128910) HPCR star folded on the ME period.

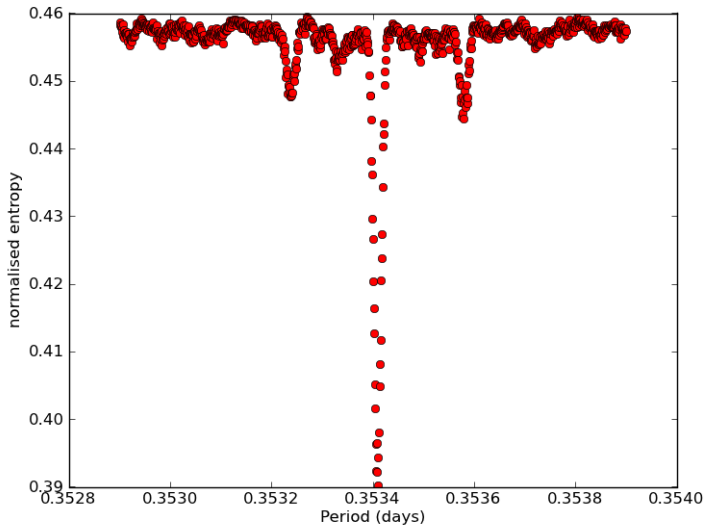

Figure A.78: Period–Entropy curve of ASAS 144047–3725.3 (HD 128910) HPCR star.

A.4 ASAS & ME Periods

Table A.1: This table consolidates data relevent to this study, for stars, where not all the data has been previously given and also for stars which have not been previously mentioned in this dissertation. Nearly all these stars satisfied the ASAS selection criteria described in the section 1.1 introduction. ASAS 004430–3606.5 was initially believed to an EC variable but is actually classified as a semi-detached binary(ESD). ASAS 001522–3202.7 is classified as Mira type star with a period of 366 days and it took many hours for the ME programme to determine its period. These stars were all used in assessing the accuracy of the ME code and the number of divisions into which the phase–magnitude plane of the light curves should be optimally divided. There was no particular reason why the information for some stars was presented and that of other stars in this list were not, however adding the light curves of all the stars to this dissertation would add no further useful information. The column labelled N lists the number of ASAS data points used in the ME programme, from which it can be seens that 300 to 400 data points is the common size of the ASAS data files. Periods were calculated using the ME program and compared with the ASAS periods. Columns labelled ASAS and ME respectively, list in days, the ASAS periods and the ME periods. The last column gives the magnitude range of the original ASAS data.

ASAS ID	N	ASAS	ME	Magnitude range
003628+2132.3	204	0.366125	0.366135	10.913 – 11.367
011638–3942.5	488	0.379920	0.379917	10.197 – 10.868
012104+0736.3	312	0.475611	0.475610	8.478 – 8.889
014656–0945.1	454	0.485960	0.485952	10.769 – 11.636
014854–2053.6	747	0.316849	0.316851	10.247 – 11.136
023833–1417.9	470	0.440790	0.440789	9.368 – 10.027
024952+0856.3	302	0.379920	0.379925	8.688 – 8.947
030701–5608.1	606	0.625110	0.625105	10.9 – 11.823
030953–0653.6	479	0.445280	0.445289	10.392 – 11.018
033459+1742.6	352	0.399946	0.399951	9.559 – 10.046
034814+2218.9	286	0.341347	0.341350	11.004 – 11.832
034928+1254.7	318	0.305372	0.305372	9.114 – 9.707
035153–1031.8	486	0.507654	0.507652	8.1 – 8.664
041209–1028.2	508	0.321499	0.321499	8.15 – 8.985
042925–3334.6	968	0.634190	0.634206	9.895 – 10.443
051114–0833.4	577	0.423400	0.423408	9.187 – 9.959
051832–6813.6	923	0.285461	0.285462	10.827 – 11.636
062605+2759.9	90	0.247053	0.494131	10.067 – 10.541
064558–0017.5	430	0.568030	0.568020	10.5 – 11.37
071058–0352.8	629	0.677050	0.677046	8.181 – 8.769
073246–2047.5	743	0.819250	0.819249	8.377 – 8.895
073338–5007.4	593	0.432618	0.432621	10.305 – 10.931
073905–0239.1	502	0.637704	0.637705	8.847 – 9.516
084002+1900.0	489	0.382882	0.382885	9.831 – 10.318

Table 6.1 cont.

ASAS ID	N	ASAS	ME	Magnitude range
084108–3212.1	947	2.318500	2.318547	10.591 – 11.617
100141+1724.5	348	0.284098	0.284101	9.454 – 10.207
100234+1702.8	347	0.487736	0.487734	10.139 – 10.767
100248+0105.7	370	0.419820	0.419821	9.768 – 10.224
101602–0618.5	494	0.540111	0.540113	9.267 – 9.546
104033+1334.0	297	0.618060	0.618056	9.491 – 10.112
105030–0241.7	737	0.443432	0.443432	8.842 – 9.256
110211+0953.7	330	0.365798	0.365801	8.855 – 9.399
110505+0509.1	336	0.430356	0.430360	9.247 – 9.901
120103+1300.5	416	0.642650	0.642647	8.28 – 8.916
121206+2232.0	234	0.220686	0.220685	11.183 – 12.174
123300+2642.9	345	0.237348	0.237347	10.992 – 11.794
131032–0409.5	393	0.311251	0.311248	9.588 – 10.135
134607+0506.9	334	0.407672	0.407674	7.020 – 7.532
141726+1234.1	398	0.342315	0.342316	10.373 – 11.144
141937+0553.8	336	0.480687	0.480690	7.407 – 7.916
143504+0906.8	345	0.355154	0.355150	8.87 – 9.18
144803+1356.7	297	0.413767	0.413759	9.2 – 9.441
152243+1615.7	318	0.148382	0.296771	8.09 – 8.41
153152–1541.1	496	0.358259	0.358254	10.062 – 10.626
155649+2216.0	240	0.386498	0.386496	10.764 – 11.768
164121+0030.4	374	0.453390	0.453390	8.37 – 8.897
165717+1059.8	422	0.207783	0.415566	10.41 – 10.672
171358+1621.0	302	0.421522	0.421525	8.308 – 8.815
173356+0810.0	349	0.425403	0.425422	8.469 – 8.651
175332–0354.9	550	0.426520	0.426516	9.165 – 9.413
180921+0909.1	368	0.409000	0.409005	8.79 – 9.427
182913+0647.3	350	0.375300	0.375305	9.261 – 9.723
185318+2113.5	332	21.84685	0.493326	9.698 – 9.884
193524+0550.3	334	0.370306	0.370313	10.45 – 11.131
194813+0918.5	347	0.506786	0.506797	9.251 – 10.264
203113+0513.2	393	0.521690	0.521684	8.673 – 9.059
204628–7157.0	1034	0.795000	0.794990	8.564 – 9.074
205710+1939.0	247	0.363840	0.363844	8.591 – 8.811

Table 6.1 cont.

ASAS ID	N	ASAS	ME	Magnitude range
222257+1619.4	300	0.361487	0.361503	10.787 – 11.601
233655+1548.1	232	0.636880	0.636886	9.238 – 9.715
234535+2528.3	271	0.578450	0.578461	8.862 – 9.797
234718–0805.2	321	0.481410	0.481411	10.353 – 10.768
002449–2744.3	515	0.313670	0.313661	12.208 – 13.259
002821–2904.1	526	0.269896	0.269892	11.883 – 12.715
004717–1941.6	751	0.488810	0.488810	11.11 – 11.65
014933–1937.6	708	0.340812	0.340812	10.938 – 11.722
052851–3010.2	589	0.302101	0.302097	11.192 – 11.724
060557–5342.9	731	0.463630	0.463639	10.76 – 11.21
062254–7502.0	1015	0.257704	0.257706	11.263 – 11.892
062426–2044.9	738	0.384698	0.384692	10.45 – 11.027
065232–2533.5	589	0.418634	0.418637	8.588 – 9.107
070959–3639.5	772	0.371832	0.371832	9.619 – 9.882
071727–4007.7	619	0.320267	0.320264	11.059 – 11.894
072729–5056.5	594	0.330552	0.330559	11.759 – 12.356
074537–3109.6	582	0.602930	0.602919	10.674 – 11.052
082456–4833.6	587	0.364879	0.364873	11.487 – 12.033
093312–8028.5	1172	0.406071	0.406065	10.585 – 11.048
095048–6723.3	818	0.276944	0.276943	11.076 – 12.094
114757–6034.0	685	1.657640	1.657536	8.669 – 10.076
135243–5532.5	866	0.580790	0.580788	9.443 - 10.084
144047–3725.3	632	0.353414	0.353410	9.223 – 9.552
000425–5346.4	219	0.288260	0.288262	13.297 – 14.436
000410–4108.2	156	0.525510	0.525495	13.215 – 14.991
001522–3202.7	597	425.0000	732.0000	6.121 – 13.01
001646+1014.7	311	20.65571	0.997270	6.389 – 7.428
013149+1537.5	239	0.329240	0.332730	7.394 – 7.633
035324–2902.4	469	0.339330	0.339331	13.361 – 14.387
044017–2410.7	343	0.416320	0.416050	13.551 – 14.696
044853–0911.9	339	0.489630	0.489632	13.448 – 14.719
053420–2606.6	358	0.298081	0.298099	13.676 – 15.043
054911–1902.6	434	0.314238	0.314239	13.409 – 14.658
212125–0309.6	320	0.374460	0.374456	9.71 – 10.192
004430–3606.5	502	0.246539	0.246535	9.522 – 9.732

A.5 Randomly Selected Stars

Some light curves are presented in this section, which were randomly selected, although one factor which played a part in their selection was that their light curves are not sharp when plotted with either the ASAS or ME period. Fig. A.82 shows the light curve for 001522–3202.7 which according to ASAS has a period of 425 days while the minimum entropy program determines that the period is 366 days. Clearly this is not an EW variable star. The curve folded on the ME period produces a much sharper light curve than the ASAS period of 001522–3202.7. ASAS 013149+1537.5 when folded on the ME period produced a result which was not recognisable as a variable star. However, this star is very bright (7.6 mag) and probably results in some saturation of the CCD.

The characteristics of 6 light curves with brightness on the lower limit of the ASAS telescopes appear below. System and atmospheric noise therefore will have a big impact on the quality of these data points. In addition, these data files also have numbers of data points which correspond to the typical low values of the ASAS data files. For this reason the lack of clear sharp light curves is expected.

ASAS 000425-5346.4 has 219 data points and has a brightness of 13.82 Mag. (Fig. A.80
ASAS 035324-2902.4 has 469 data points and has a brightness of 13.74 Mag. (Fig. A.88)
ASAS 044017-2410.7 has 343 data points and has a brightness of 13.75 Mag. (Fig. A.90)
ASAS 044853-0911.9 has 339 data points and has a brightness of 13.71 Mag. (Fig. A.92)
ASAS 053420-2606.6 has 358 data points and has a brightness of 14.24 Mag. (Fig. A.94)
ASAS 054911-1902.6 has 434 data points and has a brightness of 13.74 Mag. (Fig. A.96)

ASAS 212125-0309.6 (HV Aqr) has 320 data points and has a brightness of 9.85 Mag. (Fig. A.98). This light curve is the sharpest of the light curves is this section. This is because the stars brightness is well inside the specifications of the ASAS telescopes. The curve would however be better if the data file had more points.

ASAS 004430-3606.5 (CR Scl) has 502 data points and a brightness of 9.62 Mag. (Fig. A.86). In this case the ME period is not as good as the ASAS period. This is surprising due to the fairly large number of data points. This leads to the expectation that this star may be an HPCR star and in fact the American Association of Variable

Star Observers (AAVSO - http://www.aavso.org/) has published a period change rate of 0.26×10^{-5} d yr^{-1} which is typical of the period change rates for the 31 HPCR stars of Pilecki *et al.* (2007). Note that AAVSO identifies this star as ASAS J004430-3606.5

Note that the ME programme requires an initial estimate of the period and if this initial estimate is too far off the true period, the ME programme will not find the true period in a reasonably short time.

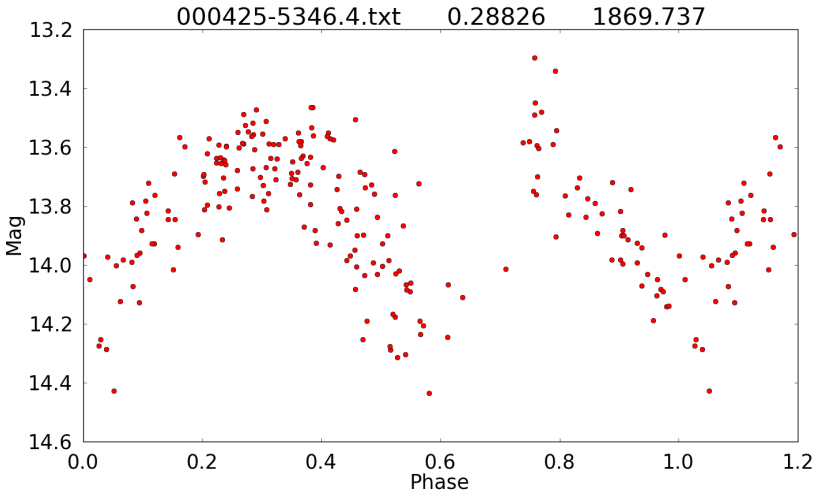

Figure A.79: Light curve of ASAS 000425–5346.4 folded on the ASAS period.

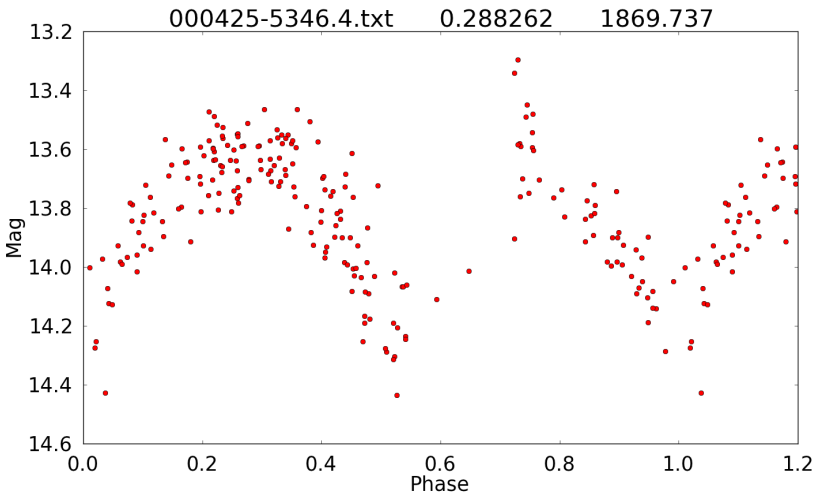

Figure A.80: Light curve of ASAS 000425–5346.4 folded on the ME period.

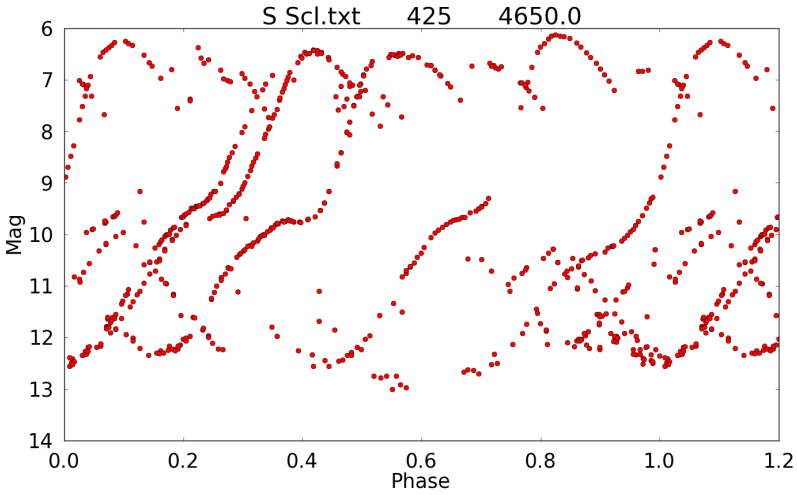

Figure A.81: Light curve of ASAS 001522–3202.7 folded on the ASAS period.

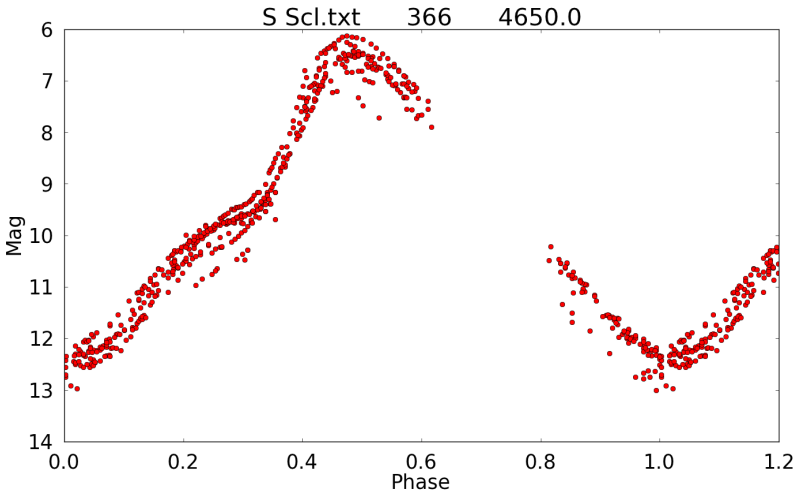

Figure A.82: Light curve of ASAS 001522–3202.7 folded on the ME period.

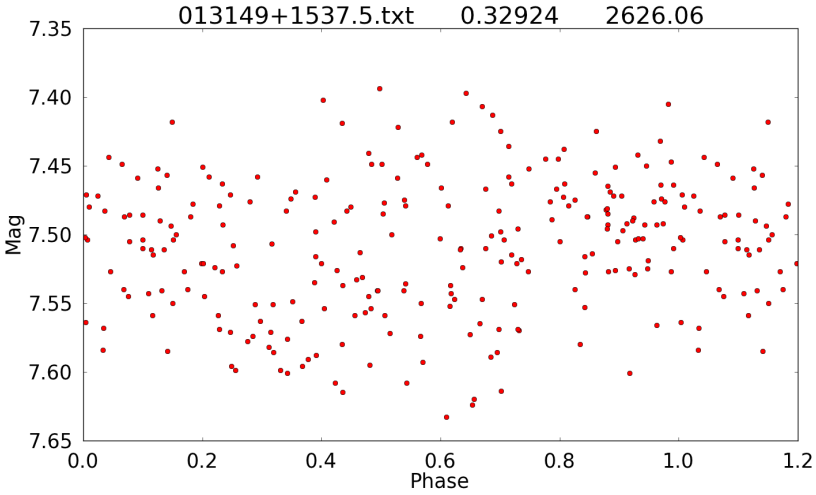

Figure A.83: Light curve of ASAS 013149+1537.5 folded on the ASAS period.

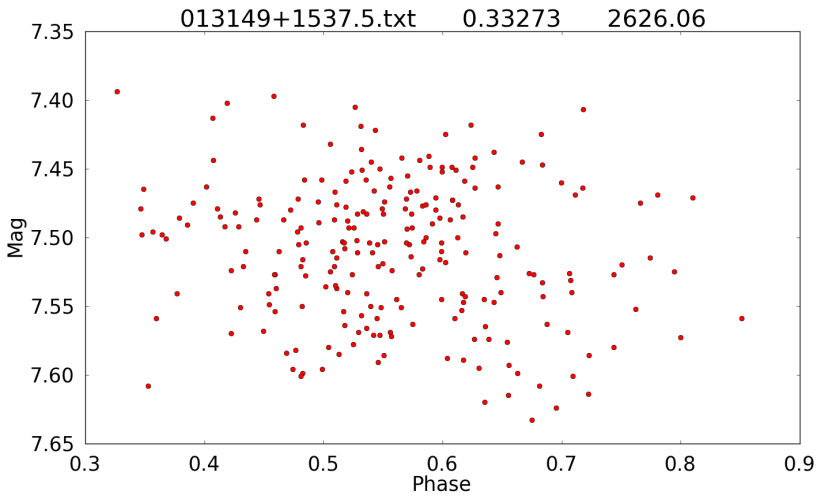

Figure A.84: Light curve of ASAS 013149+1537.5 folded on the ME period.

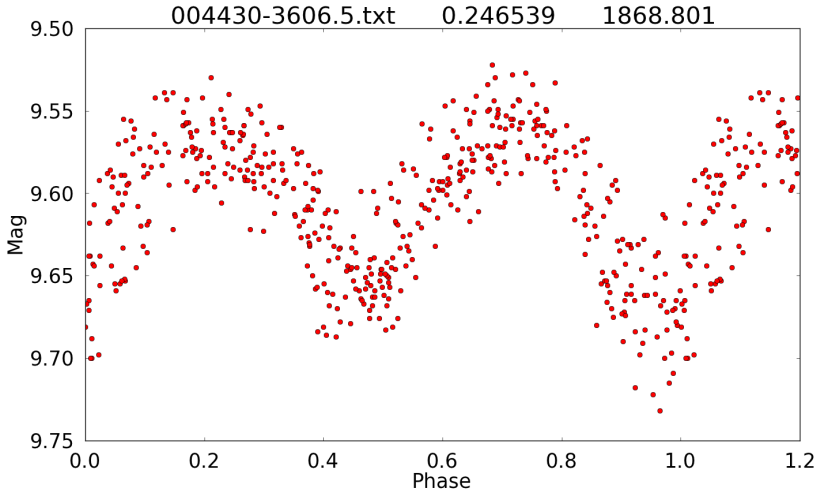

Figure A.85: Light curve of ASAS 004430–3606.5 folded on the ASAS period.

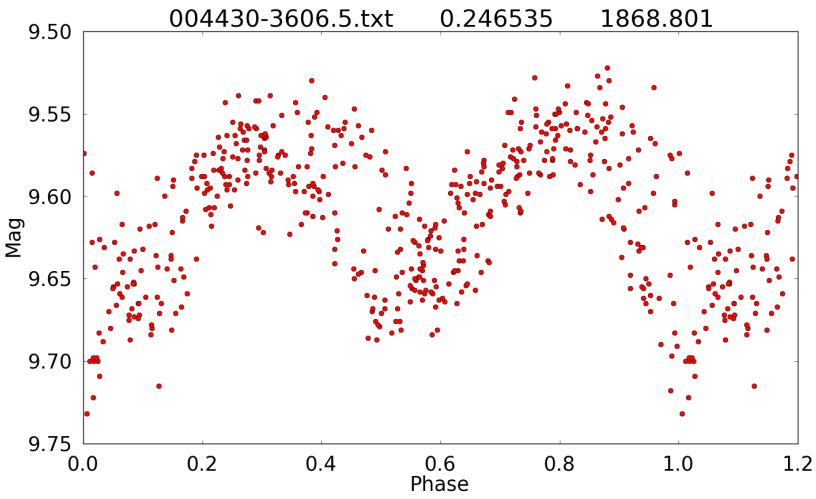

Figure A.86: Light curve of ASAS 004430–3606.5 folded on the ME period.

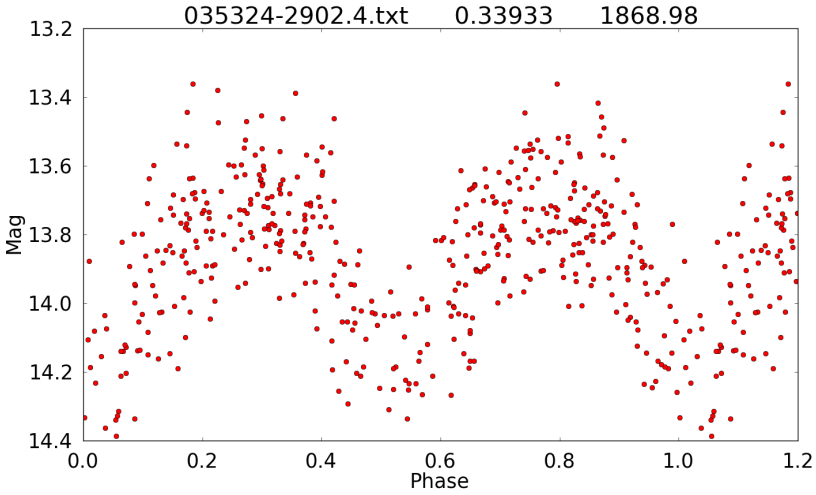

Figure A.87: Light curve of ASAS 035324–2902.4 folded on the ASAS period.

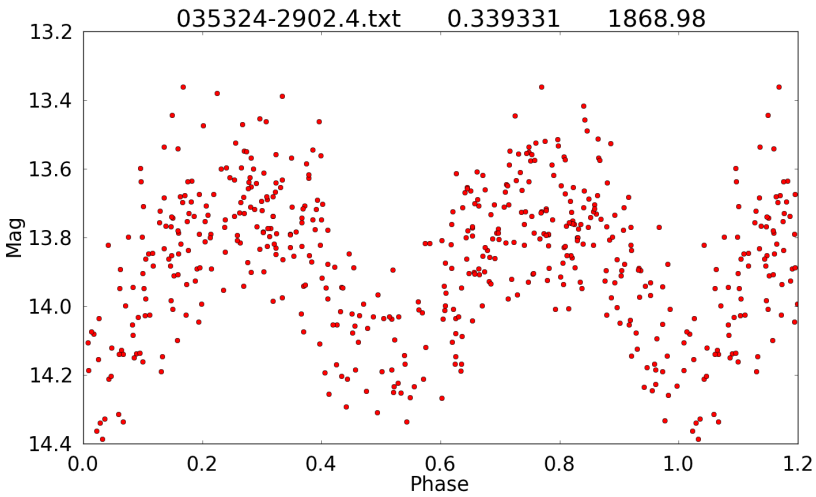

Figure A.88: Light curve of ASAS 035324–2902.4 folded on the ME period.

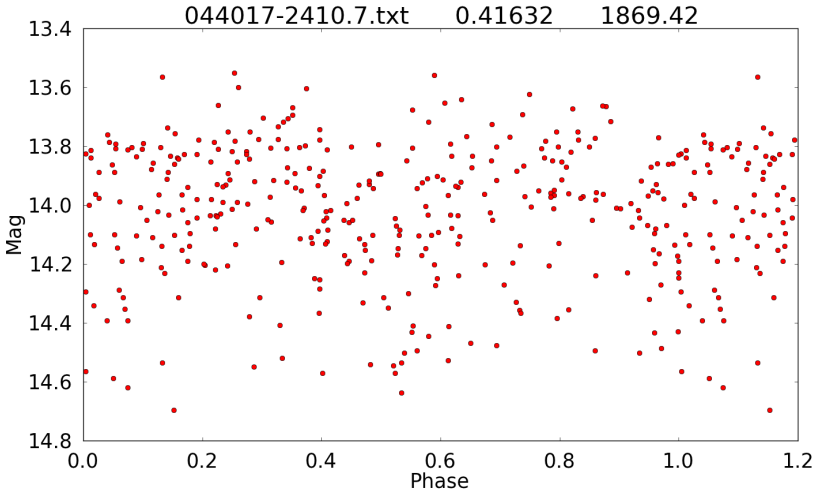

Figure A.89: Light curve of ASAS 044017–2410.7 folded on the ASAS period.

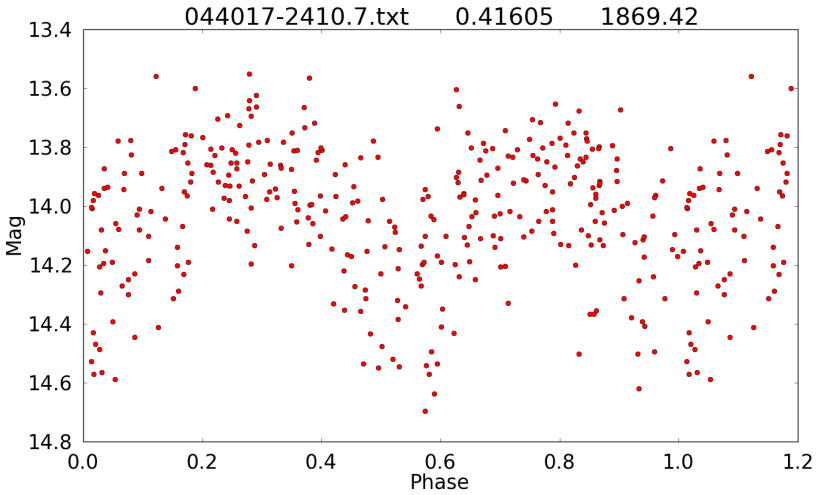

Figure A.90: Light curve of ASAS 044017–2410.7 folded on the ME period.

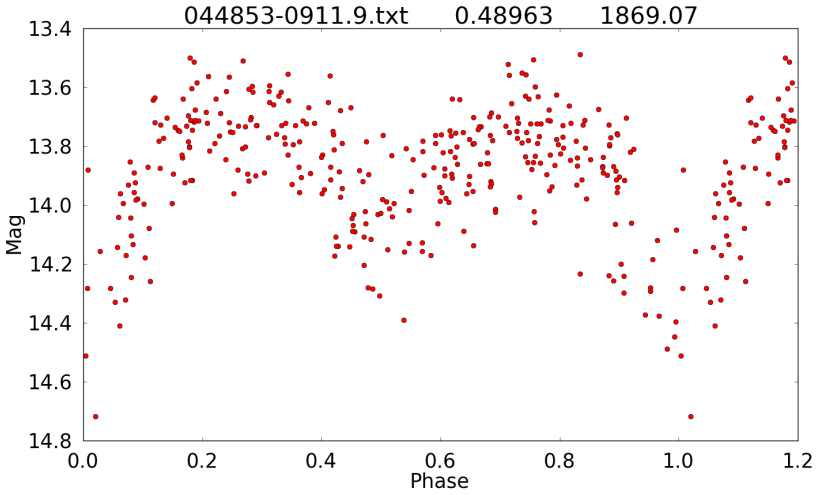

Figure A.91: Light curve of ASAS 044853–0911.9 folded on the ASAS period.

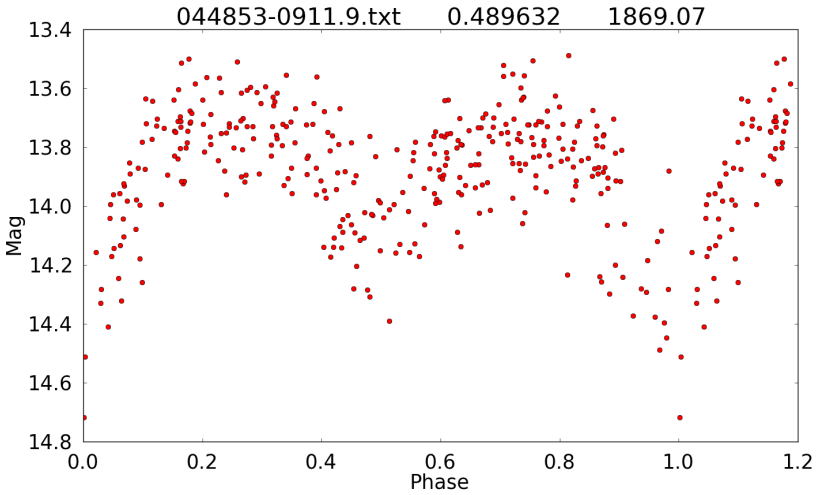

Figure A.92: Light curve of ASAS 044853–0911.9 folded on the ME period.

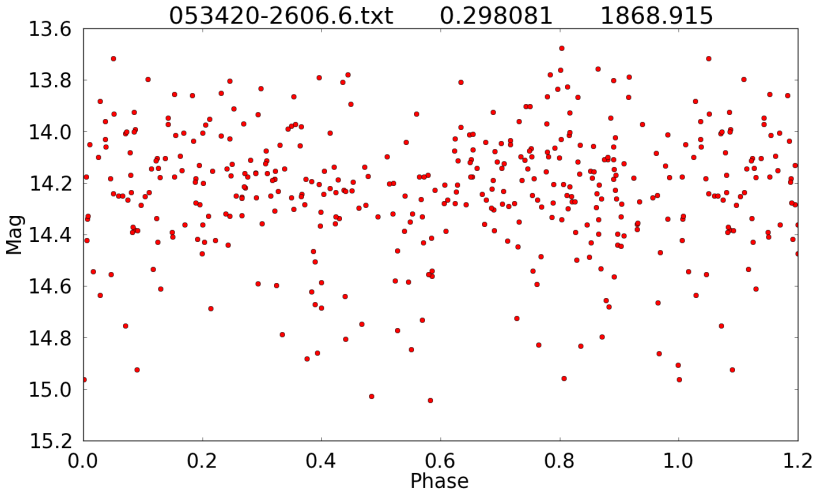

Figure A.93: Light curve of ASAS 053420–2606.6 folded on the ASAS period.

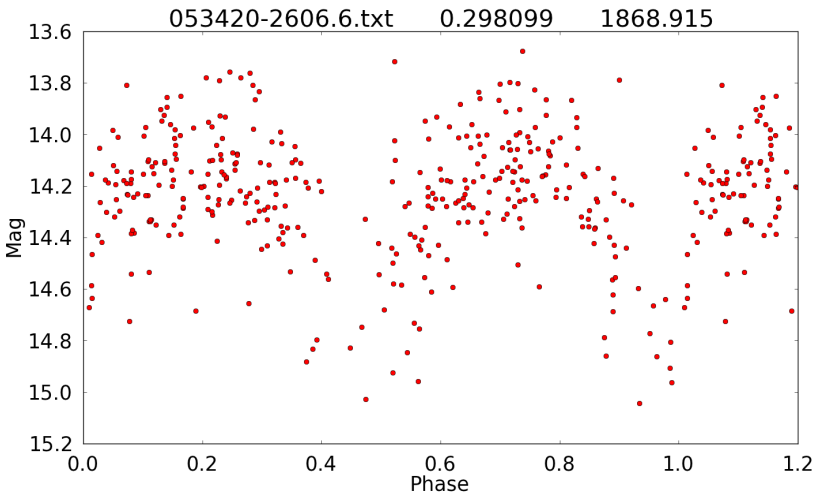

Figure A.94: Light curve of ASAS 053420–2606.6 folded on the ME period.

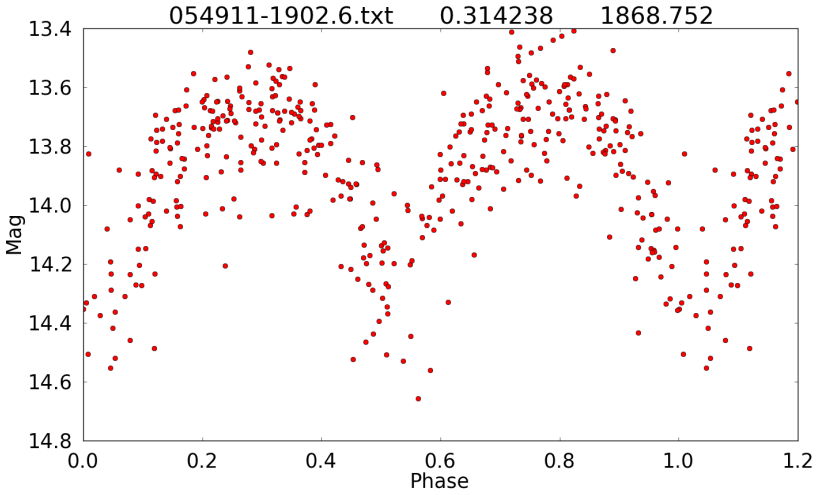

Figure A.95: Light curve of ASAS 054911–1902.6 folded on the ASAS period.

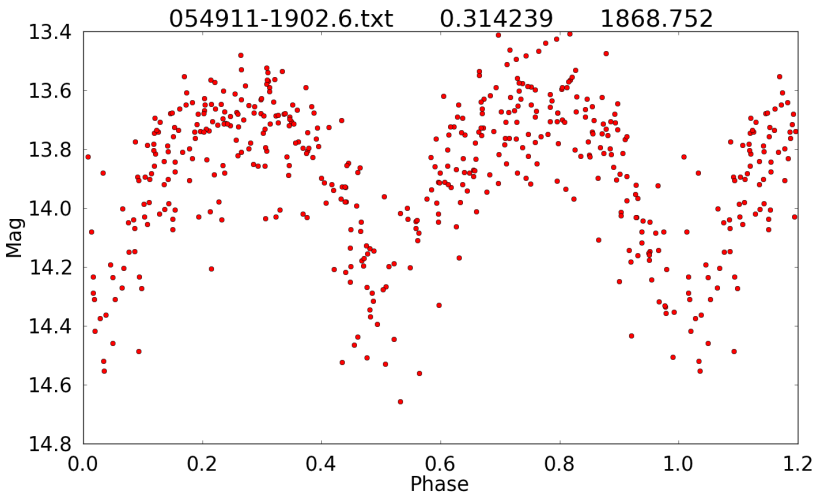

Figure A.96: Light curve of ASAS 054911–1902.6 folded on the ME period.

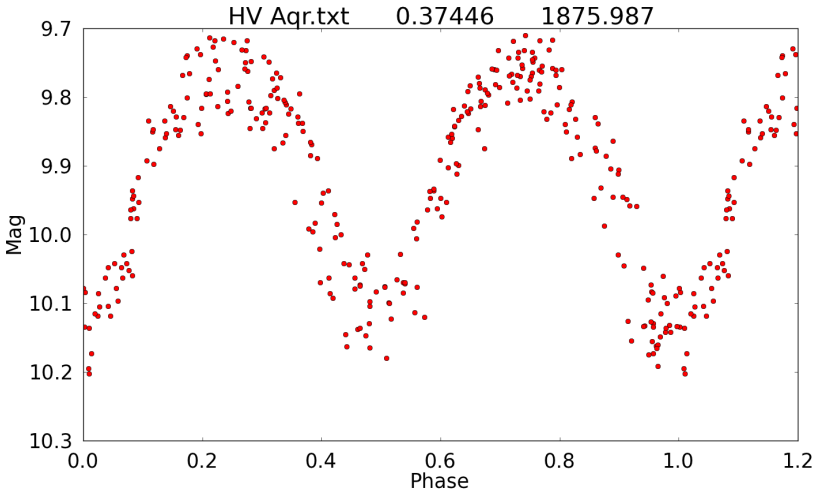

Figure A.97: Light curve of ASAS 212125–0309.6 (HV Aqr) folded on the ASAS period.

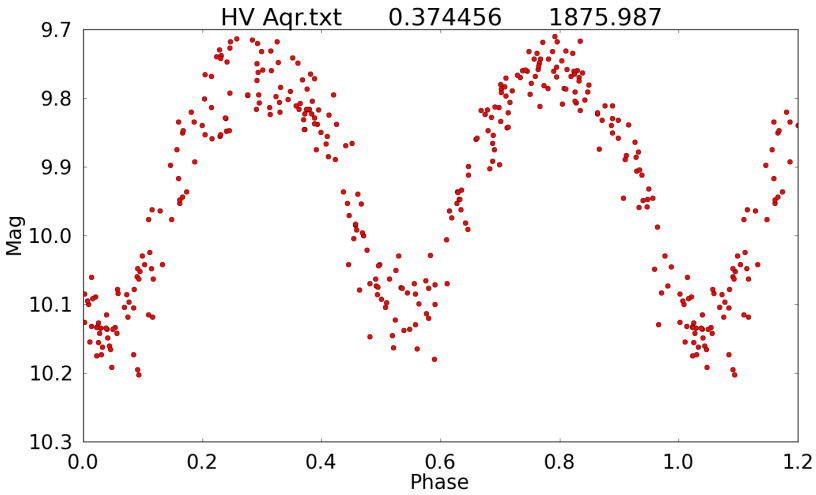

Figure A.98: Light curve of ASAS 212125–0309.6 (HV Aqr) folded on the ME period.

References

Adams, W. S. and Joy, A. H. (1919). *ApJ*, **49**, 186.

Baldwin, J. M. (1908). *MNRAS*, **69**, 78.

Biermann, P. and Thomas, H.-C. (1972). *A&A*, **16**, 60.

Binnendijk, L. (1957). *JRASC*, **51**, 83.

Binnendijk, L. (1961). *AJ*, **66**, 27.

Binnendijk, L. (1970). *VA*, **12**, 217.

Bodenheimer, P., Ruzmajkina, T., and Mathieu, R. D. (1993). In E. H. Levy and J. I. Lunine, editors, *Protostars and Planets III*, page 367.

Bonnell, I. A. (2001). The formation of binary stars. *IAUS*, **200**, 23.

Boss, A. P. (1988). *ComAp*, **12**, 169.

Bradstreet, D. H. and Guinan, E. F. (1988). *ESA Special Publication*, **281**, 303.

Carter, T. (2011). Lecture Notes. California State University, Stanislaus. Also available as `http://csustan.csustan.edu/~tom/Lecture-Notes/Information-Theory/info-lec.pdf`.

Chaisson, E. and McMillan, S. (2005). *Astronomy Today*. 5th Edition, Prentice Hall. ISBN 0-13-144596-0.

Chandler, S. C. (1892). *AJ*, **11**, 113.

Cincotta, P. M., Mendez, M., and Nunez, J. A. (1995). *ApJ*, **449**, 231.

Cincotta, P. M., Helmi, A., Mendez, M., Nunez, J. A., and Vucetich, H. (1999). *MNRAS*, **302**, 582.

Deb, S. and Singh, H. P. (2011). *MNRAS*, **412**, 1787.

Dryomova, G. N. and Svechnikov, M. A. (2006). *Ap*, **49**, 358.

Eggen, O. J. (1967). *MmRAS*, **70**, 111.

Flannery, B. P. (1976). *ApJ*, **205**, 217.

Gazeas, K. D. and Niarchos, P. G. (2006). *MNRAS*, **370**, L29.

Haffner, H. (1937). *ZA*, **14**, 285.

Hartley, R. V. L. (1928). *The Bell System Technical Journal*, page 535.

Hazlehurst, J. (1974). *A&A*, **36**, 49.

Hazlehurst, J. and Refsdal, S. (1980). *A&A*, **84**, 200.

Hilditch, R. W. (2001). *An Introduction to Close Binary Stars*. Cambridge University Press, Cambridge, UK. ISBN 0521241065.

Hilditch, R. W., King, D. J., and McFarlane, T. M. (1988). *MNRAS*, **231**, 341.

Huffer, C. M. (1934). *ApJ*, **79**, 369.

Kolb, J., Downing, M., and Clare, R. M. (2010). In *Adaptive Optics for Extremely Large Telescopes, 05014*.

Kopal, Z. (1955). *Annales d'Astrophysique*, **18**, 379.

Kopal, Z. (1959). The International Astrophysics Series, London: Chapman and Hall.

Kroupa, P., Tout, C. A., and Gilmore, G. (1993). *MNRAS*, **262**, 545.

Kubiak, M., Udalski, A., and Szymanski, M. K. (2006). *AcA*, **56**, 253.

Kuiper, G. P. (1948). *ApJ*, **108**, 541.

Lada, C. J. (2006). *ApJ*, **640**, L63.

Lohr, M. E., Norton, A. J., Kolb, U. C., Anderson, D. R., Faedi, F., and West, R. G. (2012). *A&A*, **542**, A124.

Lucy, L. B. (1968a). *ApJ*, **151**, 1123.

Lucy, L. B. (1968b). *ApJ*, **153**, 877.

Lucy, L. B. (1968c). *Highlights of Astronomy*, **1**, 452.

Lucy, L. B. (1973). *Ap&SS*, **22**, 381.

Lucy, L. B. (1976). *ApJ*, **205**, 208.

Lucy, L. B. (1977). *AJ*, **82**, 1013.

Lucy, L. B. and Wilson, R. E. (1979). *ApJ*, **231**, 502.

Mauder, H. (1972). *A&A*, **17**, 1.

Mullan, D. J. (1975). *ApJ*, **198**, 563.

Muller, G. and Kempf, P. (1903). *ApJ*, **17**, 201.

Niarchos, P. (1977). *Ap&SS*, **47**, 79.

Paczyński, B., Szczygieł, D. M., Pilecki, B., and Pojmański, G. (2006). *MNRAS*, **368**, 1311.

Paschke, A. and Brat, L. (2006). *Open European Journal on Variable Stars*, **23**, 13.

Pilecki, B., Fabrycky, D., and Poleski, R. (2007). *MNRAS*, **378**, 757.

Pojmanski, G. (2000). *AcA*, **50**, 177.

Prasad, V., Pandey, J. C., Patel, M. K., and Srivastava, D. C. (2013). *NA*, **20**, 52–61.

Pribulla, T. and Rucinski, S. M. (2006). *AJ*, **131**, 2986.

Prša, A. and Zwitter, T. (2005). *ApJ*, **628**, 426.

Rahunen, T. (1981). *A&A*, **102**, 81.

Rahunen, T. and Vilhu, Q. (1977). *A&A*, **56**, 99.

Reif, F. (1965). *Fundamentals of Statistical and Thermal Physics*. Waveland Press, Inc., Nong Grove, IL USA. ISBN 978-1-57766-612-7.

Robertson, J. A. and Eggleton, P. P. (1977). *MNRAS*, **179**, 359.

Roxburgh, I. W. (1966). *ApJ*, **143**, 111.

Rucinski, S. (1973). *Postepy Astronomii Krakow*, **21**, 189.

Rucinski, S. M. (1993a). *PASP*, **105**, 1433.

Rucinski, S. M. (1993b). In J. Sahade, G. E. McCluskey, Jr., and Y. Kondo, editors, *Astrophysics and Space Science Library*, volume 177 of *Astrophysics and Space Science Library*, page 111.

Rucinski, S. M. and Lu, W. X. (1999). *AJ*, **118**, 515.

Rucinski, S. M. and Lu, W. X. (2000). *MNRAS*, **315**, 587.

Russell, H. N. (1912). *ApJ*, **36**, 133.

Samus, N. N. and Durlevich, O. V. (2009). *VizieR Online Data Catalog*, **1**, 2025.

Shannon, C. E. (1948). *The Bell systems Technical Journal*, **27**, 379.

Shapley, H. (1948). *Harvard Observatory Monographs*, **7**, 249.

Shapley, H. and van der Bilt, J. (1917). *ApJ*, **46**, 281–290.

Sharma, S. and Johnston, K. V. (2009). *ApJ*, **703**, 1061.

Shu, F. H. (1982). *The Physical Universe*. University Science Books.

Shu, F. H., Lubow, S. H., and Anderson, L. (1976). *ApJ*, **209**, 536.

Skelton, P. L. (2009). *MSc Thesis, University of South Africa*.

Stepien, K. (2006a). *AcA*, **56**, 199.

Stepien, K. (2006b). *AcA*, **56**, 347.

Tohline, J. E. (2002). *ARA&A*, **40**, 349.

van Hamme, W. (1982). *A&A*, **105**, 389.

Vilhu, O. (1981). *Ap&SS*, **78**, 401.

Vilhu, O. (1982). *A&A*, **109**, 17.

Vilhu, O. and Rahunen, T. (1980). Close binary stars: Observations and interpretation. *IAUS*, **88**, 491.

Webbink, R. F. (1975). *BAAS*, **7**, 534.

Whelan, J., Mochnacki, S. W., and Worden, S. P. (1974). *MNRAS*, **168**, 31.

Wilsey, N. J. and Beaky, M. M. (2009). *JAAVSO*, **37**, 210.

Wilson, R. E. (1978). *ApJ*, **224**, 885.

Wilson, R. E. and Devinney, E. J. (1971). *ApJ*, **166**, 605.

Woodward, E. J. (1942a). *Harvard College Observatory Circular*, **446**, 1.

Woodward, E. J. (1942b). *Harvard College Observatory Circular*, **447**, 1.

Woodward, E. J. and Wilson, R. E. (1977). *Ap&SS*, **52**, 387.

Yakut, K. and Eggleton, P. P. (2005). *ApJ*, **629**, 1055.